

University of Alberta

**An Extended Jointly Gaussian Approach
for Iterative Equalization**

by

Marcel Jar e Silva

A thesis submitted to the Faculty of Graduate Studies and Research in
partial fulfillment of the requirements for the degree of

Doctor of Philosophy

in

Communications

Department of Electrical and Computer Engineering

©Marcel Jar e Silva
Fall 2011
Edmonton, Alberta

Permission is hereby granted to the University of Alberta Libraries to reproduce single copies of this thesis and to lend or sell such copies for private, scholarly or scientific research purposes only.

Where the thesis is converted to, or otherwise made available in digital form, the University of Alberta will advise potential users of the thesis of these terms.

The author reserves all other publication and other rights in association with the copyright in the thesis and, except as herein before provided, neither the thesis nor any substantial portion thereof may be printed or otherwise reproduced in any material form whatsoever without the author's prior written permission.

To Stella

Abstract

A novel equalization scheme for signals transmitted over multipath Multiple-Input Multiple-Output (MIMO) channels, well-suited for iterative processing, is proposed in this work. This method, dubbed Extended Jointly Gaussian Approach (extended JGA), provides an interesting trade-off between complexity and performance for equalizers based on the JGA. It works by first performing a marginalization over a set of interfering terms, and then using a jointly Gaussian assumption on the remaining interference. It is shown that, with this extension, performance can be greatly improved for some scenarios at the expense of a manageable increase in computational complexity. In order to reduce the computational burden of the detection process, complexity saving techniques are discussed. For Single-Carrier Frequency-Division Multiple Access (SC-FDMA) schemes, the computational burden of the equalization process can be further reduced by using frequency-domain versions of the classical JGA, or the extended JGA proposed in this work. The potential of the extended method is assessed for non-iterative schemes via analysis of Signal to Interference-plus-Noise Ratios (SINRs) at the output of the equalizer. This figure of merit shows that a significant increase in throughput can be obtained by removing some terms from the interference pool, specially for MIMO channels. For iterative equalization, the convergence behaviour of systems applying equalizers based on both the classical and the extended JGA is analyzed by means of EXIT charts. Simulink models of uplink Long Term Evolution (LTE) communication systems, applying both classical and extended JGA equalizers, are used to produce Monte Carlo simulations. These simulations are used to confirm the performance gains indicated by SINR analysis and EXIT charts for realistic MIMO scenarios.

Contents

| | | |
|----------|-----------------------------------------------------------------|-----------|
| 1 | Introduction | 1 |
| 1.1 | Classical equalization schemes for multipath channels | 2 |
| 1.1.1 | Linear equalizers | 4 |
| 1.1.2 | Decision-feedback equalizers | 5 |
| 1.1.3 | Maximum likelihood sequence estimation | 6 |
| 1.2 | MIMO communications | 11 |
| 1.2.1 | Maximum likelihood detection | 11 |
| 1.2.2 | Linear receivers | 12 |
| 1.2.3 | Decision-feedback receivers | 12 |
| 1.3 | Equalization schemes for multipath MIMO systems | 13 |
| 1.4 | Iterative equalization | 14 |
| 1.5 | Thesis overview | 17 |
| 2 | Channel Model | 18 |
| 2.1 | Multipath SISO channel model | 18 |
| 2.2 | Multipath MIMO channel model | 20 |
| 2.3 | Generating channel coefficients | 22 |
| 2.3.1 | Time delay distribution | 23 |
| 2.3.2 | Fading coefficient distribution | 24 |
| 2.4 | Spatial channel model | 25 |
| 2.4.1 | Correlation between channel parameters | 30 |
| 2.4.2 | Coherence time for the SCM | 31 |
| 2.5 | Baseband discrete-time channel model | 32 |
| 2.6 | Channel normalization | 32 |

CONTENTS

| | | |
|----------|----------------------------------------------------------|-----------|
| 3 | The Jointly Gaussian Approach - JGA | 34 |
| 3.1 | Classical JGA | 34 |
| 3.2 | Extended JGA | 38 |
| 3.2.1 | Choice of the set of interferers to be removed | 40 |
| 3.3 | JGA for multipath MIMO channels | 41 |
| 3.4 | Extended JGA for multipath MIMO channels | 43 |
| 3.5 | Low-complexity implementation methods | 45 |
| 3.5.1 | Sliding window | 45 |
| 3.5.2 | Averaging the <i>a priori</i> information | 46 |
| 3.6 | JGA for SC-FDMA | 47 |
| 3.6.1 | Multipath MIMO scenario | 53 |
| 3.6.2 | Extended JGA for SC-FDMA | 53 |
| 3.7 | Complexity analysis | 54 |
| 4 | SINR and EXIT Analysis | 62 |
| 4.1 | SINR analysis | 62 |
| 4.1.1 | SINR for the JGA | 63 |
| 4.1.2 | SINR for the extended JGA | 68 |
| 4.2 | EXIT charts | 73 |
| 4.2.1 | Extrinsic transfer characteristics | 73 |
| 4.2.2 | Comparing EXIT charts for JGA and extended JGA | 77 |
| 5 | Experimental Results | 80 |
| 5.1 | Uncoded system | 80 |
| 5.2 | Iterative equalization system - SISO scenario | 81 |
| 5.3 | SINR analysis - SISO scenario | 84 |
| 5.4 | SINR analysis - MIMO scenario | 87 |
| 5.5 | EXIT charts - MIMO scenario | 91 |

CONTENTS

| | | |
|----------|------------------------------------------------------------------------|------------|
| 5.6 | Comparing analysis and simulation results for a specific channel . . . | 93 |
| 6 | Conclusions and Future Work | 97 |
| 6.1 | Original contributions | 98 |
| 6.2 | Future work | 99 |
| A | Obtaining Soft-Values from LLRs | 107 |
| A.1 | BPSK constellation | 109 |
| A.2 | QPSK constellation | 110 |
| A.3 | 16 QAM constellation | 111 |
| B | HSDPA Standard | 113 |
| B.1 | HSDPA transmission format | 114 |
| B.2 | HSDPA communication system elements | 116 |
| B.2.1 | Turbo codes | 116 |
| B.2.2 | Rate matching | 118 |
| B.2.3 | Channel interleaver | 119 |
| B.2.4 | Channel modulation | 119 |
| B.2.5 | Walsh spreading | 120 |
| B.2.6 | Hybrid Automatic Repeat-Request (HARQ) | 120 |
| B.2.7 | Rake receiver | 121 |
| C | LTE Standard | 122 |
| C.1 | LTE transmission format | 123 |
| C.2 | SC-FDMA communication system elements | 126 |
| C.2.1 | Cyclic redundancy check | 127 |
| C.2.2 | Turbo code | 128 |
| C.2.3 | Rate matching | 129 |
| C.2.4 | Modulation | 129 |

CONTENTS

| | | |
|-------|----------------------------------------------|-----|
| C.2.5 | Transform precoding | 129 |
| C.2.6 | Resource element mapper | 130 |
| C.2.7 | SC-FDMA baseband signal generation | 130 |
| C.2.8 | Cyclic-prefix attachment | 131 |
| C.2.9 | SC-FDMA signal reception | 131 |

List of Tables

| | | |
|-----|--------------------------------------------------------------------------------------------------------------------------------------------------------------------------------------------------------|----|
| 2.1 | Sub-path angle offsets for AoD and AoA (for macrocells and micro-cells). | 29 |
| 3.1 | Computational complexity analysis for a JGA equalizer (BPSK modulation). | 56 |
| 3.2 | Computational complexity analysis for a JGA equalizer (higher-order modulation). | 56 |
| 3.3 | Computational complexity analysis for an extended JGA equalizer (BPSK modulation with only one symbol removed from the interference pool). | 58 |
| 3.4 | Complexity analysis of an extended JGA equalizer with s symbols removed from $\zeta[k]$ (higher-order modulation). | 58 |
| 3.5 | Complexity analysis of a JGA equalizer for SC-FDMA transmission (BPSK modulation). | 60 |
| 3.6 | Complexity analysis of an extended JGA equalizer for SC-FDMA transmission (higher-order modulation). | 60 |
| 3.7 | Total number of complex multiplications required by different equalization schemes. | 61 |
| 5.1 | Percentage of channels in Figures 5.6, 5.7, and 5.8 resulting in each CQI for suburban macrocells (SUMA), urban macrocells (UMA), and urban microcells (UMI), according to the HSDPA standard. | 86 |
| 5.2 | SNRs that result in a frame error rate of 10% for the turbo code specified by the LTE standard. | 87 |

LIST OF TABLES

| | | |
|-----|----------------------------------------------------------------------------------------------------------------------------------------------------------------------------------------------------------|-----|
| 5.3 | Percentage of channels in Figures 5.6, 5.7, and 5.8 resulting in each CQI for suburban macrocells (SUMA), urban macrocells (UMA) and urban microcells (UMI), according to the LTE standard. | 87 |
| 5.4 | Percentage of channels in Figures 5.9, 5.10, and 5.11 resulting in each CQI for urban macrocells (UMA), suburban macrocells (SUMA), and urban microcells (UMI), according to the HSDPA standard. | 90 |
| 5.5 | Percentage of channels in Figures 5.10, 5.9, and 5.11 resulting in each CQI for urban macrocells (UMA), suburban macrocells (SUMA), and urban microcells (UMI), according to the LTE standard. | 90 |
| 5.6 | Channel Coefficients | 95 |
| B.1 | Packet format for different values of CQI. | 115 |
| C.1 | Transmission Bandwidth configuration for LTE | 123 |
| C.2 | CQI Table. | 126 |

List of Figures

| | | |
|-----|--------------------------------------------------------------------------------------------------------------|----|
| 1.1 | Digital communication system schematics diagram. | 2 |
| 1.2 | Water-filling for frequency selective channels. | 3 |
| 1.3 | Decision Feedback Equalizer. | 5 |
| 1.4 | Iterative equalization system schematics diagram. | 14 |
| 2.1 | Multipath propagation scenario. | 19 |
| 2.2 | Multi-antenna interference. | 20 |
| 2.3 | BS and MS angular parameters. | 26 |
| 2.4 | Fading over time for SISO flat-fading channels. | 31 |
| 3.1 | Simplified schematics diagram for SC-FDMA. | 48 |
| 3.2 | Simplified schematics diagram for SC-FDMA using the JGA in the frequency domain. | 52 |
| 3.3 | JGA Schematics Diagram. | 55 |
| 3.4 | Extended JGA Schematics Diagram. | 57 |
| 3.5 | SC-FDMA JGA Schematics Diagram. | 59 |
| 3.6 | SC-FDMA JGA Schematics Diagram 2. | 59 |
| 4.1 | Schematics diagram for a multipath communication system. | 63 |
| 4.2 | Histogram of LLRs at the output of an equalizer for positive trans- mitted BPSK symbols at 20 dB. | 64 |
| 4.3 | BER curves for AWGN and multipath channels (SNRs for multipath channel shown above points). | 65 |
| 4.4 | Theoretical and simulated BER performances for uncoded BPSK trans- mission over test channel A. | 66 |

LIST OF FIGURES

| | | |
|------|------------------------------------------------------------------------------------------------------------------------------------|----|
| 4.5 | QPSK Constellation. | 67 |
| 4.6 | Signal constellation for a $[0.8, 0.6]$ channel with BPSK modulation. . . | 69 |
| 4.7 | Histogram of LLRs at the output of an extended JGA equalizer for positive transmitted BPSK symbols at 15 dB. | 71 |
| 4.8 | BER performance for the extended JGA with $x[k - 1]$ removed from the interference pool for channel test A. | 72 |
| 4.9 | BER performance for the extended JGA with $x[k - 1]$ and $x[k + 1]$ removed from the interference pool for channel test A. | 72 |
| 4.10 | Mutual information as a function of σ_i | 75 |
| 4.11 | EXIT charts for “open-tunnel” and “intersection” scenarios. | 76 |
| 4.12 | EXIT curves for a JGA detector obtained via approximation and via histogram analysis. | 77 |
| 4.13 | EXIT charts for equalizers using the JGA and the extended JGA. . . . | 78 |
| 5.1 | Performance curves for different equalizers over test channel A (uncoded system). | 81 |
| 5.2 | Iterative equalization system schematics diagram. | 81 |
| 5.3 | Performance curves for an iterative equalization system using the JGA. | 82 |
| 5.4 | Iterative convolutional extended JGA. | 83 |
| 5.5 | Iterative convolutional JGA and extended JGA (regular and LC implementations) for the test channel A. | 83 |
| 5.6 | SINR (JGA) X SINR (EJGA) for suburban macrocell channels. | 85 |
| 5.7 | SINR (JGA) X SINR (EJGA) for urban macrocell channels. | 85 |
| 5.8 | SINR (JGA) X SINR (EJGA) for urban microcell channels. | 86 |
| 5.9 | SINR (JGA) X SINR (EJGA) for 2X2 MIMO urban macrocell channels. | 88 |
| 5.10 | SINR (JGA) X SINR (EJGA) for 2X2 MIMO suburban macrocell channels. | 89 |
| 5.11 | SINR (JGA) X SINR (EJGA) for 2X2 MIMO urban microcell channels. | 89 |

LIST OF FIGURES

| | | |
|------|--------------------------------------------------------------------------------------------------------------------------------------------------------------------------------------------------------------------------------------------------|-----|
| 5.12 | EXIT curves for LTE turbo decoders with CQIs 1-6. | 91 |
| 5.13 | EXIT curves for LTE turbo decoders with CQIs 7, 8, and 9. | 92 |
| 5.14 | Percentage of channels per CQI for the iterative JGA (light colours) and iterative extended JGA (dark colours) for the urban macrocell (left, red), suburban macrocell (center, green), and urban microcell (right, blue) scenarios. | 92 |
| 5.15 | Percentage of channels per CQI for the non-iterative JGA (light colours) and iterative JGA (dark colours) for the urban macrocell (left, red), suburban macrocell (center, green), and urban microcell (right, blue) scenarios. | 93 |
| 5.16 | Percentage of channels per CQI for the non-iterative JGA (light colours) and iterative extended JGA (dark colours) for the urban macrocell (left, red), suburban macrocell (center, green), and urban microcell (right, blue) scenarios. | 94 |
| 5.17 | Schematics Diagram for a 2×2 MIMO multipath communication system. | 94 |
| 5.18 | EXIT chart for the JGA, the extended JGA, and the decoder (inter-changed axis). | 95 |
| 5.19 | BER curves for iterative systems applying the JGA and the extended JGA for a channel specified by the coefficients in Table 5.6. | 96 |
| A.1 | Constellation mappings. | 108 |
| B.1 | HSDPA physical layer schematics diagram. | 113 |
| B.2 | HSDPA transmitted packet structure. | 114 |
| B.3 | Packet transmission for a CQI of 15. | 117 |
| B.4 | HSDPA turbo encoder. | 118 |
| B.5 | Turbo decoder schematics diagram. | 118 |

LIST OF FIGURES

| | | |
|-----|----------------------------------------------|-----|
| B.6 | Rake receiver with three “fingers” | 121 |
| C.1 | LTE basic resource block. | 124 |
| C.2 | Frame structure | 125 |
| C.3 | LTE uplink schematic diagram. | 127 |
| C.4 | Feedback Shift Register. | 128 |

List of Abbreviations

3GPP Third Generation Partnership Project

ACK Acknowledgment (for HARQ schemes)

ARQ Automatic repeat request

AWGN Additive white Gaussian noise

BCJR Bahl-Cocke-Jelinek-Raviv (decoding algorithm)

BER Bit error rate

BS Base station

CLT Central limit theorem

CQI Channel quality indicator

CRC Cyclic redundancy check

DFE Decision-feedback equalization

DRP Dithered relative prime

EJGA Extended jointly Gaussian approach

FER Frame error rate

FPGA Field-programable gate array

HARQ Hybrid automatic repeat request

HSPA High speed packet access

HSPA+ Evolved high-speed packet access

HSDPA High speed downlink packet access

HS-DPCCH High speed-dedicated physical control channel

HS-PDSCH High speed-physical downlink shared channel

i.i.d. Independent and identically distributed

JGA Jointly Gaussian approach

LE Linear equalization

LLR Log-likelihood ratio

LOS Line-of-sight

LTE Long-term enhancement

MAI Multi antenna interference

MAP Maximum *a posteriori*

MIMO Multiple-input multiple-output

ML Maximum likelihood

MS Mobile station

NACK Negative acknowledgment (for HARQ schemes)

PAPR Peak-to-average power ratio

OFDM Orthogonal frequency-division multiplexing

SC-FDMA Single-carrier frequency-division multiple access

SCM Spatial channel model

SISO Single-input single-output

SNR Signal to noise ratio

SINR Signal to interference-plus-noise ratio

TBS Transport block size

TTI Transport transmission interval

WSSUS Wide-sense stationary uncorrelated scattering

1

Introduction

The ever-growing demand for higher data rates in mobile communication networks requires the use of all resources that can be offered by the wireless channel. In this regard, two methods that can significantly augment the overall information throughput are the use of increasingly higher bandwidths, as well as the use of multiple-input multiple-output (MIMO) technology. In fact, thanks to their potential to dramatically increase the transmission rate, both methods have been included in a number of mobile communication standards, e.g., the High-Speed Packet Access (HSPA) [1], the Long Term Evolution (LTE) [2], and the Worldwide Interoperability for Microwave Access (WiMAX) [3].

A problem that arises with the use of channels with large bandwidth and/or MIMO technology is that of interference. Transmission of data over channels with large bandwidth is more prone to suffer from the effects of multipath propagation, resulting in a phenomenon known as intersymbol interference (ISI). For MIMO systems, the signals conveyed by each transmitting antenna will interfere with one another at the receiving antennas, resulting in multi-antenna, or spatial, interference (MAI). When these two methods are combined, both sources of interference, i.e., ISI and MAI, are also combined. Interference, if not properly taken care of, can greatly degrade the performance of the communication system.

In digital communication systems, the transmitter sends discrete-time symbols that are modulated and multiplied by a carrier, or in other words up-converted, to be transmitted over the channel. Also, the sampled outputs of the matched filter at

the receiver are discrete-time symbols. Therefore, although interference from multiple paths and/or antennas is a continuous phenomenon in its nature, the concatenation of up-converter, multipath MIMO channel, down-converter, matched filter and sampler can be modelled by a discrete-time filter H followed by additive Gaussian noise [4], as seen in Figure 1.1 for a single-input single-output (SISO) system.

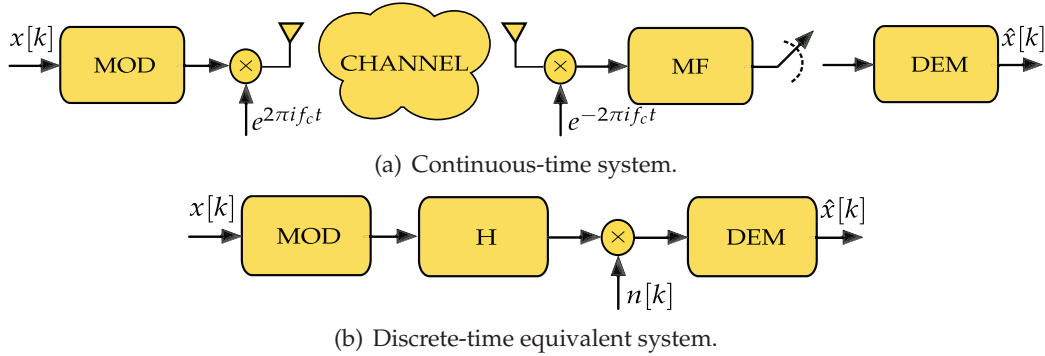


Figure 1.1: Digital communication system schematics diagram.

A literature overview of classical methods to counteract the effects of ISI, MAI and combined ISI and MAI is presented in what follows. For all methods presented, a discrete-time channel model, as shown in Figure 1.1(b) is assumed.

1.1 Classical equalization schemes for multipath channels

The reasoning behind increasing the bandwidth of the signal to be transmitted, in order to enhance the overall throughput, traces back to the seminal work of Shannon [5]. In this seminal paper, Shannon proved that the capacity of a Gaussian channel corrupted by additive white Gaussian noise (AWGN) grows linearly with the bandwidth available, but only logarithmically with the available power, according to

$$C = B \log_2 \left(1 + \frac{P}{BN_0} \right), \quad (1.1)$$

where B denotes the available bandwidth, P the total available power and N_0 the power of the noise.

Increasing the channel's bandwidth, as already discussed, makes the channel more prone to suffer from the effects of multipath propagation. In the frequency domain,

the introduction of multiple paths results in a non-flat channel frequency response. For such scenario, the channel's capacity can be calculated according to [6]

$$C = \max_{P(f): \int P(f)df \leq P} \int \log_2 \left(1 + \frac{|H(f)|^2 P(f)}{N_0} \right) df, \quad (1.2)$$

where $P(f)$ denotes the power allocation over the frequency spectrum and $H(f)$ the channel's frequency response.

The optimal power allocation over the frequency spectrum follows the water-filling algorithm [6], as shown in Figure 1.2. Clearly, for a normalized channel with flat frequency response, $H(f) = 1$ for all frequencies, making $P(f) = P/B$.

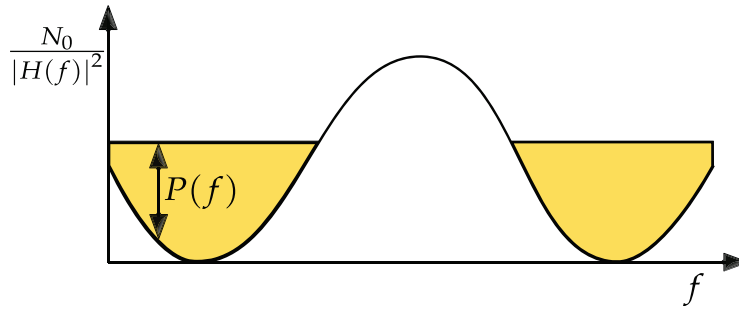


Figure 1.2: Water-filling for frequency selective channels.

It can be shown, using the Cauchy-Schwarz inequality, that for normalized channels, i.e., channels for which $\int |H(f)|^2 df = 1$, the capacity of a frequency-selective channel is always smaller than the capacity of a Gaussian channel.

Besides decreasing the theoretical capacity of the channel, multipath propagation also makes the task of achieving this capacity harder. For a communication system over a multipath channel to approach the channel's capacity, a coding scheme that takes into account the correlation between consecutive received symbols is necessary. However, taking correlation between neighbouring symbols into account greatly increases the complexity of the decoding process. The practical approach, therefore, is to separate the tasks of equalization and decoding (for an encoded system), performing each one independently.

A large body of research has been dedicated to develop practical equalization methods. These methods can be divided into three classes, Linear Equalization (LE), Decision-Feedback Equalization (DFE) and Maximum Likelihood Sequence Estimation (MLSE). A brief description of these classes is presented in what follows.

1.1.1 Linear equalizers

Linear equalization consists in passing the received sequence through a linear filter with a fixed length $N = N_1 + N_2 + 1$ (N_1 anticausal and $N_2 + 1$ causal taps). Denoting the k th received symbols by $y[k]$ and the i th filter's coefficient by $w[i]$, the output of the equalizer is given by

$$\tilde{x}[k] = \sum_{i=-N_1}^{N_2} w[i]y[k-i]. \quad (1.3)$$

Ideally, the coefficients $w[i]$ should be calculated in order to minimize the probability of detection error. However, it is virtually impossible to optimize the values of $w[i]$ according to this criterion. Thus, two indirect optimization criteria have been proposed in the literature, Zero-Forcing (ZF) and Minimum Mean Squared Error (MMSE) [6].

Zero-forcing equalization aims to remove all ISI from the observed signal. This is accomplished by a filter whose coefficients $w[i]$ are such that its frequency response is exactly the inverse of that of the channel. Denoting the channel's frequency response by $H(\omega)$, the filter's frequency response is given by

$$F(\omega) = \frac{1}{H(\omega)}. \quad (1.4)$$

Although all ISI is removed, it can be shown that this filter can greatly enhance the variance of the noise at its output, calculated according to (1.5) [6]. Looking at this expression, it is easy to see that if $H(\omega)$ is close to zero for a given range of frequencies, the power of the noise after the equalizer is greatly enhanced. Moreover, if $H(\omega)$ has a null, ZF equalization becomes impossible.

$$\sigma_n^2 = \int_0^B \frac{N_0}{H(\omega)} d\omega. \quad (1.5)$$

Because of this noise enhancement effect present in ZF equalizers, another criterion that shows a balance between inverting the channel and keeping noise enhancement at an acceptable level has been proposed. It is the MMSE criterion. In an MMSE equalizer, the coefficients $w[i]$ are calculated to minimize the mean squared error between the output of the equalizer and the transmitted signal. Mathemati-

cally, the coefficients $w[i]$ are selected in order to minimize $E [|x[k] - \tilde{x}[k]|^2]$ for all values of k . It can be shown that the filter that follows this criteria has a frequency response given by [6]

$$F(\omega) = \frac{1}{H(\omega) + N_0}, \quad (1.6)$$

where N_0 denotes the power of the noise. Clearly, this extra factor in the denominator guarantees that the power of the noise at the filter's output is always finite. Nevertheless, the noise enhancement effect isn't completely mitigated and part of the ISI is now left uncompensated.

1.1.2 Decision-feedback equalizers

Decision-Feedback Equalization (DFE) is a non-linear method that aims to mitigate ISI using two filters and a decision device. First, channel observations, $y[k]$, are passed through a feedforward filter. Then, the output of the feedback filter is subtracted from the output of this filter, resulting in $\tilde{x}[k]$. Finally, this result is mapped into one of the symbols in the transmitted signal constellation, $\hat{x}[k]$, by a decision device. These hard-decisions are used as input to the feedback filter, as seen in Figure 1.3.

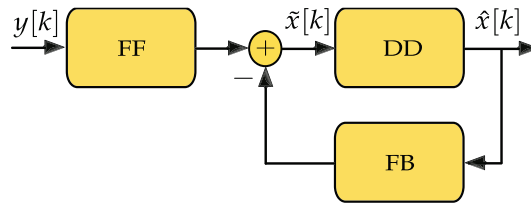


Figure 1.3: Decision Feedback Equalizer.

It was shown in [7] that the optimal feedforward filter $FF(\omega)$ for a ZF DFE is a noise whitening filter. In this case, the feedback filter's frequency response $FB(\omega)$ should be equal to the whitened channel's response $H(\omega)FF(\omega)$.

Since the feedback filter is an estimate of the channel, instead of its inverse, it doesn't incur any noise enhancement. However, decision errors propagate on the feedback loop, potentially leading to follow-up errors. Because of it, ZF DFE normally performs better than MMSE LE for average to high SNRs, but shows a poorer performance for low SNRs [4].

1.1.3 Maximum likelihood sequence estimation

In a Maximum Likelihood Sequence Estimation (MLSE) process, the input sequence x that maximizes the likelihood of the received sequence y is chosen. In other words, a specific sequence x , out of all possible transmitted sequences, is selected so that $P(y|x)$ is maximized.

Clearly, the straightforward way of estimating the transmitted sequence based on this criterion is to compare $P(y|x_i)$ for every possible sequence x_i . However, for any sequence of practical size (normally between 10^2 to 10^5 symbols), this task is computationally infeasible since it would require 2^{mN} comparisons, where m denotes the modulation order¹ and N the size of the transmitted sequence.

The Viterbi algorithm [8] is able to estimate the maximum likelihood sequence by treating the channel as a hidden Markov model, reducing the number of comparisons to only 2^{mL} per detected symbol, where L denotes the memory of the discrete-time multipath channel model.

An equalizer based on the Viterbi algorithm works by following paths on a trellis representing the possible states of the multipath channel. Whenever two or more paths arrive at the same state, the one that produces the output sequence closest to the received signal is chosen, while all other paths are eliminated. Closest here means closest in the Euclidean sense, i.e., the path that produces an output sequence \hat{y} for which $\sum_{i=0}^{N_T} |y[k] - \hat{y}[k]|^2$ is minimal is selected.

MLSE is optimal in the sense of resulting in the smallest possible Bit Error Rate (BER) [4]. However, its complexity grows exponentially with the memory of the channel. Therefore, it quickly becomes impractical as the value of L increases.

MAP equalization

If *a priori* information is available at the equalizer's input, it can be taken into account by a Maximum *a Posteriori* (MAP) algorithm proposed by Bahl *et al* [9] known as the BCJR algorithm. As it will be shown later in this work, the use of *a priori* information is *conditio sine qua non* for iterative equalization.

¹The modulation order is defined as the base 2 logarithm of the number of symbols in the signal constellation, e.g., one for binary phase-shifting keying (BPSK), two for quadrature phase-shifting keying (QPSK), and four for 16 quadrature amplitude modulation (16 QAM).

The BCJR algorithm minimizes the BER, in the presence of *a priori* information, by maximizing the probability of each decoded symbol $\hat{x}[k]$ being equal to the transmitted symbol $x[k]$, given the received sequence \mathbf{y} , i.e., this algorithm can be used to solve the following optimization problem,

$$\max_{\hat{x}[k]} P(\hat{x}[k] = x[k] | \mathbf{y}). \quad (1.7)$$

To solve this problem, the BCJR algorithm calculates log-likelihood ratios (LLRs) for each transmitted symbol. Mathematically, the LLR of a given transmitted symbol $x[k]$ is defined as

$$L(x[k]) = \log \left[\frac{P(x[k] = +1 | \mathbf{y})}{P(x[k] = -1 | \mathbf{y})} \right]. \quad (1.8)$$

Applying the Bayes' rule to both numerator and denominator of (1.8) results in

$$P(x[k] = +1 | \mathbf{y}) = \frac{P(x[k] = +1, \mathbf{y})}{P(\mathbf{y})} = \frac{P(\mathbf{y} | x[k] = +1) P(x[k] = +1)}{P(\mathbf{y})} \quad (1.9)$$

and

$$P(x[k] = -1 | \mathbf{y}) = \frac{P(x[k] = -1, \mathbf{y})}{P(\mathbf{y})} = \frac{P(\mathbf{y} | x[k] = -1) P(x[k] = -1)}{P(\mathbf{y})}. \quad (1.10)$$

Using the results in (1.9) and (1.10), (1.8) can be rewritten as

$$L(x[k]) = \log \left[\frac{P(\mathbf{y} | x[k] = +1) P(x[k] = +1)}{P(\mathbf{y} | x[k] = -1) P(x[k] = -1)} \right]. \quad (1.11)$$

The BCJR algorithm works by representing the output \mathbf{v} of the multipath channel, after being fed by a transmitted signal \mathbf{x} , but before the addition of the noise term, by a path in a trellis structure. Using this trellis structure, (1.9) can be rewritten as

$$P(x[k] = +1 | \mathbf{y}) = \frac{P(x[k] = +1, \mathbf{y})}{P(\mathbf{y})} = \frac{\sum_{(s',s) \in S_k^+} P(s[k] = s', s[k+1] = s, \mathbf{y})}{P(\mathbf{y})}, \quad (1.12)$$

where $\sum_{(s',s) \in S_k^+}$ represents the space of all transitions from states $s[k] = s'$ and $s[k+1] = s$ for which $x[k] = +1$.

Using (1.12) in (1.8) results in

$$L(x[k]) = \left[\frac{\sum_{(s',s) \in S_k^+} P(s',s,\mathbf{y})}{\sum_{(s',s) \in S_k^-} P(s',s,\mathbf{y})} \right] \quad (1.13)$$

It is possible to calculate (1.13) in a recursive fashion. In order to do so, the received sequence has to be broken in three parts, as seen below

$$\begin{aligned} P(s',s,\mathbf{y}) &= P(s',s,\mathbf{y}[t < k], y[k], \mathbf{y}[t > k]) \\ &= P(\mathbf{y}[t > k] | s', s, \mathbf{y}[t < k], y[k]) P(s', s, \mathbf{y}[t < k], y[k]) \\ &= P(\mathbf{y}[t > k] | s', s, \mathbf{y}[t < k], y[k]) P(s, y[k] | s', \mathbf{y}[t < k]) P(s', \mathbf{y}[t < k]), \end{aligned} \quad (1.14)$$

where the second and third equalities hold due to Bayes' Rule.

Since $\mathbf{y}[t > k]$ depends only on the future state s , and $y[k]$ depends only on the present state s' , (1.14) can be simplified to

$$\begin{aligned} P(s',s,\mathbf{y}) &= P(\mathbf{y}[t > k] | s) P(s, y[k] | s') P(s', \mathbf{y}[t < k]) \\ &= \beta_{k+1}(s) \gamma_k(s', s) \alpha_k(s'), \end{aligned} \quad (1.15)$$

where the terms $\alpha_k(s')$, $\beta_{k+1}(s)$ and $\gamma_k(s', s)$ are defined as

$$\alpha_k(s') \triangleq P(s', \mathbf{y}[t < k]) \quad (1.16a)$$

$$\beta_{k+1}(s) \triangleq P(\mathbf{y}[t > k] | s) \quad (1.16b)$$

$$\gamma_k(s', s) \triangleq P(s, y[k] | s'). \quad (1.16c)$$

The values of $\alpha_k(s')$ and $\beta_{k+1}(s)$ can be calculated using forward and backward recursions, respectively.

$$\begin{aligned}
 \alpha_{k+1}(s) &= P(s, \mathbf{y}[t < k + 1]) \\
 &= \sum_{s' \in \sigma_k} P(s', s, \mathbf{y}[t < k + 1]) \\
 &= \sum_{s' \in \sigma_k} P(s, \mathbf{y}[k] | s', \mathbf{y}[t < k]) P(s', \mathbf{y}[t < k]) \\
 &= \sum_{s' \in \sigma_k} P(s, \mathbf{y}[k] | s') P(s', \mathbf{y}[t < k]) \\
 &= \sum_{s' \in \sigma_k} \gamma_k(s', s) \alpha_k(s').
 \end{aligned} \tag{1.17}$$

$$\begin{aligned}
 \beta_k(s') &= P(\mathbf{y}[t > k - 1] | s') = P(\mathbf{y}[k], \mathbf{y}[t > k] | s') \\
 &= \sum_{s \in \sigma_{k+1}} P(s, \mathbf{y}[k], \mathbf{y}[t > k] | s') \\
 &= \sum_{s \in \sigma_{k+1}} P(\mathbf{y}[t > k] | s, s', \mathbf{y}[k]) P(s, \mathbf{y}[k] | s') \\
 &= \sum_{s \in \sigma_{k+1}} P(\mathbf{y}[t > k] | s) P(s, \mathbf{y}[k] | s') \\
 &= \sum_{s \in \sigma_{k+1}} \beta_{k+1}(s) \gamma_k(s', s).
 \end{aligned} \tag{1.18}$$

In (1.17) and (1.18), σ_k and σ_{k+1} represent the set of all possible states s' and s , respectively.

To calculate $\gamma_k(s', s)$, its equation is rewritten as

$$\begin{aligned}
 \gamma_k(s', s) &= P(s, \mathbf{y}[k] | s') = \frac{P(s, \mathbf{y}[k], s')}{P(s')} \\
 &= \frac{P(s', s)}{P(s')} \times \frac{P(s, \mathbf{y}[k], s')}{P(s', s)} \\
 &= P(s | s') P(\mathbf{y}[k] | s', s).
 \end{aligned} \tag{1.19}$$

Since the output $v[k]$ of the multipath channel is completely determined by the transition from a state s' to another state s , (1.19) is equivalent to

$$\gamma_k(s', s) = P(s | s') P(\mathbf{y}[k] | v[k]). \tag{1.20}$$

Finally, given a certain state s' , the transition to a future state s is fully specified by the input $x[k]$. Thus, (1.20) can be rewritten as

$$\gamma_k(s', s) = P(x[k])P(y[k]|v[k]) \quad (1.21)$$

Clearly, the term $P(x[k])$ corresponds to the *a priori* information regarding the input symbol $x[k]$. If no *a priori* information is available, $P(x[k]) = 0.5$ is assumed for all values of k . The term $P(y[k]|v[k])$ depends on the noise. For the AWGN case, (1.21) is given by [10]

$$P(y[k]|v[k]) \propto \exp\left(-\frac{E_b}{N_0} (y[k] - v[k])^2\right). \quad (1.22)$$

Complexity analysis of MLSE and MAP equalization

As shown above, both MLSE and MAP equalization schemes work by using a trellis representation of the channel with 2^{mL} possible states. As a result, optimal detection for multipath channels rapidly becomes impractical as the modulation order, and/or the channel memory values increase. In order to address this issue, several sub-optimal techniques have been proposed to reduce the complexity of MLSE and MAP detection of signals through ISI channels with large delay spread.

The delayed decision-feedback sequence estimator (DDFSE), proposed independently in [11] and [12], reduces the complexity of MLSE detection by constructing the channel trellis taking into account only the first μ taps. At each state of the channel trellis, the interference introduced by the remaining $L - \mu$ taps is taken into account by making hard-decisions on the sequence of symbols that lead to that particular state, and cancelling it from the received signal. Hence, this algorithm works exactly like a Viterbi algorithm when $\mu = L$ and as a DFE when $\mu = 0$. This method works particularly well for channels with most of its energy concentrated in the first taps.

Reduced-complexity BCJR-like algorithms were proposed in [13, 14], these algorithms reduce the overall complexity of the equalization process by only following the most promising paths in the channel trellis. The M-BCJR method presented in [13], as the DDFSE, achieves great performance when most of the energy is concentrated in the first few taps. For the three methods presented in [14], on the other hand, this minimum-phase constraint isn't necessary. However, trellises cre-

ated by these methods are highly irregular, as opposed to the ones created by MAP or DDFSE schemes, making the implementation of these methods in hardware a challenge.

1.2 MIMO communications

MIMO technology has gained a lot of attention from the specialized literature, as well as industry, over the last decade. It can be shown that, by using arrays of antennas at each end of the communication link between transmitter and receiver, a new channel with a greater capacity is virtually created [15]. For instance, the use of multiple antennas can increase the overall throughput by transmitting independent data streams over each antenna at the transmitter, resulting in what is called multiplexing gain. MIMO technology can also increase the reliability of the communication link, by sending copies of the same data stream over all transmitting antennas, resulting in diversity gain. Space-time coding can be used to achieve a trade-off between multiplexing and diversity gain. For a comprehensive introduction of MIMO communication systems, the reader is referred to [16, 17].

In this work, spatial multiplexing, i.e., transmission of independent data streams from each transmitting antenna is assumed. For this scenario, at each antenna at the receiver, information sent by each transmitting antenna interferes with one another. Hence, it is the receiver's task to filter the interference and obtain an estimative of the transmitted signal. In what follows, some classical detection methods for flat MIMO channels are presented.

1.2.1 Maximum likelihood detection

Assuming an $N_R \times N_T$ MIMO system with flat frequency response, in other words, free from ISI, the relationship between the received vector \mathbf{y} of size N_R and the transmitted vector \mathbf{x} of size N_T is given by

$$\mathbf{y} = \mathbf{H}\mathbf{x} + \mathbf{n}, \quad (1.23)$$

where \mathbf{H} is an $N_R \times N_T$ matrix of fading coefficients between each pair of transmitting and receiving antennas, and \mathbf{n} denotes a noise vector of size N_R .

Maximum likelihood detection requires finding a specific vector x , among all possible 2^{mN_T} transmitted vectors, that minimizes

$$\|\mathbf{y} - \mathbf{H}\mathbf{x}\|_F^2, \quad (1.24)$$

where $\|\cdot\|_F$ indicate the Frobenius norm.

The complexity of this method grows exponentially with the product $m \times N_T$, since this is the number of possible transmitted sequences. Hence, its application is restricted to small signal constellations and/or small number of transmit antennas. This method can be approximated by Sphere Detection Algorithms (SDAs). The basic idea behind SDAs is to restrict the search for the optimal transmitted vector x to a smaller subset of potential candidates, instead of all possible vectors [17]. In the same way as multipath channels, sub-optimal methods can be used to provide a trade-off between complexity and performance. A number of such methods are presented in what follows.

1.2.2 Linear receivers

For a MIMO linear receiver, the received signal \mathbf{y} is multiplied by a matrix \mathbf{A} , resulting in

$$\tilde{\mathbf{y}} = \mathbf{A}\mathbf{y} = \mathbf{A}\mathbf{H}\mathbf{x} + \mathbf{A}\mathbf{n}. \quad (1.25)$$

As in the multipath SISO scenario, this matrix can be chosen to ensure that all interference is removed, resulting in the Moore-Penrose pseudoinverse zero-forcing matrix² $\mathbf{A} = (\mathbf{H}^\dagger \mathbf{H})^{-1} \mathbf{H}^\dagger$ [17], or to minimize the mean squared error, resulting in $\mathbf{A} = (\mathbf{H}^\dagger \mathbf{H} + \sigma^2 \mathbf{I})^{-1} \mathbf{H}^\dagger$. Also, as in the multipath SISO scenario, the computational complexity reduction obtained by linear detectors come at the expense of poor performance for some channels [18].

1.2.3 Decision-feedback receivers

A method tantamount to decision-feedback equalization for multipath SISO channels can be applied to the reception of signals over MIMO channels. First, the

²Complex conjugates are denoted by \dagger .

channel matrix is decomposed in the form

$$\mathbf{H} = \mathbf{Q}\mathbf{R}, \quad (1.26)$$

where the $N_R \times N_T$ matrix \mathbf{Q} is orthogonal, i.e., $\mathbf{Q}^\dagger\mathbf{Q} = \mathbf{I}$, and \mathbf{R} is an $N_T \times N_T$ upper triangular matrix [19].

Using this decomposition, it is clear that $\tilde{\mathbf{y}} = \mathbf{Q}^\dagger\mathbf{y}$ is given by

$$\tilde{\mathbf{y}} = \mathbf{R}\mathbf{x} + \tilde{\mathbf{n}}, \quad (1.27)$$

where $\tilde{\mathbf{n}} = \mathbf{Q}^\dagger\mathbf{n}$ retains the same statistical properties of \mathbf{n} [16].

Using the upper diagonal structure of \mathbf{R} , the detection process works as follows. First, the symbol transmitted by the N_T th transmitting antenna, x_{N_T} , is detected by minimizing $|\tilde{y}_{N_T} - r_{N_T,N_T}x_{N_T}|^2$. Following, the hard-decision \hat{x}_{N_T} is used to detect x_{N_T-1} , by minimizing $|\tilde{y}_{N_T-1} - r_{N_T-1,N_T-1}x_{N_T-1} - r_{N_T-1,N_T}\hat{x}_{N_T}|^2$. The method proceeds by making hard-decisions on the detected symbols, one by one, and cancelling the interference introduced by these symbols in $\tilde{\mathbf{y}}$ until x_1 is detected. Clearly, as in the multipath SISO scenario, this method is prone to suffer from error propagation. The performance of this method can be improved by optimizing the antenna labeling in such a way that the most powerful signals are detected first. A very popular method to achieve this goal is the Vertical-Bell Laboratories Layered Space-Time (V-BLAST) method presented in [20].

1.3 Equalization schemes for multipath MIMO systems

For multipath MIMO systems, interference comes from two different dimensions, spatial (MAI) and temporal (ISI). In such scenario, ML and MAP equalizers have a complexity that grows exponentially with the product $m \times N_T \times L$, becoming impractical even for small values of these parameters. As a result, practical methods for equalization of multipath MIMO systems have been proposed in literature over the past few years.

Orthogonal frequency-division multiplexing (OFDM) is a method used to avoid the exponential complexity growth due to ISI. OFDM works by turning a multipath MIMO channel into a set of parallel flat frequency response MIMO channels [6]. Because of its potential, OFDM has been included in the WiMAX standard and in

the downlink for the LTE standard. Nevertheless, OFDM transmissions are very sensitive to carrier frequency synchronization and, more importantly, have a high Peak-to-Average Power Ratio (PAPR). Hence, they are not suited for the uplink of cellular networks, where the transmitter is normally a battery powered device [21].

The expression for the relationship between transmitted and received signals in (1.23) can be extended to frequency-selective MIMO systems, as discussed in details in Chapter 2. Hence, ZF and MMSE linear receivers, as well as decision-feedback receivers, can be readily extended to work in this scenario. However, as in the flat frequency response MIMO scenario, these methods can lead to poor error rate performances.

A method to enhance performance of detectors for both multipath SISO and multipath MIMO channels, dubbed iterative equalization, has gained a lot of attention lately. This method consists in dividing the task of detecting the transmitted signal in smaller parts that exchange extrinsic information in an iterative fashion. In the following section, iterative equalization is presented, first for multipath SISO channels, and later, extended to multipath MIMO scenarios.

1.4 Iterative equalization

In 1993, a groundbreaking result in error control coding was presented by Berrou *et al* [22]. With the introduction of a new class of codes, called turbo codes, together with the introduction of an iterative decoder method, it was possible for the first time to approach the theoretical bounds for error-free communication over noisy channels predicted by Shannon [5].

A few years after the introduction of turbo codes, Douillard *et al* showed that the iterative decoding technique introduced in [22] could also be applied to the detection of encoded information transmitted over multipath channels [23].

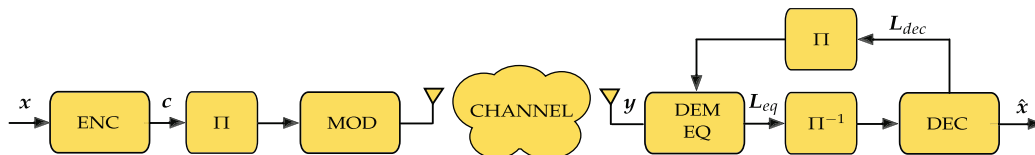


Figure 1.4: Iterative equalization system schematics diagram.

A schematics diagram of the iterative equalization system proposed in [23] can be seen in Figure 1.4. This system work as follows. The signal x to be transmitted is first encoded by an error-control code, resulting in c . This encoded message is interleaved, in order to remove the correlation between neighbouring encoded bits, modulated, and transmitted over the channel. At the receiver, the demodulator/equalizer block and the decoder exchange extrinsic information about the received signal for a given number of iterations. After the final iteration, hard-decisions are taken on the LLRs produced by the decoder, resulting in \hat{x} .

The demodulator/equalizer block takes into account a sequence of observations, y , and an interleaved version of the LLRs produced by the decoder, L_{dec} . Then, it outputs a sequence of extrinsic LLRs³, L_{eq} . These extrinsic LLRs, after interleaving, serve as an input for the decoder. The decoder will process this information into a new sequence of LLRs, L_{dec} , that, after de-interleaving, serve as a new set of *a priori* information for the equalizer. This process continues until a pre-determined number of iterations take place.

In Douillard *et al*'s proposed system, a convolutional code is used and the equalizer uses a Soft-Output Viterbi Algorithm (SOVA) [24] to calculate extrinsic LLRs. A few years after this pioneering work, Bauch *et al* [25], published a work where the BCJR algorithm is used, instead of the SOVA, to extract extrinsic LLRs from the received signal and the available *a priori* information. Using a convolutional code of memory $L = 4$ and a random interleaver of size 4096, Bauch *et al* showed that for a BER of 10^{-4} , this iterative equalization system performed, after 8 iterations, 5.6 dB better than a non-iterative system, for a multipath channel described by taps $[0.227, 0.460, 0.680, 0.460, 0.227]$.

Despite the astonishing improvement in performance obtained by performing iterations between equalizer and decoder, iterative systems using MLSE or MAP equalizers often result in a prohibitive computational load. In fact, as discussed before, with a computational complexity that grows proportionally to 2^{mL} , MLSE and MAP equalization quickly become infeasible for large constellations and/or long memory multipath channels. This problem is only aggravated by the fact that iterative systems need to perform equalization and decoding several times until a specified number of iterations is met. Hence, a large body of research has been dedicated to the search of equalization methods suited for iterative systems, without

³Extrinsic LLRs are calculated taking into account the *a priori* information about all symbols but the one under detection, for each symbol.

incurring in prohibitive computational loads.

In order to keep complexity at reasonable levels, Berthet *et al* [26] adapted a DDFSE to be used in iterative equalization systems. To improve performance, an all-pass prefilter is used before the DDFSE. This prefilter turns the multipath channel into a minimum-phase channel, so that the energy on the first taps is maximized, while the frequency response is kept the same. For some channels, however, this all-pass filter might not be able to concentrate enough energy on the first taps and the system is prone to suffer from error propagation effects.

For multipath MIMO systems, Visoz [27] proposed a scheme that performs MIMO data detection and channel equalization in a disjoint but iterative fashion. This method works as follows. First, a MIMO data detector is activated. Following, each data stream is equalized and extrinsic information obtained at the output of each stream is sent back to the MIMO detector until a certain number of iterations take place. This method can achieve great performance for channels mildly corrupted by ISI, but tend to perform poorly for channels where ISI is a major source of disturbance. The reason being that, for this scenario, the output of the MIMO data detector is unreliable for the first iteration.

A detection scheme based on the MMSE criterion was proposed by Wang and Poor [28] for code-division multiple access (CDMA) signals over multipath MIMO channels. It allows MMSE detection to take into account *a priori* information and produces LLRs at its output. Therefore, it is well-suited to take part in an iterative detection scheme coupled with a soft-input soft-output decoder. Tuchler *et al* [29] adapted Wang and Poor's method for non-coded transmission over multipath SISO channels. Simulations indicate that the application of their method for iterative detection results in only a small performance degradation for some channels, as compared to MAP estimation, while providing a huge complexity reduction.

Another detection method, closely related to the MMSE approach proposed in [28, 29], is the jointly Gaussian approach (JGA). The JGA, which falls into the class of probabilistic data association (PDA) algorithms [30, 31], greatly reduces the complexity of the estimation process by assuming the received symbols to form a set of jointly Gaussian random variables. Like the MMSE approach, this method can take into account *a priori* information and delivers LLRs at its output. Hence, it is well-suited for iterative equalization. It is proven in [32] that the JGA approach is equivalent to the MMSE detector proposed in [29].

The JGA was first proposed in [33] for asynchronous CDMA detection. Later it has been extended to MIMO multipath channels in [32], and to multiuser multipath MIMO channels by the same authors in [34]. In [35], the JGA is performed via a graph-based iterative approach to detect signals transmitted over MIMO multipath channels.

In this work, an extension of the jointly Gaussian approach, dubbed extended JGA, is discussed. This extension, which can be applied to both multipath SISO and MIMO channels, generalizes the JGA, allowing a trade-off between complexity and performance. The novelty of this extended method, with regards to the classical JGA, is that a marginalization over some of the most important interference terms is conducted before applying the Gaussian assumption on the remaining interference. It will be shown that this method, for only a negligible increase in computational complexity, can result in a significant improvement in performance compared to the classical JGA.

1.5 Thesis overview

This thesis is organized as follows. In Chapter 2, a comprehensive discussion about channel modelling is presented. Multipath SISO and MIMO channels are modelled as matrices whose coefficients are obtained using the Spatial Channel Model (SCM). The JGA is explained in details in Chapter 3, paving the way to the introduction of the extended JGA for both SISO and MIMO scenarios. Low-complexity implementation methods, including frequency-domain equalization, are also presented in this chapter that ends with a discussion on the computational complexity of the JGA and the extended JGA. In Chapter 4, the improvement in performance obtained by the extended JGA is analyzed by means of two methods, Signal to Interference-plus-Noise Ratio (SINR) analysis and Extrinsic Information Transfer (EXIT) charts. Simulation results are presented in Chapter 5, confirming the performance gains predicted in Chapter 4, and also presenting average gains in terms of throughput for realistic channels. Conclusions, a summary of original contributions of this work, and a roadmap for future research are presented in Chapter 6.

2

Channel Model

In this chapter, baseband discrete-time models of multipath SISO and MIMO channels are presented. These models are extremely useful in that they allow the use of simple matrix equations to characterize the relationship between transmitted and received discrete-time symbols in digital communication systems.

2.1 Multipath SISO channel model

In this work, coherent detection is assumed. Moreover, the receiver is assumed to have a precise knowledge of both signal phase and symbol timing. Therefore, at time instant k , the received symbol $y[k]$ is equal to a scaled version of the transmitted symbol $x[k]$ and, possible, some echoes of previously transmitted symbols together with noise [6]. Mathematically,

$$y[k] = \sum_{l=0}^{L-1} h[l]x[k-l] + n[k] \quad (2.1)$$

where $h[l]$ denotes the complex channel gain for the l th path (or echo), L denotes the number of paths and $n[k]$ the noise at time instant k .

Echoes can be produced by different effects. Apart from a possible line-of-sight (LOS) path, the transmitted signal can also arrive at the receiver via reflected paths, scattered paths and even diffracted paths. In Figure 2.1, a base station (BS) transmits information over multiple paths to a mobile station (MS) inside a red car.

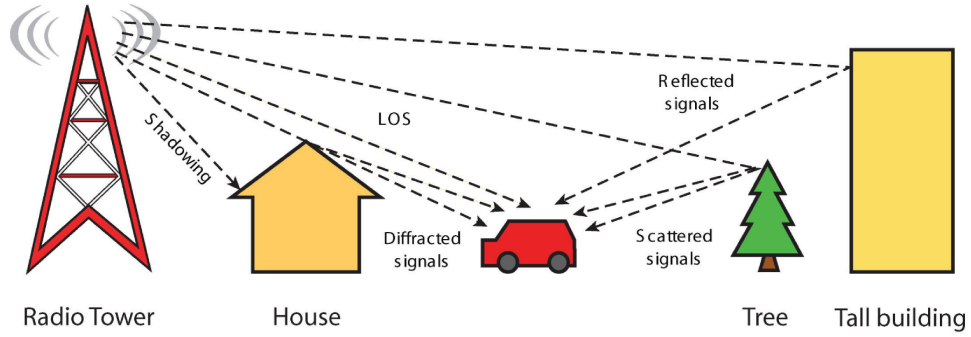


Figure 2.1: Multipath propagation scenario.

Noise in wireless communication systems arises from a multitude of sources: other signals being transmitted at the same frequency, thermal noise, shot noise, etc. In these conditions, the Central Limit Theorem (CLT) is likely to hold. Hence, noise for such systems, is normally modelled as Gaussian.

If a vector \mathbf{x} of K symbols¹ is transmitted, a received vector \mathbf{y} can be obtained according to the following matrix equation

$$\mathbf{y} = \mathbf{H}\mathbf{x} + \mathbf{n}, \quad (2.2)$$

where \mathbf{n} denotes an AWGN noise vector of size K and \mathbf{H} the channel matrix, defined as

$$\mathbf{H} = \begin{bmatrix} h[0] & 0 & \cdots & 0 & \cdots & 0 \\ \vdots & h[0] & \ddots & \vdots & \cdots & \vdots \\ h[L-1] & \vdots & \ddots & 0 & \cdots & \vdots \\ 0 & h[L-1] & \ddots & h[0] & \ddots & 0 \\ \vdots & \vdots & \ddots & \vdots & \ddots & \vdots \\ 0 & 0 & \cdots & h[L-1] & \cdots & h[0] \end{bmatrix}. \quad (2.3)$$

Using the matrix representation of the channel in (2.3), it can be seen that (2.2) implements the convolution shown in (2.1) for all received symbols.

¹In this work, vectors are written in lowercase bold types, while matrices are written in bold type capital letters.

2.2 Multipath MIMO channel model

In a MIMO scenario, at the receiver side, each antenna receives signals transmitted by all antennas at the transmitter side, resulting in MAI. This phenomenon is shown in Figure 2.2 for a 4×4 MIMO transmission system.

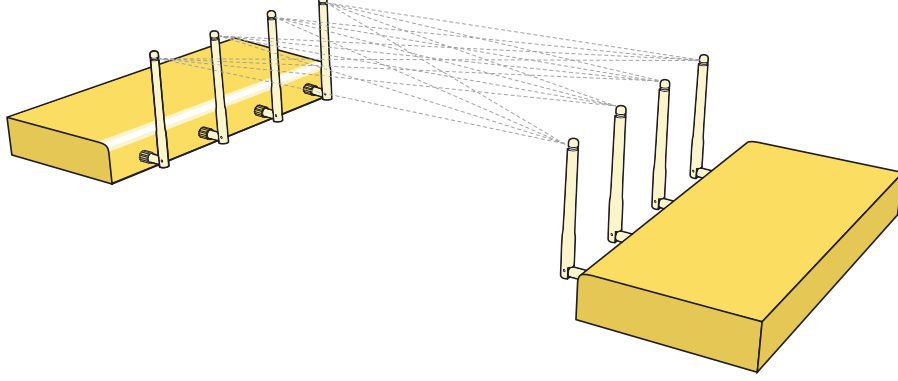


Figure 2.2: Multi-antenna interference.

For a communication system facing both multipath propagation and MAI, let N_T denote the number of transmitting antennas and N_R the number of receiving antennas. Hence, the k th symbol received by the n th receiving antenna, $y_n[k]$, is given according to

$$y_n[k] = \sum_{m=0}^{N_T-1} \sum_{l=0}^{L-1} h^{n,m}[l] x_m[k-l] + n_n[k],$$

where $h^{n,m}[l]$ represents the complex gain of the l th path between the m th transmitting antenna and the n th receiving antenna, $x_m[k]$ denotes the k th symbol transmitted by the m th antenna, and $n_n[k]$ represents the noise received by the n th antenna which is, once again, assumed to be additive white Gaussian.

The set of N_T transmitted symbols at each time instant k is denoted by a column vector $\mathbf{x}[k] = \{x_0[k], \dots, x_{N_T-1}[k]\}^\dagger$. In the same way, the signal received by all N_R receiving antennas is given by $\mathbf{y}[k] = \{y_0[k], \dots, y_{N_R-1}[k]\}^\dagger$, and the noise by $\mathbf{n}[k] = \{n_0[k], \dots, n_{N_R-1}[k]\}^\dagger$. If a sequence of K vectors $\mathbf{x}[k]$ is transmitted, an overall transmitted signal vector, \mathbf{x} , with size $N_T K$, can be created stacking up all vectors $\mathbf{x}[k]$. In the same manner, an overall received signal vector, \mathbf{y} , and an overall noise vector, \mathbf{n} , both with size $N_R K$, can also be created. This procedure of stacking up vectors of transmitted and received signals can be visualized in (2.4), (2.5) and (2.6).

$$\mathbf{x} = \begin{bmatrix} \mathbf{x}[0] \\ \mathbf{x}[1] \\ \vdots \\ \mathbf{x}[K-1] \end{bmatrix} = \begin{bmatrix} x_0[0] \\ \vdots \\ x_{N_T-1}[0] \\ \hline x_0[1] \\ \vdots \\ x_{N_T-1}[1] \\ \hline \vdots \\ x_0[K-1] \\ \vdots \\ x_{N_T-1}[K-1] \end{bmatrix} \quad (2.4)$$

$$\mathbf{y} = \begin{bmatrix} \mathbf{y}[0] \\ \mathbf{y}[1] \\ \vdots \\ \mathbf{y}[K-1] \end{bmatrix} = \begin{bmatrix} y_0[0] \\ \vdots \\ y_{N_R-1}[0] \\ \hline y_0[1] \\ \vdots \\ y_{N_R-1}[1] \\ \hline \vdots \\ y_0[K-1] \\ \vdots \\ y_{N_R-1}[K-1] \end{bmatrix} \quad (2.5)$$

$$\mathbf{n} = \begin{bmatrix} \mathbf{n}[0] \\ \mathbf{n}[1] \\ \vdots \\ \mathbf{n}[K-1] \end{bmatrix} = \begin{bmatrix} n_0[0] \\ \vdots \\ n_{N_R-1}[0] \\ \hline n_0[1] \\ \vdots \\ n_{N_R-1}[1] \\ \hline \vdots \\ n_0[K-1] \\ \vdots \\ n_{N_R-1}[K-1] \end{bmatrix} \quad (2.6)$$

Having defined x , y , and n , the relationship between the transmitted and the received signals, for a MIMO scenario, can also be written in matrix notation as

$$\mathbf{y} = \mathbf{H}\mathbf{x} + \mathbf{n}, \quad (2.7)$$

where \mathbf{H} is a matrix representing the multipath MIMO channel. This matrix is an $N_R K \times N_T K$ convolution matrix

$$\mathbf{H} = \begin{bmatrix} \mathbf{H}[0] & 0 & \cdots & 0 & \cdots & 0 \\ \vdots & \mathbf{H}[0] & \ddots & \vdots & \cdots & \vdots \\ \mathbf{H}[L-1] & \vdots & \ddots & 0 & \cdots & \vdots \\ 0 & \mathbf{H}[L-1] & \ddots & \mathbf{H}[0] & \ddots & 0 \\ \vdots & \vdots & \ddots & \vdots & \ddots & \vdots \\ 0 & 0 & \cdots & \mathbf{H}[L-1] & \cdots & \mathbf{H}[0] \end{bmatrix}, \quad (2.8)$$

where each element $\mathbf{H}[l]$ is an $N_R \times N_T$ matrix with fading coefficients between all pairs of transmitting and receiving antennas for the l th path,

$$\mathbf{H}[l] = \begin{bmatrix} h^{0,0}[l] & h^{0,1}[l] & \cdots & h^{0,N_T-1}[l] \\ h^{1,0}[l] & h^{1,1}[l] & \cdots & h^{1,N_T-1}[l] \\ \vdots & \vdots & \ddots & \vdots \\ h^{N_R-1,0}[l] & h^{N_R-1,1}[l] & \cdots & h^{N_R-1,N_T-1}[l] \end{bmatrix}.$$

In what follows, methods to generate the complex channel gains $h[l]$, for the SISO scenario, and $h^{m,n}[l]$, for the MIMO scenario, are presented.

2.3 Generating channel coefficients

After mathematically modelling transmission over both multipath SISO and MIMO channels via matrix equations, there is still the problem of determining the channel coefficients, $h[l]$ for SISO, and $h^{m,n}[l]$ for MIMO scenarios. This problem has received a lot of attention from specialized literature starting from the early seventies for SISO scenarios, and from the early 2000s for MIMO scenarios.

Wireless channels can be modelled in different ways. For instance, indoor channels can be modelled via ray-tracing techniques taking the local geometry into ac-

count [36]. However, for most purposes, such an approach might be too expensive and often infeasible, especially for outdoor channels. Hence, several statistical models have been proposed in the literature. A few of these models are discussed in this section.

The first difficulty with modelling multipath channels is that, in realistic scenarios, some paths might arrive with delays that are not integer multiples of the sampling time, as (2.1) suggests. Hence, a time variant SISO channel can be described as

$$c(\tau, t) = \sum_{n=0}^{N(t)} a_n(t) e^{-j\phi_n(t)} \delta(t - \tau_n(t)), \quad (2.9)$$

where $N(t)$ denotes the number of paths at instant t , $a_n(t)$ the n th tap gain, $\phi_n(t)$ the arrival angle and $\tau_n(t)$ the delay for the n th tap.

Turin *et al* [37], assumed $\phi_n(t)$ to be uniformly distributed over the interval $[0, 2\pi]^2$ and carried out an experiment in the San Francisco Bay area to obtain the statistics of $a_n(t)$ and $\tau_n(t)$ for four distinct types of areas: A heavily built-up area (downtown San Francisco); A medium-sized city downtown core (downtown Oakland); A small-to-medium city downtown core (downtown Berkeley); Residential suburbs (foothills of residential Berkley).

For all these four areas, an extensive number of meticulously controlled channel measurements were obtained to serve as a database to be analyzed by reduction techniques and curve fitting. Other authors, notably [38], have also used this database to provide slightly different models for multipath wireless channels.

2.3.1 Time delay distribution

Turin [37] has proposed a Poisson hypothesis to model the arrival times of the multiple paths. This model was modified by Suzuki in [38] to better fit the available data. Suzuki also proposed a discrete version of this model using a branching process [39]. Saleh and Valenzuela [40], working on data collected from indoor channels have arrived at a model where rays arrive at the receiver in clusters. According to Saleh and Valenzuela's model, clusters arrive following a Poisson model with a fixed rate Λ . Within each cluster, rays arrive following another Poisson process

²In fact, for almost all frequencies f_c of interest, the signal's wavelength is small enough so that even a few inches can change the phase by a order of 2π .

with a rate λ , where $\Lambda \gg \lambda$.

2.3.2 Fading coefficient distribution

Via statistical analysis of all areas, Turin [37] modelled the amplitude of fading coefficients as having a log-normal distribution,

$$p(a_n(t)) = \frac{1}{\sqrt{2\pi\sigma^2}a_n(t)} \exp\left[-\frac{(\ln(a_n(t)) - \mu)^2}{2\sigma^2}\right], \quad (2.10)$$

where the mean μ and the variance σ^2 decay exponentially as a function of the time delay, and consequently, as a function of n .

Over a spatial dimension of a few hundred wavelengths, it is generally accepted that path strengths follow a Rayleigh distribution [37]. However, Suzuki's analysis [39] showed that even for these scenarios, the log-normal distribution gives a better fit to the experimental data.

For indoor channels, Saleh and Valenzuela [40], modelled the received ray amplitudes as independent Rayleigh random variables with variances that decay exponentially with cluster delay as well as with the delay of each ray within a cluster.

MIMO scenarios

It is shown in [15] that, assuming all links between pairs of transmitting and receiving antennas to be independent, Rayleigh distributed and ISI free, the capacity of MIMO channels scales linearly with the number of antennas. In fact, this independent Rayleigh assumption is largely used in MIMO literature [16, 17, 41]. For realistic wideband MIMO scenarios, however, links between different pairs of transmitting and receiving antennas have spatial correlation as well as dispersion, affecting the system's performance [42].

In [43], each link between pairs of transmitting and receiving antennas is assumed to be a Wide-Sense Stationary Uncorrelated Scattering (WSSUS) Rayleigh fading channel with zero mean and autocorrelation determined by a zeroth-order Bessel function of the first kind. Also, the correlation between two different links is also determined by a zeroth-order Bessel function of the first kind, multiplied by the

correlation coefficients between the two receiving antennas and the correlation coefficients between the two transmitting antennas.

A structured model is proposed in [44]. This model, based on an Eigenvalue Decomposition (EVD) of the MIMO channel, considers correlation in the three dimensions of the propagation channel. This model possesses the advantage of not having to assume scatterers at the receiver to fade independently of those at the transmitter and also considers the correlation between delay bins in the channel's power delay profile.

Additional channel models can be found in [45, 46, 47]. In this work, channel coefficients are generated according to the Spatial Channel Model (SCM) [48], described in details in what follows.

2.4 Spatial channel model

The SCM for MIMO communication systems, presented in a technical report from the 3rd Generation Partnership Project (3GPPTM) [48], is used to generate the complex channel gains for multipath SISO and MIMO channels in this work. This model was chosen for two reasons:

- It takes into account several parameters that affect the properties of the communication channel like: distance between antennas in the arrays of transmitting and receiving antennas, the distance between transmitter and receiver, and the type of cell (i.e., urban microcells, urban macrocells and suburban macrocells), among others. Hence, the SCM permits realistic channels to be generated for specific cases under study;
- It has been adopted by the Wireless World Initiative New Radio (WINNER³), a consortium of telecommunication companies headed by Nokia, to investigate propagation conditions and develop new methods for efficient and flexible spectrum use. Hence, results obtained here can be compared in a straightforward fashion with industry standards.

³<http://www.ist-winner.org/index.html>

of this section. The variable z'_l is a uniform random variable in the interval 0 to $1.2 \mu\text{s}$. These variables are sorted in descending order, i.e., $\tau'_L > \tau'_{L-1} > \dots > \tau'_1$. According to this definition, $\tau'_1 = 0$. The delay from the l th path, denoted by τ_l , is then quantized according to (2.12), where T_C is the duration of a chip interval.

$$\tau_l = \frac{T_C}{16} \left\lfloor \frac{\tau'_l - \tau'_1}{\frac{T_C}{16}} + \frac{1}{2} \right\rfloor. \quad (2.12)$$

All parameters in (2.11) are described in what follows.

Path Loss (P_L) The path loss for urban and suburban macrocells are based on the modified COST 231 Hata-Urban propagation model [49] given by

$$P_L(\text{dB}) = 45.5 + (44.9 - 6.55 \log_{10}(h_{\text{BS}})) \log_{10} \left(\frac{d}{1000} \right) + \quad (2.13) \\ (35.46 - 1.1h_{\text{MS}}) \log_{10}(f_c) - 13.82 \log_{10}(h_{\text{BS}}) + 0.7h_{\text{MS}} + C,$$

where h_{BS} and h_{MS} stands for the BS and MS antenna heights, respectively, in meters. d is the distance between BS and MS, f_c is the carrier frequency in MHz and C a constant factor equal to 0 dB for suburban macrocells and 3 dB for urban macrocells.

For microcells, the path loss is based on the COST 231 Walfish-Ikegami non-line-of-sight (NLOS) model [49]. The following parameters are fixed: $h_{\text{BS}} = 12.5$, $h_{\text{MS}} = 1.5$, building height = 12, building to building distance = 50, street width = 25 and an orientation of 30° for all paths. For these values, the path loss is given by

$$P_L(\text{dB}) = -55 + 38 \log_{10}(d) + \left(24.5 + \frac{1.5}{925} f_c \right) \log_{10}(f_c). \quad (2.14)$$

Power of the l th path (P'_l) Each one of the L paths between each pair of antennas has an unnormalized power given by

$$P'_l = \begin{cases} e^{\frac{(1-r_{\text{DS}})(\tau'_l - \tau'_1)}{r_{\text{DS}} \sigma_{\text{DS}}}} e^{-\frac{\xi_l}{10}}, & \text{for urban and suburban macrocells;} \\ 10^{-\left(\tau_l + \frac{\xi_l}{10}\right)}, & \text{for urban microcells;} \end{cases} \quad (2.15)$$

where $r_{\text{DS}} = 1.4$ for suburban macrocells, $r_{\text{DS}} = 1.7$ for urban macrocells, σ_{DS}

is derived at the end of the section, the shadowing randomization effect, ξ_l , is a zero mean Gaussian random variable with standard deviation of 3 dB, and τ_l is the n th unquantized delay given in units of microseconds.

Log-normal shadow fading coefficient ($\sigma_{SF,l}$) This coefficient is given by

$$\sigma_{SF,l} = 10^{\frac{\sigma_{SH}\gamma_l}{10}}, \quad (2.16)$$

where σ_{SH} is equal to 8 dB for macrocells. For urban microcells it can assume values of 4 dB if there is a LOS, or 10 dB otherwise (NLOS). The values of γ_l are obtained according to a probability distribution that takes into account the correlation between shadowing and delay spread, as seen in Section 2.4.1.

Number of subpaths (M) Each one of the L resolvable paths or echoes is approximated by the SCM model as a sum of 20 unresolvable subpaths.

Angle of departure ($\theta_{l,s}^{AoD}$) Each one of the 20 unresolvable subpaths for each one of the L resolvable paths leaves the BS with a certain departure angle (see Figure 2.3). These angles are obtained by first obtaining the angle for the l th path and then applying the offsets listed in Table 2.1 for each subpath. The angles for the L resolvable paths are taken from the following distributions

$$\rho_l \sim \begin{cases} \eta(0, 1.44\sigma_{AS}^2), & \text{for suburban macrocells;} \\ \eta(0, 1.69\sigma_{AS}^2), & \text{for urban macrocells;} \\ U(-40^\circ, 40^\circ), & \text{for urban microcells;} \end{cases} \quad (2.17)$$

where σ_{AS} is derived at the end of the section. In macrocells, the departure angles are sorted in descending order of its absolute values, i.e., $|\rho_L| > |\rho_{L-1}| > \dots > |\rho_1|$, in such a way that higher angles are associated with higher delays. For microcells, there is no need to order the departure angles.

Angle of arrival ($\theta_{l,s}^{AoA}$) For each resolvable path, each one of the 20 unresolvable subpaths arrives at the MS with a certain angle (see Figure 2.3). As in the case of departure angles, these angles are obtained by first obtaining the angle for the n th path and then applying the offsets listed in Table 2.1 for each subpath. The angles for the N resolvable paths are taken from the distribution $\rho_l \sim \eta(0, \sigma_{l,AoA}^2)$, where $\sigma_{l,AoA} = 104.12(1 - e^{-0.2175|10\log(P_l)|})$ and $\sigma_{l,AoA} = 104.12(1 - e^{-0.265|10\log(P_l)|})$ for macrocells and microcells, respectively. These angles are associated with randomly chosen resolvable paths.

Table 2.1: Sub-path angle offsets for AoD and AoA (for macrocells and microcells).

| # | Macro AoD | Micro AoD | AoA | # | Macro AoD | Micro AoD | AoA |
|----|-----------|-----------|----------|----|-----------|-----------|----------|
| 1 | +0.089° | +0.223° | +1.564° | 2 | -0.089° | -0.223° | -1.564° |
| 3 | +0.282° | +0.706° | +4.944° | 4 | -0.282° | -0.706° | -4.944° |
| 5 | +0.498° | +1.246° | +8.722° | 6 | -0.498° | -1.246° | -8.722° |
| 7 | +0.743° | +1.857° | +13.004° | 8 | -0.743° | -1.857° | -13.004° |
| 9 | +1.025° | +2.564° | +17.949° | 10 | -1.025° | -2.564° | -17.949° |
| 11 | +1.359° | +3.398° | +23.789° | 12 | -1.359° | -3.398° | -23.789° |
| 13 | +1.768° | +4.422° | +30.953° | 14 | -1.768° | -4.422° | -30.953° |
| 15 | +2.296° | +5.740° | +40.182° | 16 | -2.296° | -5.740° | -40.182° |
| 17 | +3.038° | +7.597° | +53.181° | 18 | -3.038° | -7.597° | -53.181° |
| 19 | +4.310° | +10.775° | +75.427° | 20 | -4.310° | -10.775° | -75.427° |

Base station antenna gain ($G_{\text{BS}}(\theta_{l,s}^{\text{AoD}})$) Since the BS antennas are sectorized, its gain depends on the departure angle, as seen in Section 4.5.1 of [48].

Mobile antenna gain ($G_{\text{MS}}(\theta_{l,s}^{\text{AoA}})$) Each antenna element at the MS is assumed to have an omni-directional pattern with a gain of -1 dB.

Carrier wavelength (λ) The carrier wavelength is given in meters. For a carrier of 2 GHz, this value is equal to 0.15 m.

Distance from reference antenna at BS (d_m) The distance in meters from the m th antenna in the BS array from the reference antenna ($s = 1$). According to this definition, $d_1 = 0$.

Distance from reference antenna at MS (d_n) The distance in meters from the n th antenna in the MS array from the reference antenna ($u = 1$). According to this definition, $d_1 = 0$.

Subpath phase ($\Phi_{l,s}$) This is the phase of the s th subpath of the l th path. Subpath phases are independent identically distributed (i.i.d.) with a uniform distribution in the interval $[0^\circ, 360^\circ]$.

Magnitude of MS vector ($\|\mathbf{v}\|$) The MS velocity vector's magnitude can be fixed or drawn from a specified probability distribution.

Angle of MS vector (θ_v) The angle of the MS, with respect to the MS broadside (see Figure 2.3), is drawn from a uniform distribution in the interval $[0^\circ, 360^\circ]$.

The delay spread, σ_{DS} , for urban and suburban macrocells is drawn for a log-normal random variable as $\sigma_{DS} = 10^{\epsilon_{DS}\alpha_n + \mu_{DS}}$, where α_n is derived in Section 2.4.1, $\epsilon_{DS} = 0.288$ and $\mu_{DS} = -6.80$ for suburban macrocells and $\epsilon_{DS} = 0.18$ and $\mu_{DS} = -6.18$ for urban macrocells.

The azimuth spread, σ_{AS} , for urban and suburban macrocells is also drawn from a log-normal random variable as $\sigma_{AS} = 10^{\epsilon_{AS}\beta_n + \mu_{AS}}$, where β_n is derived in 2.4.1, $\epsilon_{AS} = 0.13$ and $\mu_{AS} = 0.69$ for suburban macrocells, $\epsilon_{AS} = 0.34$ and $\mu_{AS} = 0.810$ or $\epsilon_{AS} = 0.210$ and $\mu_{AS} = 1.18$ for urban macrocells with mean angle spread of 8° or 15° , respectively.

2.4.1 Correlation between channel parameters

In the SCM, the delay spread, the azimuth spread, and the log-normal shadow fading are assumed to be correlated. To take their correlation into account, $\sigma_{DS,n}$, $\sigma_{AS,n}$, and $\sigma_{SF,n}$ are calculated as follows (Section 5.6 in [48]).

First, a correlation matrix is defined as

$$A - B = \begin{bmatrix} 1 & \rho_{\alpha\beta} & \rho_{\gamma\alpha} \\ \rho_{\alpha\beta} & 1 & \rho_{\gamma\beta} \\ \rho_{\gamma\alpha} & \rho_{\gamma\beta} & 1 - \zeta \end{bmatrix}, \quad (2.18)$$

where the correlation between $\sigma_{DS,n}$ and $\sigma_{AS,n}$ is denoted by $\rho_{\alpha\beta}$, the correlation between $\sigma_{SF,n}$ and $\sigma_{DS,n}$ is denoted by $\rho_{\gamma\alpha}$, and the correlation between $\sigma_{SF,n}$ and $\sigma_{AS,n}$ is denoted by $\rho_{\gamma\beta}$. The shadowing fading correlation ζ takes into account inter-site correlations.

Following, correlated Gaussian random variables α_n , β_n , and γ_n are generated according to

$$\begin{bmatrix} \alpha_n \\ \beta_n \\ \gamma_n \end{bmatrix} = \begin{bmatrix} c_{11} & c_{12} & c_{13} \\ c_{21} & c_{22} & c_{23} \\ c_{31} & c_{32} & c_{33} \end{bmatrix} \begin{bmatrix} w_{n1} \\ w_{n2} \\ w_{n3} \end{bmatrix} + \begin{bmatrix} 0 & 0 & 0 \\ 0 & 0 & 0 \\ 0 & 0 & \sqrt{\zeta} \end{bmatrix} \begin{bmatrix} \zeta_1 \\ \zeta_2 \\ \zeta_3 \end{bmatrix}, \quad (2.19)$$

where w_{n1} , w_{n2} , w_{n3} , ζ_1 , ζ_2 , and ζ_3 are independent Gaussian random variables, and the matrix \mathbf{C} with elements c_{ij} is given by $(A - B)^{1/2}$.

2.4.2 Coherence time for the SCM

As seen in (2.11), the channel coefficients produced by the SCM are a function of time. This dependency allows one to track how the channel evolves as information is transmitted to a non-static receiver. In Figure 2.4, the channel gain for a SISO flat-fading channel, assuming a carrier frequency of 2 GHz and a MS moving at 30 km/h, 60 km/h, 90 km/h, and 120 km/h, with $\theta_v = 90^\circ$ (see Figure 2.3), is plotted.

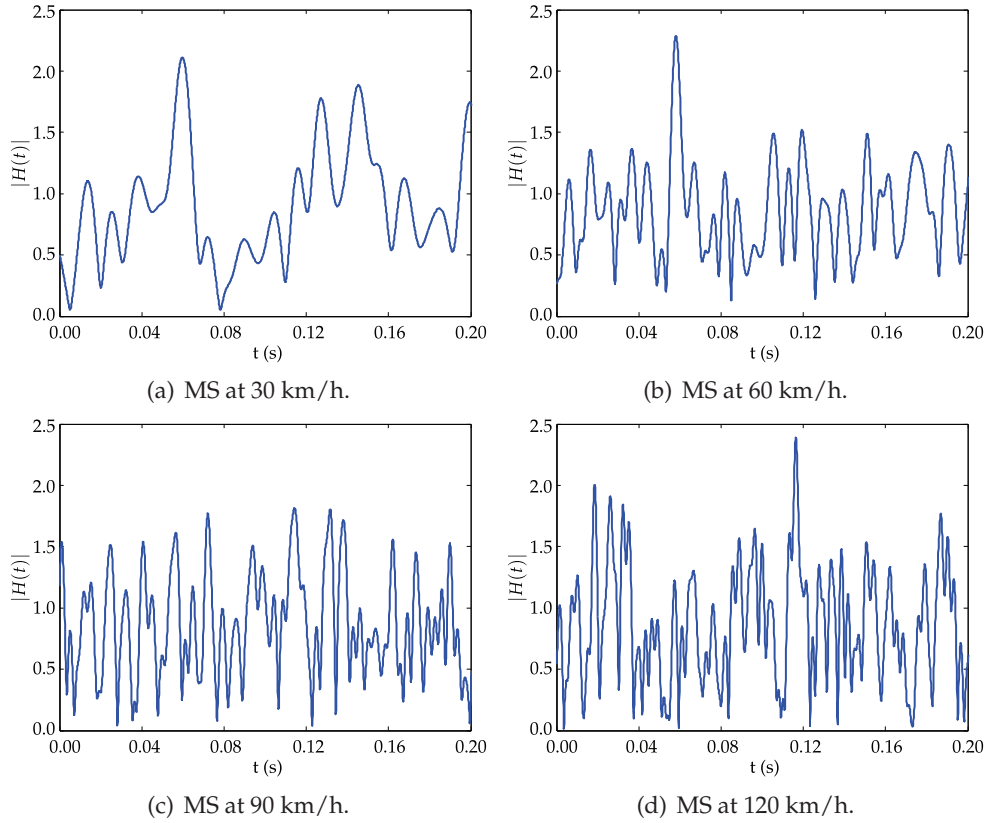


Figure 2.4: Fading over time for SISO flat-fading channels.

Defining the coherence time, T_c , of the channel as the time over which the time correlation is above 0.5, one can obtain the coherence times as $T_c = 4.6$ ms, $T_c = 2.2$ ms, $T_c = 1.7$ ms, and $T_c = 1.3$ ms, for 30 km/h, 60 km/h, 90 km/h, and 120 km/h, respectively. Hence, since sampling rates are normally on the order of 1 μ s, the SCM can be modelled as a block fading channel for blocks of up to one thousand symbols, even for the fastest MS. To obtain time-invariant channels, the last multiplicative term (2.11) is set to 1 by letting $t = 0$.

2.5 Baseband discrete-time channel model

To obtain a discrete-time channel model, delays should be given according to integer multiples of the sampling time T_S . As discussed earlier, most channel models, including the SCM, have proposed statistical distributions of tap delays that are not always integer multiples of T_S . The SCM, for instance, quantizes the path delays to the nearest 1/16th of the chip interval (defined in [48] as $1/(3.84 \times 10^6) = 2.6 \times 10^{-7}$ s), which may not be the same as T_S .

To obtain a discrete model for a given sampling rate T_S , a method based on the sampling theorem presented in [50] is used. The channel is assumed to be band-limited by an ideal rectangular filter with a bandwidth equal to that of the signal. With this limitation, for the SCM, an echo with gain $h^{m,n}[l]$ and delay τ_l can be represented, at the output of the rectangular filter, as

$$h^{m,n}[l]\text{sinc}(t - \tau_l), \quad (2.20)$$

which corresponds to a sinc function centred in its delay. Hence, the discrete multipath gains for integers of the sampling rate are given according to

$$h^{m,n'}[l] = \sum_{l=0}^{L-1} h^{m,n}[l]\text{sinc}(\tau_l - sT_S). \quad (2.21)$$

For a complex channel, this same approach is applied for both real and imaginary components.

2.6 Channel normalization

According to most multipath MIMO channel models, including the SCM, the system's performance is affected not only by MAI and ISI, but also by fading. In this work, the focus is on the performance of novel detection schemes for each instantaneous channel realization. Hence, to remove the contribution of fading to the system's performance, each realization of the MIMO channel \mathbf{H} needs to be normalized. Different approaches for normalization of MIMO channels have been adopted in the specialized literature. A comprehensive discussion on this subject can be found in [51]. In this paper the normalization approach is identical to the

one used in [52]. Each channel realization is multiplied by a factor α such that $\sum_0^{L-1} \alpha \|\mathbf{H}^l\|^2 = N_T$. This particular approach was chosen to ensure that the total received power is the same as the total transmitted power, or in other words, the channel's overall gain is equal to one.

Next chapter presents a technique, denoted jointly Gaussian approach (JGA), to overcome the effects of interference (both spatial and temporal) introduced by multipath SISO and MIMO channels. Following, an extension of this technique, dubbed extended JGA, is presented. The extended JGA, as well as its application for SC-FDMA transmissions is one of the major original contributions of this work.

3

The Jointly Gaussian Approach - JGA

In this chapter, an equalization method called the Jointly Gaussian Approach (JGA) is discussed. Following, an extension of this method, dubbed the Extended Jointly Gaussian Approach (Extended JGA, or EJGA), an original contribution of this work, is presented. Both methods are first presented for multipath SISO scenarios and later expanded to multipath MIMO scenarios. Next, both methods are adapted to work in the frequency domain for Single-Carrier Frequency-Division Multiple Access (SC-FDMA) transmissions, making them an attractive solution for equalization in the uplink scenario of LTE systems. The computational complexity of each method, as a function of the number of complex multiplications, is calculated and compared for both time and frequency-domain implementations. Low-complexity implementations for both methods are also discussed.

3.1 Classical JGA

In Chapter 2, it was shown that a received sequence \mathbf{y} for a transmitted sequence \mathbf{x} over a multipath channel is given according to

$$\mathbf{y} = \mathbf{H}\mathbf{x} + \mathbf{n}. \quad (3.1)$$

Since \mathbf{x} is a column vector, (3.1) can be rewritten as the sum of all symbols in \mathbf{x} multiplied by their corresponding columns in \mathbf{H} ,

$$\mathbf{y} = \sum_{l=0}^{K-1} \mathbf{h}[l]x[l] + \mathbf{n}, \quad (3.2)$$

where $\mathbf{h}[l]$ denotes the l th column of the channel matrix \mathbf{H} and K the size of the transmitted sequence \mathbf{x} .

For a given symbol $x[k]$ under detection, (3.2) can be rewritten as

$$\begin{aligned} \mathbf{y} &= \mathbf{h}[k]x[k] + \sum_{l=0, l \neq k}^{K-1} \mathbf{h}[l]x[l] + \mathbf{n} \\ &= \mathbf{h}[k]x[k] + \boldsymbol{\zeta}[k], \end{aligned} \quad (3.3)$$

where $\boldsymbol{\zeta}[k]$ denotes the sum of all interference terms plus noise.

The JGA, first proposed in [33] for CDMA detection, assumes $\boldsymbol{\zeta}[k]$ to be a vector of jointly Gaussian random variables. This assumption, which greatly simplifies the detection process, is justified by the CLT. The interference is created by the sum of i.i.d. random variables¹ (all transmitted symbols apart from the one under detection) multiplied by columns of \mathbf{H} , and the noise is assumed to be AWGN.

With this jointly Gaussian assumption, the *a posteriori* probability of having received \mathbf{y} , given that $x[k]$ was transmitted, has a multivariate normal distribution [53]

$$\begin{aligned} P(\mathbf{y}|x[k]) &= \frac{e^{-\frac{1}{2}(\mathbf{y}-\mathbf{h}[k]x[k]-\bar{\boldsymbol{\zeta}}[k])^\dagger \boldsymbol{\Sigma}[k]^{-1}(\mathbf{y}-\mathbf{h}[k]x[k]-\bar{\boldsymbol{\zeta}}[k])}}{\sqrt{(2\pi)^K \det(\boldsymbol{\Sigma}[k])}} \\ &= \frac{e^{-\frac{1}{2}(\boldsymbol{\zeta}[k]-\bar{\boldsymbol{\zeta}}[k])^\dagger \boldsymbol{\Sigma}[k]^{-1}(\boldsymbol{\zeta}[k]-\bar{\boldsymbol{\zeta}}[k])}}{\sqrt{(2\pi)^K \det(\boldsymbol{\Sigma}[k])}}, \end{aligned} \quad (3.4)$$

where the interference term $\boldsymbol{\zeta}[k]$ is calculated according to (3.3) as $\mathbf{y} - \mathbf{h}[k]x[k]$ and the mean value of the interference, $\bar{\boldsymbol{\zeta}}[k]$, is calculated as

$$\begin{aligned} \bar{\boldsymbol{\zeta}}[k] &= \bar{\mathbf{y}} - \mathbf{h}[k]\bar{x}[k] \\ &= \mathbf{H}\bar{\mathbf{x}} - \mathbf{h}[k]\bar{x}[k]. \end{aligned} \quad (3.5)$$

¹For the case of encoded transmissions, where the coded bits to be transmitted are correlated, an interleaver can be used prior to transmission to greatly reduce correlation effects.

The covariance matrix of the interference, $\zeta[k]$, denoted by $\Sigma[k]$ is given by

$$\Sigma[k] = \text{Cov}(\zeta[k], \zeta[k]) = \mathbf{H}\mathbf{V}[k]\mathbf{H}^\dagger + \sigma^2\mathbf{I}, \quad (3.6)$$

where the $K \times K$ matrix $\mathbf{V}[k]$ is the covariance matrix of the vector of transmitted symbols x . Since all transmitted symbols are assumed to be independent, this matrix is diagonal. Moreover, as $x[k]$ is assumed to be known in (3.4), its variance is null and, therefore, the diagonal element k of $\mathbf{V}[k]$, $v[k]$, is set to zero. The variance of the noise is denoted by σ^2 .

The mean value of the transmitted symbols, corresponding to the vector \bar{x} in (3.5), as well as its variance, corresponding to the diagonal elements of $\mathbf{V}[k]$ in (3.6), are calculated taking into account the *a priori* information about the vector of transmitted symbols, x . Denoting by $L[k]$ the LLR of $x[k]$, its mean value and its variance, assuming a BPSK modulation, are shown in Appendix A to be given by

$$\begin{aligned} \bar{x}[k] &= \tanh(L[k]/2), \\ v[k] &= 1 - |\tanh(L[k]/2)|^2. \end{aligned} \quad (3.7)$$

In Appendix A, it is also shown how to calculate $\bar{x}[k]$ and $v[k]$ for higher-order modulations, like QPSK and 16 QAM.

If no *a priori* information is available, \bar{x} is a null vector and all non-zero elements of $\mathbf{V}[k]$ are set to one, as it can be seen by setting $L[k]$ to zero in (3.7). In an iterative detecting system, the first iteration is normally carried out assuming that no *a priori* information is available.

The extrinsic LLRs for all transmitted symbols $x[k]$, assuming once more BPSK modulation, are easily calculated using (3.4) as

$$\begin{aligned} L[k] &= \log \left[\frac{P(\mathbf{y}|x[k] = +1)}{P(\mathbf{y}|x[k] = -1)} \right] \\ &= \log \left[\frac{e^{-\frac{1}{2}(\mathbf{y}-\mathbf{h}[k]-\bar{\zeta}[k])^\dagger \Sigma[k]^{-1}(\mathbf{y}-\mathbf{h}[k]-\bar{\zeta}[k])}}}{e^{-\frac{1}{2}(\mathbf{y}+\mathbf{h}[k]-\bar{\zeta}[k])^\dagger \Sigma[k]^{-1}(\mathbf{y}+\mathbf{h}[k]-\bar{\zeta}[k])}} \right], \end{aligned} \quad (3.8)$$

where the denominators of $P(\mathbf{y}|x[k] = +1)$ and $P(\mathbf{y}|x[k] = -1)$ are omitted since they are the same and, therefore, are cancelled out.

After simple algebraic manipulations, (3.8) can be rewritten as

$$\begin{aligned}
L[k] &= -\frac{1}{2} (\mathbf{y} - \mathbf{h}[k] - \bar{\boldsymbol{\xi}}[k])^\dagger \boldsymbol{\Sigma}[k]^{-1} (\mathbf{y} - \mathbf{h}[k] - \bar{\boldsymbol{\xi}}[k]) \\
&\quad + \frac{1}{2} (\mathbf{y} + \mathbf{h}[k] - \bar{\boldsymbol{\xi}}[k])^\dagger \boldsymbol{\Sigma}[k]^{-1} (\mathbf{y} + \mathbf{h}[k] - \bar{\boldsymbol{\xi}}[k]) \\
&= \mathbf{h}[k]^\dagger \boldsymbol{\Sigma}[k]^{-1} (\mathbf{y} - \bar{\boldsymbol{\xi}}[k]) + (\mathbf{y} - \bar{\boldsymbol{\xi}}[k])^\dagger \boldsymbol{\Sigma}[k]^{-1} \mathbf{h}[k] \\
&= 2\mathbf{h}[k]^\dagger \boldsymbol{\Sigma}[k]^{-1} (\mathbf{y} - \bar{\boldsymbol{\xi}}[k]) \\
&= 2\mathbf{h}[k]^\dagger \boldsymbol{\Sigma}[k]^{-1} (\mathbf{y} - \bar{\mathbf{y}} + \mathbf{h}[k]\bar{x}[k]) \\
&= 2\mathbf{h}[k]^\dagger \boldsymbol{\Sigma}[k]^{-1} (\mathbf{y} - \mathbf{H} \cdot \bar{\mathbf{x}} + \mathbf{h}[k]\bar{x}[k]).
\end{aligned} \tag{3.9}$$

It is interesting to note that this result was shown in [32] to be equivalent to the LLRs obtained in [54] applying the MMSE criterion for linear equalization. Hence, the performance of a detector based on the JGA is the same as of a linear detector applying the MMSE criterion. For channels greatly affected by multipath propagation, this performance can be quite far from that of a detector applying the optimal maximum-likelihood detection scheme [4]. Hence a more powerful equalization scheme can provide significant gains in performance.

For higher-order modulation schemes, each symbol carries information about a number of bits² as shown in Appendix A. If a constellation with 2^m symbols is used, where m denotes the modulation order, each symbol will define m bits and, therefore, m LLRs have to be calculated. The extrinsic LLR for the i th bit that defines a given symbol is calculated as the logarithm of the sum of the probabilities of all symbols for which this bit is equal to one, over the sum of the probabilities of all symbols for which it is equal to zero. Mathematically,

$$L[k] = \log \left[\frac{\sum_{x[k], b[i]=1} \left(P(\mathbf{y}|\mathbf{x}) \prod_{n=0, n \neq i}^m P(b[n]) \right)}{\sum_{x[k], b[i]=0} \left(P(\mathbf{y}|\mathbf{x}) \prod_{n=0, n \neq i}^m P(b[n]) \right)} \right], \tag{3.10}$$

where the sum in the numerator is performed over all symbols for which $b_i = 1$, and the sum in the denominator for all symbols for which $b_i = 0$. Each probability $P(\mathbf{y}|\mathbf{x})$ is multiplied by the product of the probabilities of all bits that determine the symbol $x[k]$, apart from the one which LLR is calculated. For instance, if a symbol $x[k]$ corresponds to $b_0 = 0$, $b_1 = 1$, $b_2 = 0$, and $b_3 = 1$, the LLR of b_2 is calculated

²For instance, in a 16 QAM modulation, each constellation symbol is determined by 4 bits, b_0 , b_1 , b_2 and b_4 .

multiplying $P(\mathbf{y}|\mathbf{x})$ by $P(b_0[k] = 0)P(b_1[k] = 1)P(b_3[k] = 1)$ for this term in the summation in (3.10).

In the next section, a new detection method is proposed to enhance the performance of detectors based on the JGA, without incurring in prohibitive computational complexities.

3.2 Extended JGA

In many realistic scenarios, most of the interference is due to only a small subset of dominant interference terms. Hence, using an optimal or sub-optimal method to remove the interference caused by these terms, while using a low-complexity scheme to remove the remaining interference, appears to be a good trade-off between performance versus complexity.

The idea of using a combination of methods with different complexities isn't new. For instance, it was used by Duel-Hallen and Heegard in [11]. They proposed a delayed decision-feedback sequence estimator, where a MAP scheme is used, in conjunction with a DFE, to estimate the signal transmitted over multipath SISO channels with several taps. Their method achieves great performance for multipath channels with most of its power concentrated on the first few taps.

In this thesis, an extension of the JGA is proposed. It achieves great performance for channels with most of its power concentrated in just a few taps, regardless of their position. It works by performing a marginalization over the interfering terms, while using a low-complexity method to deal with the remaining interference.

The extended JGA proposed here works as follows. First, a subset of interference terms, from now on denoted interferers, is removed from $\zeta[k]$, the interference pool. Without loss of generality, the method is presented here with the removal of only one interferer. For this particular case, (3.3) is rewritten as

$$\mathbf{y} = \mathbf{h}[k]x[k] + \mathbf{h}[m]x[m] + \zeta[k, m], \quad (3.11)$$

where the interference-plus-noise term $\zeta[k, m]$, associated with transmitted sym-

bols $x[k]$ and $x[m]$, can be calculated as

$$\boldsymbol{\zeta}[k, m] = \mathbf{y} - \mathbf{h}[k]x[k] - \mathbf{h}[m]x[m] = \sum_{l=0, l \neq k, m}^{K-1} \mathbf{h}[l]x[l] + \mathbf{n}. \quad (3.12)$$

As in the JGA, $\boldsymbol{\zeta}[k, m]$ is assumed to be a vector of jointly Gaussian random variables. Therefore,

$$P(\mathbf{y}|\mathbf{x}[k], \mathbf{x}[m]) = \frac{e^{-\frac{1}{2}(\boldsymbol{\zeta}[k, m] - \bar{\boldsymbol{\zeta}}[k, m])^\dagger \boldsymbol{\Sigma}[k, m]^{-1} (\boldsymbol{\zeta}[k, m] - \bar{\boldsymbol{\zeta}}[k, m])}}{\sqrt{(2\pi)^K \det(\boldsymbol{\Sigma}[k])}}, \quad (3.13)$$

with the covariance matrix of $\boldsymbol{\zeta}[k, m]$, $\boldsymbol{\Sigma}[k, m]$, being given by

$$\boldsymbol{\Sigma}[k, m] = \text{Cov}(\boldsymbol{\zeta}[k, m], \boldsymbol{\zeta}[k, m]) = \mathbf{H}\mathbf{V}[k, m]\mathbf{H}^\dagger + \sigma^2\mathbf{I}. \quad (3.14)$$

The matrix $\mathbf{V}[k, m]$ differs from $\mathbf{V}[k]$ for its m th diagonal element, $v[m]$, is set to zero together with $v[k]$, since $x[m]$ does not take part in the interference $\boldsymbol{\zeta}[k, m]$.

To calculate extrinsic LLRs corresponding to the transmitted symbol $x[k]$, as in (3.8), it is necessary to obtain an expression for $P(\mathbf{y}|\mathbf{x}[k])$, instead of $P(\mathbf{y}|\mathbf{x}[k], \mathbf{x}[m])$. Invoking the total probability theorem, it can be shown that

$$P(\mathbf{y}|\mathbf{x}[k]) = \sum_{x[m] \in \mathcal{C}} P(\mathbf{y}|\mathbf{x}[k], x[m]) P(x[m]), \quad (3.15)$$

where \mathcal{C} denotes the signal constellation used. If a BPSK modulation is employed, for instance, $\mathcal{C} = \{-1, +1\}$. Clearly, if more symbols are removed from the interference pool, $P(\mathbf{y}|\mathbf{x}[k])$ is calculated performing a marginalization over all symbols removed from the original interference pool $\boldsymbol{\zeta}[k]$.

For the scenario under discussion, where only one term is removed from $\boldsymbol{\zeta}[k]$, (3.15) is used to calculate extrinsic LLRs for $x[k]$ as

$$L[k] = \log \left[\frac{\sum_{x[m] \in \mathcal{C}} P(\mathbf{y}|\mathbf{x}[k] = +1, x[m]) P(x[m])}{\sum_{x[m] \in \mathcal{C}} P(\mathbf{y}|\mathbf{x}[k] = -1, x[m]) P(x[m])} \right], \quad (3.16)$$

where $P(\mathbf{y}|\mathbf{x}[k], x[m])$ can be calculated, for given values of $x[k]$ and $x[m]$, according to (3.13)³.

³Since the denominator in (3.13) is the same for all possible values of $x[k]$ and $x[m]$, it does not have to be taken in consideration in the calculation of extrinsic LLRs.

3.2.1 Choice of the set of interferers to be removed

A question that arises after the introduction of the idea of removing some terms from the interference pool is which set of symbols to remove. To answer this question it is first important to notice that the received signal is matched filtered. This is easily seen for the classical JGA due to the factor $\mathbf{h}[k]^\dagger$ multiplying the received signal in (3.9). It is also true for extended JGA, since both methods differ only by the removal of some interference terms.

For conciseness, the choice of a particular set of symbols to be removed from the interference pool will be analyzed here for a channel with only three taps. For this scenario, i.e., $\mathbf{h} = [h_0, h_1, h_2]$, the coefficients of the resultant filter, \mathbf{g} , after matched filtering, are given by

$$\begin{aligned} g_0 &= h_0 \cdot h_2^* \\ g_1 &= h_0 \cdot h_1^* + h_1 \cdot h_2^* \\ g_2 &= h_0 \cdot h_0^* + h_1 \cdot h_1^* + h_2 \cdot h_2^* \\ g_3 &= h_1 \cdot h_0^* + h_2 \cdot h_1^* \\ g_4 &= h_2 \cdot h_0^* \end{aligned} \quad (3.17)$$

Since there are five taps in \mathbf{g} , a given transmitted symbol, $x[k]$, appears not only in the expression of the received signal after matched filtering, $y[k]'$, but also in the expressions of $y[k+1]'$, $y[k+2]'$, $y[k+3]'$, and $y[k+4]'$, as follows

$$y[k+j]' = g_j x[k] + \sum_{i=0, i \neq j}^4 g_i x[k-i+j] + n[k+j] \quad (3.18)$$

with $j \in [0, 4]$.

If $x[k]$ is the symbol under detection, the SINR from each one of these five received symbols can be easily calculated as in (3.19). All symbols are assumed to have unitary energy and the power of the noise is denoted by N_0 .

$$SINR_{y[k+j]} = \frac{|g_j|^2}{\sum_{i=0, i \neq j}^4 |g_i|^2 + N_0} \quad (3.19)$$

If a given symbol is removed from the interference pool, for instance $x[k-1]$, the coefficients multiplying it in (3.18) are removed from the denominator of (3.19),

resulting in higher SINRs, and consequently in a better performance. Since $|g_0| = |g_4|$ and $|g_1| = |g_3|$, it can be easily shown that the removal of interference terms $x[k-1]$ or $x[k+1]$ will result in the same SINRs in (3.19), although in a different order. Hence, the same improvement in performance is obtained. This result holds for all pairs of symbols at the same distance from $x[k]$.

Removing the interference introduced by $x[k-1]$ will affect all SINRs from $SINR_{y[k]}$ through $SINR_{y[k+3]}$, while removing the interference introduced by $x[k-2]$ will only affect $SINR_{y[k]}$ through $SINR_{y[k+2]}$. Symbols further away from $x[k]$ will affect even less SINR terms in (3.19). Hence, for most channels, the best approach is to always start by removing the interference introduced by the symbol closest to $x[k]$. Nevertheless, for some atypical channels with most of its energy concentrated on the last taps, the choice of a symbol farther away, for instance, $x[k-2]$ instead of $x[k-1]$, might be the optimal decision.

Finally, a close look at (3.18) shows that, for this three taps scenario, the symbols farthest away from $x[k]$ that still interfere with its reception are $x[k-4]$ and $x[k+4]$. Hence, removing from the interference pool symbols prior to $x[k-4]$ or later than $x[k+4]$ won't affect (3.19) in any way and, therefore, won't provide any benefits to the detection process. It can be shown that for a channel with L paths, the extended JGA will only have an improved performance, compared to JGA, when symbols at most $2L - 2$ time instants away from the detected symbol are removed from the interference pool.

3.3 JGA for multipath MIMO channels

As shown in Chapter 2, the channel equation (3.1) can also be applied to multipath MIMO scenarios. For an $N_T \times N_R$ MIMO scenario with L paths, the channel matrix \mathbf{H} is composed by L $N_T \times N_R$ submatrices and the transmitted vector x is created by stacking up symbols from all transmitting antennas for all time instants, as shown in (2.4).

Denoting by $x_m[k]$ the symbol transmitted by the m th antenna at the k th time instant, and by $h_m[k]$ its corresponding column in the channel matrix \mathbf{H} , (3.2) can be

rewritten for the MIMO scenario, for the n th receiving antenna as

$$\mathbf{y} = \sum_{m=0}^{N_T-1} \sum_{l=0}^{K-1} \mathbf{h}_m[l] x_m[l] + \mathbf{n}. \quad (3.20)$$

If a given symbol $x_i[k]$, i.e. the k th symbol transmitted by the i th antenna, is under detection, (3.20) can be rewritten as

$$\mathbf{y} = \mathbf{h}_i[k] x_i[k] + \boldsymbol{\zeta}_i[k], \quad (3.21)$$

where the interference plus noise term $\boldsymbol{\zeta}_i[k]$ associated with the transmitted symbol $x_i[k]$ can be calculated as

$$\boldsymbol{\zeta}_i[k] = \mathbf{y} - \mathbf{h}_i[k] x_i[k] = \sum_{\substack{m=0 \\ n \neq i}}^{N_T-1} \mathbf{h}_m[k] x_m[k] + \sum_{\substack{m=0 \\ l \neq k}}^{N_T-1} \sum_{l=0}^{K-1} \mathbf{h}_m[l] x_m[l] + \mathbf{n}. \quad (3.22)$$

Each one of the three terms in the above expression corresponds to a different source of interference. The first sum corresponds to the interference introduced by other antennas, i.e., the MAI. The second sum takes into account the interference introduced by symbols transmitted by all antennas for all time instants different than k , i.e., the ISI. Finally, \mathbf{n} denotes the additive white Gaussian noise.

Applying the jointly Gaussian assumption on $\boldsymbol{\zeta}_i[k]$, the *a posteriori* probability of having received \mathbf{y} , given that $x_i[k]$ was transmitted, is given by

$$P(\mathbf{y}|x_i[k]) = \frac{e^{-\frac{1}{2}(\boldsymbol{\zeta}_i[k] - \bar{\boldsymbol{\zeta}}_i[k])^\dagger \boldsymbol{\Sigma}_i[k]^{-1} (\boldsymbol{\zeta}_i[k] - \bar{\boldsymbol{\zeta}}_i[k])}}{\sqrt{(2\pi)^{N_R(K)} \det(\boldsymbol{\Sigma}_i[k])}}, \quad (3.23)$$

with the interference term $\boldsymbol{\zeta}_i[k]$ calculated according to (3.21) as $\mathbf{y} - \mathbf{h}_i[k] x_i[k]$. The covariance matrix of $\boldsymbol{\zeta}_i[k]$, denoted by $\boldsymbol{\Sigma}_i[k]$ is given by

$$\boldsymbol{\Sigma}_i[k] = \text{Cov}(\boldsymbol{\zeta}_i[k], \boldsymbol{\zeta}_i[k]) = \mathbf{H}\mathbf{V}_i[k]\mathbf{H}^\dagger + \sigma^2\mathbf{I}. \quad (3.24)$$

Where the $N_T K \times N_T K$ matrix $\mathbf{V}_i[k]$ is a diagonal matrix with the variance of all transmitted symbols as its diagonal elements, with the exception of $x_i[k]$ which is assumed to be known, and therefore is set to zero. The variance of the noise is denoted by σ^2 .

Clearly, as in the SISO scenario, the extrinsic LLR for $x_i[k]$ can be calculated, taking into account (3.23), as

$$\begin{aligned} L_i[k] &= \log \left[\frac{P(\mathbf{y} | x_i[k] = +1)}{P(\mathbf{y} | x_i[k] = -1)} \right] \\ &= \log \left[\frac{e^{-\frac{1}{2}(\mathbf{y} - \mathbf{h}_i[k] - \bar{\boldsymbol{\zeta}}_i[k])^\dagger \boldsymbol{\Sigma}_i[k]^{-1} (\mathbf{y} - \mathbf{h}_i[k] - \bar{\boldsymbol{\zeta}}_i[k])}}{e^{-\frac{1}{2}(\mathbf{y} + \mathbf{h}_i[k] - \bar{\boldsymbol{\zeta}}_i[k])^\dagger \boldsymbol{\Sigma}_i[k]^{-1} (\mathbf{y} + \mathbf{h}_i[k] - \bar{\boldsymbol{\zeta}}_i[k])}} \right]. \end{aligned} \quad (3.25)$$

As it will be shown in later chapters, the performance of detectors based on the JGA can be greatly enhanced by removing some interference terms from $\bar{\boldsymbol{\zeta}}_i[k]$.

3.4 Extended JGA for multipath MIMO channels

In a multipath MIMO channel, as discussed in Chapter 2, the total interference is due to symbols transmitted at the same time but from different antennas, MAI, and from symbols transmitted at previous time instants arriving from different paths, ISI. These two different interference sources are represented as the first two terms in (3.22).

Transmitted symbols belonging to any one of these two terms can be removed from the interference term $\bar{\boldsymbol{\zeta}}_i[k]$ in (3.21). For most channels analyzed in this work, the MAI has been found to be the most important source of interference. Therefore, for the remainder of this section, the extended JGA has its performance enhanced, as compared to a regular JGA, by removing from $\bar{\boldsymbol{\zeta}}_i[k]$ the MAI. However, it is straightforward to generalize the results here for any set of interferers regardless of their nature (MAI or ISI) or even mixed sets of interferers, i.e., removal of some symbols that causes MAI and some symbols causing ISI from $\bar{\boldsymbol{\zeta}}_i[k]$.

With the removal of the MAI from $\bar{\boldsymbol{\zeta}}_i[k]$, (3.21) can be rewritten as

$$\mathbf{y} = \mathbf{h}_i[k]x_i[k] + \sum_{\substack{n=0 \\ n \neq i}}^{N_T-1} \mathbf{h}_n[k]x_n[k] + \boldsymbol{\zeta}[k], \quad (3.26)$$

where $\boldsymbol{\zeta}[k]$ is now written without the subindex i since, after removing the interference from symbols transmitted by all antennas at time instant k , the residual interference will be the same for all symbols $x_m[k]$, where $m = 0, \dots, N_T - 1$.

Once more applying the jointly Gaussian assumption, the probability of receiving \mathbf{y} given all symbols transmitted at time instant k is

$$P(\mathbf{y}|\mathbf{x}[k]) = \frac{e^{-\frac{1}{2}(\boldsymbol{\zeta}[k] - \bar{\boldsymbol{\zeta}}[k])^\dagger \boldsymbol{\Sigma}[k]^{-1} (\boldsymbol{\zeta}[k] - \bar{\boldsymbol{\zeta}}[k])}}{\sqrt{(2\pi)^{N_R(K+L-1)} \det(\boldsymbol{\Sigma}[k])}}, \quad (3.27)$$

where $\mathbf{x}[k]$ denotes the vector of all N_T symbols transmitted at k , $\boldsymbol{\zeta}[k]$ is calculated as $\mathbf{y} - \sum_{m=0}^{N_T-1} \mathbf{h}_m[k] x_m[k]$, and $\bar{\boldsymbol{\zeta}}[k]$ is calculated as

$$\bar{\boldsymbol{\zeta}}[k] = \sum_{m=0}^{N_T-1} \sum_{l=0, l \neq k}^{K-1} \mathbf{h}_m[l] \bar{x}_m[l], \quad (3.28)$$

where the mean value of the transmitted symbols, $\bar{x}_m[l]$, are calculated according to (3.7), for a BPSK modulation, according to (A.10) for QPSK or according to (A.13) for 16 QAM (see Appendix A).

The covariance matrix of $\boldsymbol{\zeta}[k]$ in (3.27) is given by

$$\boldsymbol{\Sigma}[k] = \text{Cov}(\boldsymbol{\zeta}[k], \boldsymbol{\zeta}[k]) = \mathbf{H}\mathbf{V}[k]\mathbf{H}^\dagger + \sigma_w^2 \mathbf{I}, \quad (3.29)$$

where $\mathbf{V}[k]$ is a $N_T K \times N_T K$ diagonal matrix containing the variance of all transmitted symbols. Since the symbols in the transmitted vector $\mathbf{x}[k]$ are assumed to be known, their variance is set to zero in $\mathbf{V}[k]$.

The extrinsic LLRs for transmitted symbols over MIMO multipath channels can be calculated, according to the extended JGA, using (3.27) with the marginalization over all symbols removed from the interference pool as in (3.15). For a 2×2 MIMO communications system applying a BPSK modulation, the extrinsic LLR for transmitted symbols $x_0[k]$ and $x_1[k]$ are given by

$$\begin{aligned} L_0[k] &= \log \left[\frac{\sum_{x_1[k] \in \mathcal{C}} P(\mathbf{y}|x_0[k] = +1, x_1[k]) P(x_1[k])}{\sum_{x_1[k] \in \mathcal{C}} P(\mathbf{y}|x_0[k] = -1, x_1[k]) P(x_1[k])} \right] \\ &= \log \left[\frac{\sum_{x_1[k] \in \mathcal{C}} e^{-\frac{1}{2}(\mathbf{y} - \mathbf{h}_0[k] - \mathbf{h}_1[k]x_1[k] - \bar{\boldsymbol{\zeta}}[k])^\dagger \boldsymbol{\Sigma}[k]^{-1} (\mathbf{y} - \mathbf{h}_0[k] - \mathbf{h}_1[k]x_1[k] - \bar{\boldsymbol{\zeta}}[k])} P(x_1[k])}{\sum_{x_1[k] \in \mathcal{C}} e^{-\frac{1}{2}(\mathbf{y} + \mathbf{h}_0[k] - \mathbf{h}_1[k]x_1[k] - \bar{\boldsymbol{\zeta}}[k])^\dagger \boldsymbol{\Sigma}[k]^{-1} (\mathbf{y} + \mathbf{h}_0[k] - \mathbf{h}_1[k]x_1[k] - \bar{\boldsymbol{\zeta}}[k])} P(x_1[k])} \right], \end{aligned} \quad (3.30)$$

and

$$\begin{aligned}
L_1[k] &= \log \left[\frac{\sum_{x_0[k] \in \mathcal{C}} P(\mathbf{y} | x_1[k] = +1, x_0[k]) P(x_0[k])}{\sum_{x_0[k] \in \mathcal{C}} P(\mathbf{y} | x_1[k] = -1, x_0[k]) P(x_0[k])} \right] \\
&= \log \left[\frac{\sum_{x_0[k] \in \mathcal{C}} e^{-\frac{1}{2}(\mathbf{y} - \mathbf{h}_1[k] - \mathbf{h}_0[k]x_0[k] - \xi[k])^\dagger \boldsymbol{\Sigma}[k]^{-1}(\mathbf{y} - \mathbf{h}_1[k] - \mathbf{h}_0[k]x_0[k] - \xi[k])} P(x_0[k])}{\sum_{x_0[k] \in \mathcal{C}} e^{-\frac{1}{2}(\mathbf{y} + \mathbf{h}_1[k] - \mathbf{h}_0[k]x_0[k] - \xi[k])^\dagger \boldsymbol{\Sigma}[k]^{-1}(\mathbf{y} + \mathbf{h}_1[k] - \mathbf{h}_0[k]x_0[k] - \xi[k])} P(x_0[k])} \right], \tag{3.31}
\end{aligned}$$

where \mathcal{C} denotes the BPSK constellation $\{-1, +1\}$.

The jointly Gaussian approach for SISO and MIMO multipath channels has been presented here, together with their proposed extensions, without taking their computational complexity into account. In fact, as these methods were presented, they require a covariance matrix $\boldsymbol{\Sigma}[k]$ of size $K \times K$, for SISO scenarios, and $\boldsymbol{\Sigma}_i[k]$ of size $N_R K \times N_R K$, for MIMO scenarios, to be inverted for each detected symbol. Since K is normally large, this operation is computationally intensive. In the next section, methods to reduce the computational burden of signal detection using the JGA and the extended JGA approach are introduced.

3.5 Low-complexity implementation methods

In this section, some methods to reduce the computational effort involved in the process of signal equalization using the JGA are presented. First, the block-band diagonal structure of \mathbf{H} is used to justify the use of a sliding window over the channel matrix \mathbf{H} , instead of the whole matrix. Following, the available *a priori* information is averaged to ensure that only one matrix inversion is necessary for the whole block of data under detection.

All methods are presented here for the JGA applied to multipath MIMO scenarios. Nevertheless, their generalization for the extended JGA is straightforward. The SISO scenario can be seen as a special case of a MIMO scenario with $N_T = N_R = 1$.

3.5.1 Sliding window

The channel matrix \mathbf{H} , as aforementioned, is a block-band diagonal matrix. Hence, just a few terms close to its main diagonal are nonzero. As a consequence, only

a few terms close to the main diagonal of $\Sigma_i[k]$, calculated according to (3.24), are different than zero. Thus, a sliding window of size $N \times N$, with $N = N_1 + N_2 + 1 \ll N_T K$ (N_1 and N_2 denote, respectively, the number of anticausal and causal terms taken into account by the sliding window.), around the symbol under detection, can be applied to $\Sigma_i[k]$ in the calculation of the LLR of $x_i[k]$ with minimal loss in performance. The result is that a $N \times N$ matrix, denoted by $\Sigma_i[k]'$, can be used instead of the $N_R K \times N_R K$ matrix $\Sigma_i[k]$.

The probability of receiving a given vector $\mathbf{y}' = \{\mathbf{y}[k - N_2 + 1], \dots, \mathbf{y}[k + N_1]\}$, given $x[k]$, with this approximation, is

$$P(\mathbf{y}' | x_i[k]) = \frac{e^{-\frac{1}{2}(\xi_i[k]' - \bar{\xi}_i[k]')^\dagger \Sigma_i[k]'^{-1} (\xi_i[k]' - \bar{\xi}_i[k]')}}{\sqrt{(2\pi)^N \det(\Sigma_i[k]')}}}, \quad (3.32)$$

where the interference term $\xi_i[k]'$, and its average $\bar{\xi}_i[k]'$ are calculated taking into account $\{\mathbf{y}[k - N_2 + 1], \dots, \mathbf{y}[k + N_1]\}$ and $\{\bar{\mathbf{x}}[k - N_2 + 1], \dots, \bar{\mathbf{x}}[k + N_1]\}$, instead of the entire vectors \mathbf{y} and $\bar{\mathbf{x}}$, for each value of k . The sliding window approximation makes it possible to calculate LLRs using (3.32), instead of the much more computationally intensive expression in (3.23).

3.5.2 Averaging the *a priori* information

Although dramatically reducing the computational complexity of the detection process, the use of a sliding window still requires an $N \times N$ matrix to be inverted for each detected symbol.

To avoid the inversion of a large number of matrices, a low complexity approach was proposed in [54]. The basic idea is to substitute $\mathbf{V}_i[k]$, a diagonal matrix containing the variances of the transmitted symbols in (3.24) by $\bar{v}\mathbf{I}_i[k]$, where \bar{v} corresponds to the average variance of the transmitted symbols. Hence, without the zero term in $\mathbf{I}_i[k]$, corresponding to the symbol under detection, $x[k]$, a sliding window over the matrix $\Sigma_i[k]$ is the same for all transmitted symbols.

To take this zero term in $\mathbf{I}_i[k]$ into account, it can be shown that

$$\Sigma_i[k] = \bar{v}\mathbf{H}\mathbf{I}_i[k]\mathbf{H}^\dagger + \sigma^2\mathbf{I} = \bar{v}\mathbf{H}\mathbf{H}^\dagger + \sigma^2\mathbf{I} - \bar{v}\mathbf{h}_i[k]\mathbf{h}_i[k]^\dagger. \quad (3.33)$$

Denoting $\bar{\nu}\mathbf{H}\mathbf{H}^\dagger + \sigma^2\mathbf{I}$ by $\mathbf{\Sigma}$, and applying the Sherman-Morrison formula [55],

$$\mathbf{\Sigma}_i[k]^{-1} = \left(\mathbf{\Sigma} - \bar{\nu}\mathbf{h}_i[k]\mathbf{h}_i[k]^\dagger \right)^{-1} = \mathbf{\Sigma}^{-1} + \bar{\nu} \frac{\mathbf{\Sigma}^{-1}\mathbf{h}_i[k]\mathbf{h}_i[k]^\dagger\mathbf{\Sigma}^{-1}}{1 - \bar{\nu}\mathbf{h}_i[k]^\dagger\mathbf{\Sigma}^{-1}\mathbf{h}_i[k]}, \quad (3.34)$$

therefore, only one matrix inversion, $\mathbf{\Sigma}^{-1}$, is required to calculate LLRs for all transmitted symbols. As shown in [54], this method greatly reduces the computational complexity while still resulting in good performances. For the extended JGA, the Sherman-Morrison formula has to be applied recursively, taking out the zero terms in $\mathbf{I}[k]$ corresponding to each term removed from the interference pool one by one since

$$\mathbf{\Sigma}[k] = \bar{\nu}\mathbf{H}\mathbf{I}[k]\mathbf{H}^\dagger + \sigma^2\mathbf{I} = \bar{\nu}\mathbf{H}\mathbf{H}^\dagger + \sigma^2\mathbf{I} - \bar{\nu} \sum_{m=0}^{N_T} \mathbf{h}_m[k]\mathbf{h}_m[k]^\dagger. \quad (3.35)$$

For instance, in a 2×2 MIMO system the covariance matrix $\mathbf{\Sigma}[k]^{-1}$ can be calculated as,

$$\mathbf{\Sigma}[k]^{-1} = \mathbf{\Sigma}_0[k]^{-1} + \bar{\nu} \frac{\mathbf{\Sigma}_0[k]^{-1}\mathbf{h}_1[k]\mathbf{h}_1[k]^\dagger\mathbf{\Sigma}_0[k]^{-1}}{1 - \bar{\nu}\mathbf{h}_1[k]^\dagger\mathbf{\Sigma}_0[k]^{-1}\mathbf{h}_1[k]}, \quad (3.36)$$

where

$$\mathbf{\Sigma}_0[k]^{-1} = \mathbf{\Sigma}^{-1} + \bar{\nu} \frac{\mathbf{\Sigma}^{-1}\mathbf{h}_0[k]\mathbf{h}_0[k]^\dagger\mathbf{\Sigma}^{-1}}{1 - \bar{\nu}\mathbf{h}_0[k]^\dagger\mathbf{\Sigma}^{-1}\mathbf{h}_0[k]}. \quad (3.37)$$

Although both sliding-window and averaging the *a priori* information methods were presented for the MIMO scenario, their application to SISO scenarios can be done in exactly the same fashion.

3.6 JGA for SC-FDMA

In this section, it is presented how to perform equalization in the frequency domain using the JGA. Frequency-domain equalization can be used in systems like the SC-FDMA, proposed for the uplink scenario for the LTE standard, to treat the interference introduced by multipath and/or multiple antennas with only a fraction of the computational complexity required by its time-domain counterpart.

To start analyzing frequency-domain equalization using the JGA, a DFT matrix of

size K is defined

$$\mathbf{F} = \frac{1}{\sqrt{K}} \begin{bmatrix} 1 & 1 & 1 & \dots & 1 \\ 1 & \omega & \omega^2 & \dots & \omega^{K-1} \\ 1 & \omega^2 & \omega^4 & \dots & \omega^{2(K-1)} \\ \vdots & \vdots & \vdots & \ddots & \vdots \\ 1 & \omega^{K-1} & \omega^{2(K-1)} & \dots & \omega^{(K-1)(K-1)} \end{bmatrix} \quad (3.38)$$

where $\omega = e^{-\frac{2\pi i}{K}}$ is a primitive K th root of unity, and $i = \sqrt{-1}$.

With the above definition, the DFT of any sequence s can be obtained by multiplying it by this matrix, i.e., $\mathbf{S} = \mathbf{F}s$. The original sequence can be recovered by multiplying it by the inverse of \mathbf{F} , i.e., $s = \mathbf{F}^{-1}\mathbf{S} = \mathbf{F}^{-1}\mathbf{F}s = s$.

In an LTE system, as mentioned above, transmission on the uplink scenario is performed using an SC-FDMA model. A simplified SC-FDMA schematic diagram is presented in Figure 3.1. The transmitted sequence x is transformed from time domain to the frequency domain via a DFT transform of size N , resulting in \mathbf{X} . Following, a subcarrier mapper adds zeros to this signal, increasing its length from N to M . This subcarrier mapping, which can be represented by a matrix \mathbf{D} , results in \mathbf{X}' . The sequence \mathbf{X}' is transformed back to the time domain by an IDFT of size M , resulting in a sequence x' to be transmitted. After transmission over a frequency selective noisy channel, the signal at the receiver is

$$\mathbf{y}' = \mathbf{H}\mathbf{x}' + \mathbf{n} = \mathbf{H}\mathbf{F}_M^{-1}\mathbf{X}' + \mathbf{n} = \mathbf{H}\mathbf{F}_M^{-1}\mathbf{D}\mathbf{F}_N\mathbf{x} + \mathbf{n}, \quad (3.39)$$

where $\mathbf{x}' = \mathbf{F}_M^{-1}\mathbf{D}\mathbf{F}_N\mathbf{x}$ and $\mathbf{X}' = \mathbf{D}\mathbf{F}_N\mathbf{x}$.

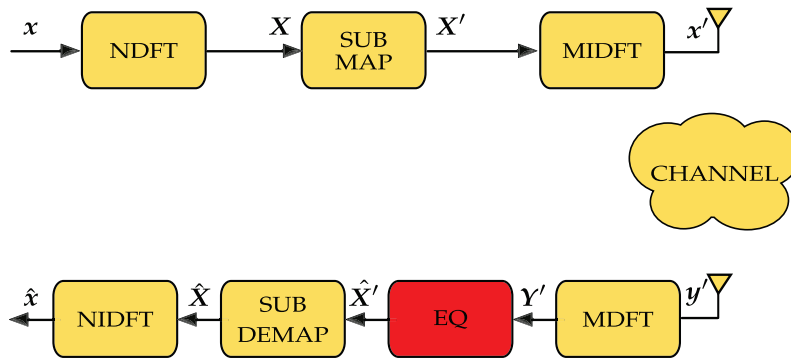


Figure 3.1: Simplified schematics diagram for SC-FDMA.

Applying a DFT transform of size M to the received signal results in

$$\begin{aligned} \mathbf{Y}' &= \mathbf{F}_M \mathbf{y}' = \mathbf{F}_M \mathbf{H} \mathbf{F}_M^{-1} \mathbf{X}' + \mathbf{F}_M \mathbf{n} \\ &= \tilde{\mathbf{H}} \mathbf{X}' + \mathbf{n}', \end{aligned} \quad (3.40)$$

where $\mathbf{n}' = \mathbf{F}_M \mathbf{n}$ is statistically identical to \mathbf{n} and $\tilde{\mathbf{H}} = \mathbf{F}_M^{-1} \mathbf{H} \mathbf{F}_M$. Assuming that \mathbf{H} is a circulant (or Toeplitz) matrix⁴, the DFT-eigenstructure of circulant matrices guarantees that $\tilde{\mathbf{H}}$ is a diagonal matrix [6]

$$\tilde{\mathbf{H}} = \begin{bmatrix} \tilde{h}_{f_0} & 0 & 0 & \cdots & 0 \\ 0 & \tilde{h}_{f_1} & 0 & \cdots & 0 \\ 0 & 0 & \ddots & \ddots & \vdots \\ \vdots & \vdots & \ddots & \ddots & \vdots \\ 0 & 0 & 0 & \cdots & \tilde{h}_{f_{M-1}} \end{bmatrix}, \quad (3.41)$$

where each term \tilde{h}_{f_i} represents the frequency response of the channel for a particular frequency f_i .

Classically, interference is taken care of by an equalizer that passes \mathbf{Y}' through a linear filter whose coefficients are calculated according to the MMSE criterion, resulting in a filtered sequence $\hat{\mathbf{X}}'$. Since the channel matrix is diagonal, the covariance matrix, $\tilde{\Sigma} = \tilde{\mathbf{H}} \tilde{\mathbf{H}}^\dagger + \sigma^2 \mathbf{I}$, is also diagonal. Hence, it can be inverted by inverting each one of its diagonal components, making the equalization process computationally efficient. However, this simple method cannot take into account *a priori* information about the transmitted sequence \mathbf{x} , hence it isn't able to take advantage of iterative equalization techniques.

The JGA can be used, instead of a linear MMSE filter, to counteract the effects of interference taking into account *a priori* information. To begin presenting the JGA for SC-FDMA signal transmission, it is necessary to obtain the covariance matrix

⁴In real systems, a cyclic prefix has to be added to the signal in order to make the channel to appear to be circulant. Here, for simplicity, the channel is already assumed to be in the circulant form.

of the received signal \mathbf{Y}' , which can be calculated as

$$\begin{aligned}
\tilde{\Sigma} &= \mathbb{E} \left[\mathbf{Y}' \mathbf{Y}'^\dagger \right] = \mathbb{E} \left[(\tilde{\mathbf{H}} \mathbf{X}' + \mathbf{n}') (\tilde{\mathbf{H}} \mathbf{X}' + \mathbf{n}')^\dagger \right] \\
&= \mathbb{E} \left[\tilde{\mathbf{H}} \mathbf{X}' \mathbf{X}'^\dagger \tilde{\mathbf{H}}^\dagger \right] + \mathbb{E} \left[\mathbf{n}' \mathbf{n}'^\dagger \right] \\
&= \tilde{\mathbf{H}} \mathbb{E} \left[\mathbf{X}' \mathbf{X}'^\dagger \right] \tilde{\mathbf{H}}^\dagger + \sigma^2 \mathbf{I} \\
&= \tilde{\mathbf{H}} \mathbb{E} \left[\mathbf{D} \mathbf{F}_N \mathbf{x} \mathbf{x}^\dagger \mathbf{F}_N^{-1} \mathbf{D}^{-1} \right] \tilde{\mathbf{H}}^\dagger + \sigma^2 \mathbf{I} \\
&= \tilde{\mathbf{H}} \mathbf{D} \mathbf{F}_N \mathbb{E} \left[\mathbf{x} \mathbf{x}^\dagger \right] \mathbf{F}_N^{-1} \mathbf{D}^{-1} \tilde{\mathbf{H}}^\dagger + \sigma^2 \mathbf{I}.
\end{aligned} \tag{3.42}$$

Assuming the same averaging *a priori* information technique, discussed in Section 3.5.2, $\mathbb{E} [\mathbf{x} \mathbf{x}^\dagger] \approx \bar{\nu} \mathbf{I}$. Hence, with this approximation, the covariance matrix of \mathbf{Y}' can also be approximated by a diagonal matrix, as seen below

$$\tilde{\Sigma} \approx \bar{\nu} \tilde{\mathbf{H}} \mathbf{D} \mathbf{F}_N \mathbf{I} \mathbf{F}_N^{-1} \mathbf{D}^{-1} \tilde{\mathbf{H}}^\dagger + \sigma^2 \mathbf{I} = \bar{\nu} \tilde{\mathbf{H}} \tilde{\mathbf{H}}^\dagger + \sigma^2 \mathbf{I}. \tag{3.43}$$

To calculate the covariance matrix of the interference associated with a transmitted symbol $x[k]$ under detection, as required by (3.8), the variance of this symbol should be set to zero. Hence (3.43) is rewritten as

$$\tilde{\Sigma}[k] = \bar{\nu} \tilde{\mathbf{H}} \mathbf{D} \mathbf{F}_N \mathbf{I}[k] \mathbf{F}_N^{-1} \mathbf{D}^{-1} \tilde{\mathbf{H}}^\dagger + \sigma^2 \mathbf{I}, \tag{3.44}$$

where $\mathbf{I}[k]$ is an identity matrix with a zero in the k th diagonal term.

Due to the zero term in $\mathbf{I}[k]$, $\tilde{\Sigma}[k]$ is no longer a diagonal matrix. However, the Sherman-Morrison formula can be applied as in Section 3.5.2. To start, denoting by $\tilde{\mathbf{h}}_{DFN}[k]$, the k th column of matrix $\tilde{\mathbf{H}}_{DFN} = \tilde{\mathbf{H}} \mathbf{D} \mathbf{F}_N$, one can rewrite (3.44) as

$$\begin{aligned}
\tilde{\Sigma}[k] &= \bar{\nu} \tilde{\mathbf{H}} \mathbf{D} \mathbf{F}_N \mathbf{F}_N^{-1} \mathbf{D}^{-1} \tilde{\mathbf{H}}^\dagger + \sigma^2 \mathbf{I} - \bar{\nu} \tilde{\mathbf{h}}_{DFN}[k] \tilde{\mathbf{h}}_{DFN}[k]^\dagger \\
&= \bar{\nu} \tilde{\mathbf{H}} \tilde{\mathbf{H}}^\dagger + \sigma^2 \mathbf{I} - \bar{\nu} \tilde{\mathbf{h}}_{DFN}[k] \tilde{\mathbf{h}}_{DFN}[k]^\dagger,
\end{aligned} \tag{3.45}$$

where the matrix $\tilde{\Sigma} = \bar{\nu} \tilde{\mathbf{H}} \tilde{\mathbf{H}}^\dagger + \sigma^2 \mathbf{I}$, as discussed before, is diagonal and can be easily inverted. The inverse of $\tilde{\Sigma}[k]$ is thus obtained as

$$\tilde{\Sigma}[k]^{-1} = \tilde{\Sigma}^{-1} + \bar{\nu} \frac{\Sigma^{-1} \tilde{\mathbf{h}}_{DFN}[k] \tilde{\mathbf{h}}_{DFN}[k]^\dagger \tilde{\Sigma}^{-1}}{1 - \bar{\nu} \tilde{\mathbf{h}}_{DFN}[k]^\dagger \tilde{\Sigma}^{-1} \tilde{\mathbf{h}}_{DFN}[k]}. \tag{3.46}$$

To take advantage of the diagonal nature of $\tilde{\mathbf{H}}$ and $\tilde{\Sigma}$, the extrinsic LLR for each detected symbol is calculated together with the inverse subcarrier mapping and

the inverse DFT transform of size N .

Before calculating LLRs in the frequency domain, it is important to notice that in the time domain, i.e. after \mathbf{Y}' passes through an inverse subcarrier mapper and an inverse DFT of size N , the received signal is given by

$$\begin{aligned}
\mathbf{y} &= \mathbf{F}_N^{-1} \mathbf{D}^{-1} \mathbf{Y}' \\
&= \mathbf{F}_N^{-1} \mathbf{D}^{-1} \mathbf{F}_M \mathbf{H} \mathbf{F}_M^{-1} \mathbf{X}' + \mathbf{F}_N^{-1} \mathbf{D}^{-1} \mathbf{n}' \\
&= \mathbf{F}_1^{-1} \mathbf{D}^{-1} \mathbf{F}_M \mathbf{H} \mathbf{F}_M^{-1} \mathbf{D} \mathbf{F}_N \mathbf{x} + \mathbf{F}_N^{-1} \mathbf{D}^{-1} \mathbf{F}_M \mathbf{n} \\
&= \mathbf{F}_N^{-1} \mathbf{D}^{-1} \tilde{\mathbf{H}} \mathbf{D} \mathbf{F}_N \mathbf{x} + \mathbf{n}'' \\
&= \tilde{\mathbf{H}}' \mathbf{x} + \mathbf{n}'' .
\end{aligned} \tag{3.47}$$

From (3.47), it can be seen that the system behaves as if a sequence \mathbf{x} is transmitted over a channel defined by $\tilde{\mathbf{H}}' = \mathbf{F}_N^{-1} \mathbf{D}^{-1} \tilde{\mathbf{H}} \mathbf{D} \mathbf{F}_N$. The noise vector $\mathbf{n}'' = \mathbf{F}_N^{-1} \mathbf{D}^{-1} \mathbf{F}_M \mathbf{n}$, although having a different size than \mathbf{n} , has its elements statistically equivalent to the ones in \mathbf{n} .

Extrinsic LLRs can be obtained for each symbol, assuming once more BPSK modulation, transmitted over an SC-FDMA system applying the JGA as

$$L[k] = \log \left[\frac{e^{-\frac{1}{2}(\mathbf{y} - \tilde{\mathbf{h}}'[k] - \tilde{\boldsymbol{\zeta}}'[k])^\dagger \tilde{\boldsymbol{\Sigma}}'[k]^{-1} (\mathbf{y} - \tilde{\mathbf{h}}'[k] - \tilde{\boldsymbol{\zeta}}'[k])}}{e^{-\frac{1}{2}(\mathbf{y} + \tilde{\mathbf{h}}'[k] - \tilde{\boldsymbol{\zeta}}'[k])^\dagger \tilde{\boldsymbol{\Sigma}}'[k]^{-1} (\mathbf{y} + \tilde{\mathbf{h}}'[k] - \tilde{\boldsymbol{\zeta}}'[k])}} \right], \tag{3.48}$$

where $\tilde{\mathbf{h}}'[k]$ denotes the k th column of $\tilde{\mathbf{H}}'$, the average interference is given by $\tilde{\boldsymbol{\zeta}}'[k] = \tilde{\mathbf{H}}' \bar{\mathbf{x}} - \tilde{\mathbf{h}}'[k] \bar{x}[k]$, and the covariance matrix of the interference by $\tilde{\boldsymbol{\Sigma}}'[k] = \bar{v} \tilde{\mathbf{H}}' \mathbf{I}[k] \tilde{\mathbf{H}}'^\dagger + \sigma^2 \mathbf{I}$.

To take advantage of the diagonal nature of $\tilde{\mathbf{H}}$, (3.48) can be performed in the frequency domain together with the inverse subcarrier mapping, \mathbf{D}^{-1} , and the inverse DFT of size N , \mathbf{F}_N^{-1} . In order to do so, the following identities can be used

$$\mathbf{y} = \mathbf{F}_N^{-1} \mathbf{D}^{-1} \mathbf{Y}' \tag{3.49}$$

$$\tilde{\mathbf{h}}'[k] x[k] = \mathbf{F}_N^{-1} \mathbf{D}^{-1} \tilde{\mathbf{H}} \mathbf{X}'_{x_k} = \mathbf{F}_N^{-1} \mathbf{D}^{-1} \tilde{\mathbf{H}} \mathbf{D} \mathbf{F}_N \mathbf{0}_{x_k} \tag{3.50}$$

$$\tilde{\boldsymbol{\zeta}}'[k] = \tilde{\mathbf{H}}' \bar{\mathbf{x}} - \tilde{\mathbf{h}}'[k] \bar{x}[k] = \mathbf{F}_N^{-1} \mathbf{D}^{-1} \tilde{\mathbf{H}} \bar{\mathbf{X}}' - \mathbf{F}_N^{-1} \mathbf{D}^{-1} \tilde{\mathbf{H}} \mathbf{X}'_{x_k}, \tag{3.51}$$

where $\mathbf{0}_{x_k}$ denotes a vector of size N with the value of $x[k]$ in its k th position and zeros elsewhere and $\mathbf{X}'_{x_k} = \mathbf{D} \mathbf{F}_N \mathbf{0}_{x_k}$.

Also, in the same way as (3.44), the covariance matrix $\tilde{\Sigma}'[k]$ can be written as

$$\begin{aligned}\tilde{\Sigma}'[k] &= \bar{\nu} \mathbf{F}_N^{-1} \mathbf{D}^{-1} \tilde{\mathbf{H}} \mathbf{D} \mathbf{F}_N \mathbf{I}[k] \mathbf{F}_N^{-1} \mathbf{D}^{-1} \tilde{\mathbf{H}}^\dagger \mathbf{D} \mathbf{F}_N + \sigma^2 \mathbf{I}, \\ &= \mathbf{F}_N^{-1} \mathbf{D}^{-1} \tilde{\Sigma}[k] \mathbf{D} \mathbf{F}_N\end{aligned}\quad (3.52)$$

where the fourth equality is due to the identity $\mathbf{F}_N^{-1} \mathbf{D}^{-1} \mathbf{I} \mathbf{D} \mathbf{F}_N = \mathbf{I}$.

It can be shown that, due to the structure of $\tilde{\Sigma}[k]$, $\tilde{\Sigma}'^{-1}[k] = \mathbf{F}_N^{-1} \mathbf{D}^{-1} \tilde{\Sigma}[k]^{-1} \mathbf{D} \mathbf{F}_N$. Hence, using this identity, (3.49), (3.50), (3.51), and (3.52), the extrinsic LLR for a transmitted symbol $x[k]$, $L[k]$, is obtained according to

$$\log \left[\frac{e^{-\frac{1}{2}((\mathbf{D}\mathbf{F}_N)^{-1}(\mathbf{Y}' - \tilde{\mathbf{H}}\mathbf{X}'_{+1} - (\tilde{\mathbf{H}}\tilde{\mathbf{X}}' - \tilde{\mathbf{H}}\tilde{\mathbf{X}}'_{x[k]}))^\dagger (\mathbf{D}\mathbf{F}_N)^{-1} \tilde{\Sigma}[k]^{-1} \mathbf{D} \mathbf{F}_N (\mathbf{D}\mathbf{F}_N^{-1}(\mathbf{Y}' - \tilde{\mathbf{H}}\mathbf{X}'_{+1} - (\tilde{\mathbf{H}}\tilde{\mathbf{X}} - \tilde{\mathbf{H}}\tilde{\mathbf{X}}'_{x[k]})))}}{e^{-\frac{1}{2}((\mathbf{D}\mathbf{F}_1)^{-1}(\mathbf{Y}' - \tilde{\mathbf{H}}\mathbf{X}'_{-1} - (\tilde{\mathbf{H}}\tilde{\mathbf{X}}' - \tilde{\mathbf{H}}\tilde{\mathbf{X}}'_{x[k]}))^\dagger (\mathbf{D}\mathbf{F}_N)^{-1} \tilde{\Sigma}[k]^{-1} \mathbf{D} \mathbf{F}_N ((\mathbf{D}\mathbf{F}_N)^{-1}(\mathbf{Y}' - \tilde{\mathbf{H}}\mathbf{X}'_{-1} - (\tilde{\mathbf{H}}\tilde{\mathbf{X}} - \tilde{\mathbf{H}}\tilde{\mathbf{X}}'_{x[k]})))}} \right], \quad (3.53)$$

which, since $(\mathbf{D}\mathbf{F}_N)^\dagger = (\mathbf{D}\mathbf{F}_N)^{-1}$, can be simplified to

$$\log \left[\frac{e^{-\frac{1}{2}(\mathbf{Y}' - \tilde{\mathbf{H}}\mathbf{X}'_{+1} - (\tilde{\mathbf{H}}\tilde{\mathbf{X}}' - \tilde{\mathbf{H}}\tilde{\mathbf{X}}'_{x[k]}))^\dagger \tilde{\Sigma}[k]^{-1} (\mathbf{Y}' - \tilde{\mathbf{H}}\mathbf{X}'_{+1} - (\tilde{\mathbf{H}}\tilde{\mathbf{X}} - \tilde{\mathbf{H}}\tilde{\mathbf{X}}'_{x[k]})}}{e^{-\frac{1}{2}(\mathbf{Y}' - \tilde{\mathbf{H}}\mathbf{X}'_{-1} - (\tilde{\mathbf{H}}\tilde{\mathbf{X}}' - \tilde{\mathbf{H}}\tilde{\mathbf{X}}'_{x[k]}))^\dagger \tilde{\Sigma}[k]^{-1} (\mathbf{Y}' - \tilde{\mathbf{H}}\mathbf{X}'_{-1} - (\tilde{\mathbf{H}}\tilde{\mathbf{X}} - \tilde{\mathbf{H}}\tilde{\mathbf{X}}'_{x[k]})}} \right]. \quad (3.54)$$

Clearly, since $\tilde{\mathbf{H}}$ is a diagonal matrix and $\tilde{\Sigma}[k]^{-1}$ can be easily calculated according to (3.46), using (3.54), instead of (3.48) represents great savings in terms of computational complexity. In Section 3.7 the complexity of both methods is compared. A schematic diagram for SC-FDMA using the JGA in the frequency domain is shown in Figure 3.2.

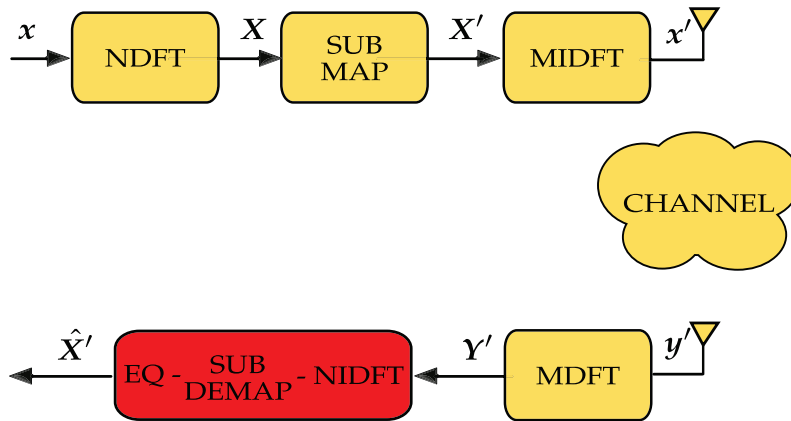


Figure 3.2: Simplified schematics diagram for SC-FDMA using the JGA in the frequency domain.

3.6.1 Multipath MIMO scenario

The expression (3.54) can also be applied for MIMO scenarios. However, the channel matrix $\tilde{\mathbf{H}}$ is now a block diagonal matrix

$$\tilde{\mathbf{H}} = \begin{bmatrix} \tilde{\mathbf{H}}_{f_0} & 0 & 0 & \cdots & 0 \\ 0 & \tilde{\mathbf{H}}_{f_1} & 0 & \cdots & 0 \\ 0 & 0 & \ddots & \ddots & \vdots \\ \vdots & \vdots & \ddots & \ddots & \vdots \\ 0 & 0 & 0 & \cdots & \tilde{\mathbf{H}}_{f_{M-1}} \end{bmatrix}, \quad (3.55)$$

where each submatrix $\tilde{\mathbf{H}}_{f_i}$ is a $N_R \times N_T$ matrix containing the the frequency response of the channel for a particular frequency f_i for all pairs of transmitting and receiving antennas.

Since the covariance matrix $\tilde{\Sigma}[k]$ is a function of $\tilde{\mathbf{H}}$, its inversion can also be obtained by inverting a block diagonal matrix and applying the Sherman-Morrison formula, as in Section 3.5.2. Therefore, inverting $\tilde{\Sigma}[k]$ requires the inversion of all M submatrices in $\tilde{\Sigma}$ to obtain $\tilde{\Sigma}^{-1}$ and then applying the Sherman-Morrison formula to obtain $\tilde{\Sigma}[k]^{-1}$. This task, however, is computationally much more efficient than inverting the $NN_R \times NN_R$ matrix $\tilde{\Sigma}'[k]$.

3.6.2 Extended JGA for SC-FDMA

The same extended JGA methods discussed in Section 3.2 for SISO channels, and in Section 3.4 for MIMO channels, can be straightforwardly applied to frequency-domain equalization of SC-FDMA signals. In fact, as simulations in Chapter 5 indicate, the adoption of these extended methods can lead to noticeable performance gains.

For instance, for detection of BPSK signals over a SISO channel, the extrinsic LLR for a transmitted symbol $x[k]$, taking symbol $x[m]$ out of the interference pool, is given by (3.16) where $P(\mathbf{y}|x[k], x[m])$ is calculated according to

$$\frac{e^{-\frac{1}{2} \left(\mathbf{Y}' - \tilde{\mathbf{H}}(\mathbf{X}'_{x[k]} + \mathbf{X}'_{x[m]}) - (\tilde{\mathbf{H}}\tilde{\mathbf{X}}' - \tilde{\mathbf{H}}(\tilde{\mathbf{X}}'_{x[k]} + \tilde{\mathbf{X}}'_{x[m]})) \right)^\dagger \tilde{\Sigma}[k, m]^{-1} \left(\mathbf{Y}' - \tilde{\mathbf{H}}(\mathbf{X}'_{x[k]} + \mathbf{X}'_{x[m]}) - (\tilde{\mathbf{H}}\tilde{\mathbf{X}} - \tilde{\mathbf{H}}(\tilde{\mathbf{X}}'_{x[k]} + \tilde{\mathbf{X}}'_{x[m]})) \right)}}{\sqrt{(2\pi)^M \det(\tilde{\Sigma}[k, m])}} \quad (3.56)$$

In the same way, for a 2×2 MIMO scenario also using a BPSK signalling scheme, the extrinsic LLR for a transmitted symbol $x_0[k]$ is given by (3.30), where the probability $P(\mathbf{y}|x_0[k], x_1[k])$ is calculated according to

$$e^{-\frac{1}{2} \left(\mathbf{Y}' - \hat{\mathbf{H}}(\mathbf{X}'_{x_0[k]} + \mathbf{X}'_{x_1[k]}) - (\hat{\mathbf{H}}\mathbf{X}' - \hat{\mathbf{H}}(\mathbf{X}'_{x_0[k]} + \mathbf{X}'_{x_1[k]})) \right)^\dagger \tilde{\Sigma}[k]^{-1} \left(\mathbf{Y}' - \hat{\mathbf{H}}(\mathbf{X}'_{x_0[k]} + \mathbf{X}'_{x_1[k]}) - (\hat{\mathbf{H}}\mathbf{X} - \hat{\mathbf{H}}(\mathbf{X}'_{x_0[k]} + \mathbf{X}'_{x_1[k]})) \right)} \frac{1}{\sqrt{(2\pi)^M \det(\tilde{\Sigma}[k])}} \quad (3.57)$$

In next section, a comparison of the complexity of each one of the methods presented in this chapter is made by counting the number of complex multiplications required to detect each symbol.

3.7 Complexity analysis

The computational complexity of the JGA in a multipath SISO scenario, assuming a BPSK modulation, can be assessed via an analysis of (3.8). A schematics diagram of a Simulink[®] implementation of this expression is presented in Figure 3.3. This schematics diagram makes it easier to assess the computational complexity involved in detecting each transmitted symbol. It can also be used to determine which constituent blocks are necessary to implement a JGA equalizer in hardware.

As it can be seen in Figure 3.3, for each symbol under detection using a sliding window of size N , this algorithm requires the following blocks:

- One block $\boxed{\text{Inv}}$ to invert a matrix of size $N \times N$, which requires N^3 complex multiplications (using the Gauss-Jordan method [19]);
- Two blocks $\boxed{\times^2}$ to multiply matrices of size N , which requires N^3 complex multiplications each;
- Four blocks $\boxed{\times}$ to multiply vectors of size N by matrices of size $N \times N$, which requires N^2 complex multiplications each;
- Two blocks $\boxed{\cdot}$ to perform direct product of complex vectors of size N , requiring N multiplications each;
- Six blocks $\boxed{+/-}$ to perform addition or subtraction of complex vectors of size N ;
- Three blocks $\boxed{(\cdot)^\dagger}$ to calculate the conjugate of complex vectors of size N ;

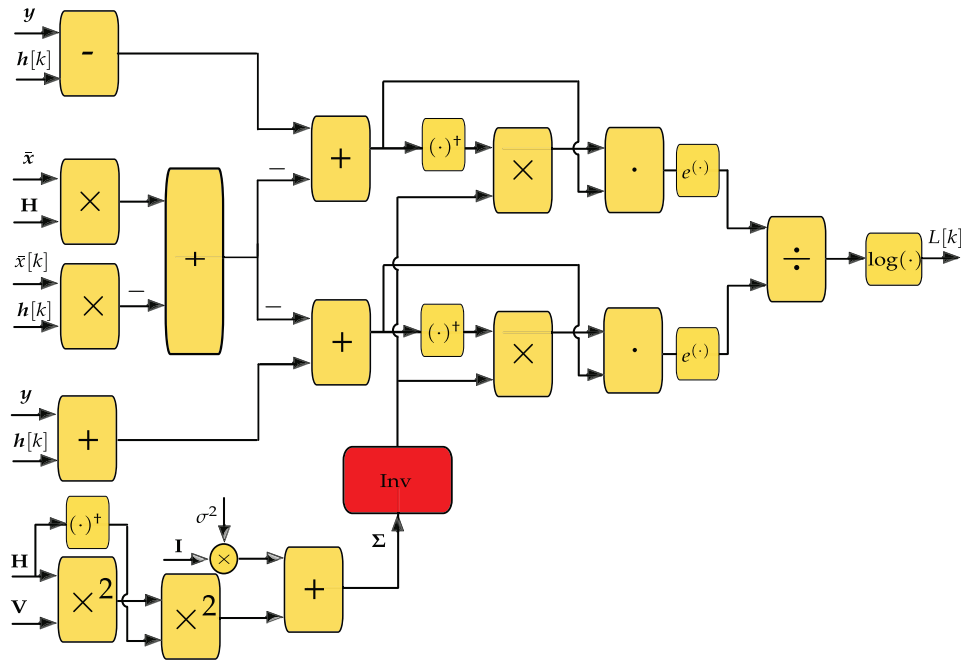


Figure 3.3: JGA Schematics Diagram.

- Two blocks $e^{(\cdot)}$ to calculate exponentials;
- One block \div to divide two complex numbers;
- One block $\log(\cdot)$ to calculate one logarithm.

Exponentials and logarithms can be calculated using lookup tables, making them computationally efficient. Also, complex conjugates can be readily obtained by changing the sign of the complex part of each number in the vector. Hence, their computational complexity can be disregarded. In fact, a close look at Figure 3.3 points out that the burden of this algorithm lies in calculating $\Sigma[k]^{-1}$, which requires two matrix multiplications and one matrix inversion. In Table 3.1, one can see the number of each type of block necessary to implement a JGA equalizer, the number of complex multiplications required by each block, as well as the total number of complex multiplications required to calculate the LLR for each transmitted symbol.

The blocks $+/-$, $(\cdot)^dagger$, $e^{(\cdot)}$, \div , and $\log(\cdot)$ are not taken into account since they do not have a significant computational complexity.

For higher-order modulations, where (3.10) has to be performed for each LLR cal-

Table 3.1: Computational complexity analysis for a JGA equalizer (BPSK modulation).

| | Inv | \times^2 | \times | \cdot |
|-----------------------------|------------|--------------------|----------|---------|
| # Blocks | 1 | 2 | 4 | 2 |
| # Multiplications per block | N^3 | N^3 | N^2 | N |
| Total multiplications | | $3N^3 + 4N^2 + 2N$ | | |

culated from each transmitted symbol, it can be shown that the equalizer will require $2 + 2^m$ $\boxed{\times}$ blocks, and 2^m $\boxed{\cdot}$ blocks, where m denotes the modulation order. It is important to notice that only one matrix inverter and two $\boxed{\times^2}$ blocks are required. The reason behind it is that $\mathbf{\Sigma}$ is the same for all terms in (3.10). In Table 3.2, it is shown the number of each type of block necessary to implement a JGA equalizer, the number of complex multiplications required by each block, as well as the total number of complex multiplications required to calculate each LLR.

Table 3.2: Computational complexity analysis for a JGA equalizer (higher-order modulation).

| | Inv | \times^2 | \times | \cdot |
|-----------------------------|------------|-------------------------------|-----------|---------|
| # Blocks | 1 | 2 | $2 + 2^m$ | 2^m |
| # Multiplications per block | N^3 | N^3 | N^2 | N |
| Total multiplications | | $3N^3 + 2N^2 + 2^m (N^2 + N)$ | | |

Extended JGA

For the extended JGA, equalization is performed according to (3.16). It is shown in Figure 3.4 a schematics diagram of a Simulink[®] implementation of this expression for only one symbol removed from the interference pool (assuming BPSK modulation). This diagram differs from the one in Figure 3.3 for the inclusion of extra branches that are introduced to take into account different combinations of values of $x[k]$ and $x[m]$, and the gains $P(x[m] = +1)$ and $P(x[m] = -1)$ introduced to take into account a priori information about $x[m]$.

It can be seen, in this case, that the number of $\boxed{\text{Inv}}$ and $\boxed{\times^2}$ blocks is kept unchanged, as compared to the JGA case. However, there are now seven $\boxed{\times}$ blocks, as compared to only four, and four $\boxed{\cdot}$ blocks, as compared to only two for the classical JGA. The number of each type of block necessary to implement a JGA equalizer,

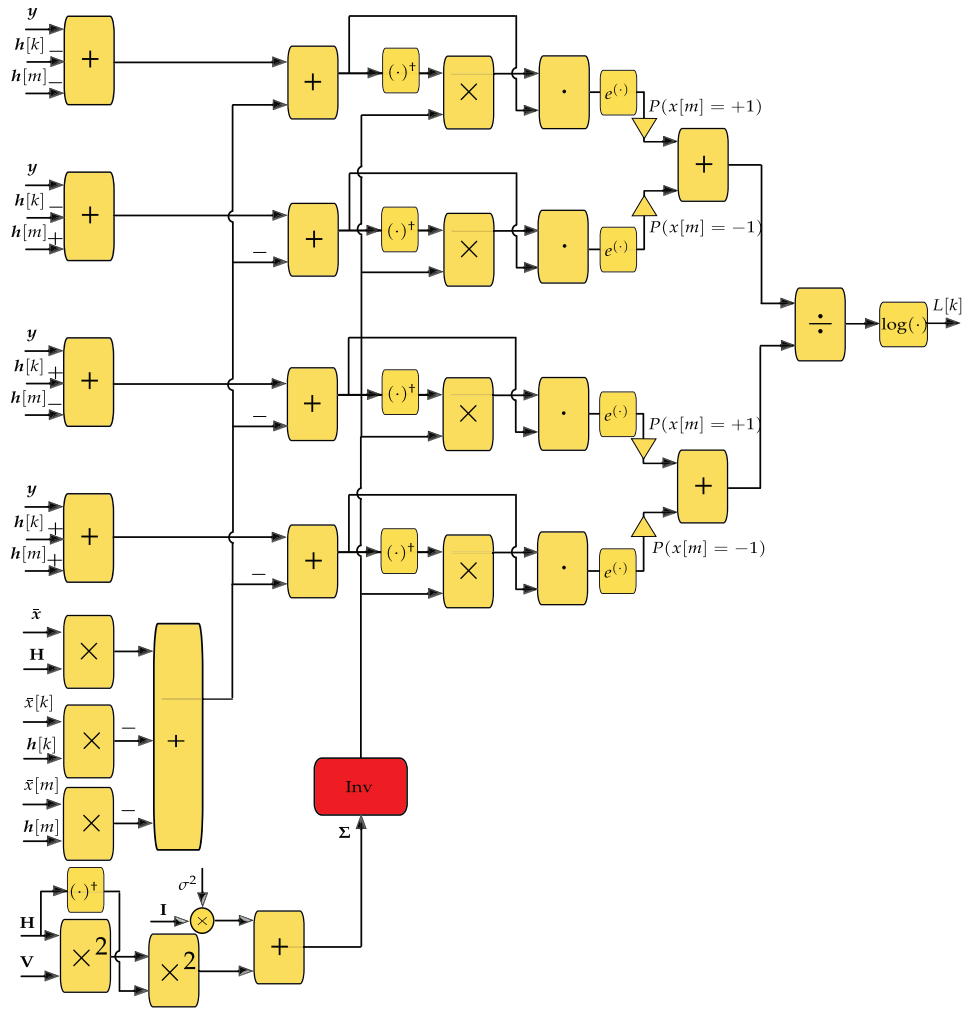


Figure 3.4: Extended JGA Schematics Diagram.

the number of complex multiplications required by each block, as well as the total number of complex multiplications required to calculate each LLR, using the extended JGA, is shown in Table 3.3.

Table 3.3: Computational complexity analysis for an extended JGA equalizer (BPSK modulation with only one symbol removed from the interference pool).

| | Inv | \times^2 | \times | \cdot |
|-----------------------------|--------------------|------------|----------|---------|
| # Blocks | 1 | 2 | 7 | 4 |
| # Multiplications per block | N^3 | N^3 | N^2 | N |
| Total multiplications | $3N^3 + 7N^2 + 4N$ | | | |

For an extended JGA with s symbols removed from the interference pool, and assuming a modulation order m , it is shown in Table 3.4 the number of blocks of each type, the number of complex multiplications per block, as well as the total number of complex multiplications required to obtain each LLR.

Table 3.4: Complexity analysis of an extended JGA equalizer with s symbols removed from $\zeta[k]$ (higher-order modulation).

| | Inv | \times^2 | \times | \cdot |
|-----------------------------|------------------------------------------|------------|-------------------|-----------|
| # Blocks | 1 | 2 | $2 + s + 2^{s+m}$ | 2^{s+m} |
| # Multiplications per block | N^3 | N^3 | N^2 | N |
| Total multiplications | $3N^3 + 2N^2 + sN^2 + 2^{s+m} (N^2 + N)$ | | | |

JGA for SC-FDMA

In Figure 3.5 a schematics diagram for a Simulink[®] implementation of (3.54) is shown, which calculates, working in the frequency domain, LLRs from the transmitted signal. For transmission using an SC-FDMA scheme, and assuming equalization to take place in the frequency domain, the channel matrix $\tilde{\mathbf{H}}$ is diagonal. Hence, the block \times^{2*} in Figure 3.5 requires only M complex multiplications, compared to N^3 for time-domain equalization. Also, when $\tilde{\mathbf{H}}$ multiplies a column vector, only M complex multiplications are necessary, compared to N^2 for time-domain equalization (this operation is shown in Figure 3.5 as \times^*). Moreover, matrix inversion can be performed by inverting each diagonal element of $\tilde{\mathbf{H}}$, block Inv^* , and applying the Sherman-Morrison formula. A schematics implementation of the Sherman-Morrison formula in Simulink[®] is shown in Figure 3.6. In this formula, there is a column vector multiplying a row vector. This operation, which

requires M^2 complex multiplications, is represented by \times^{**} . The division of an $M \times M$ matrix by a constant, which requires M^2 multiplications, is represented by \div^* .

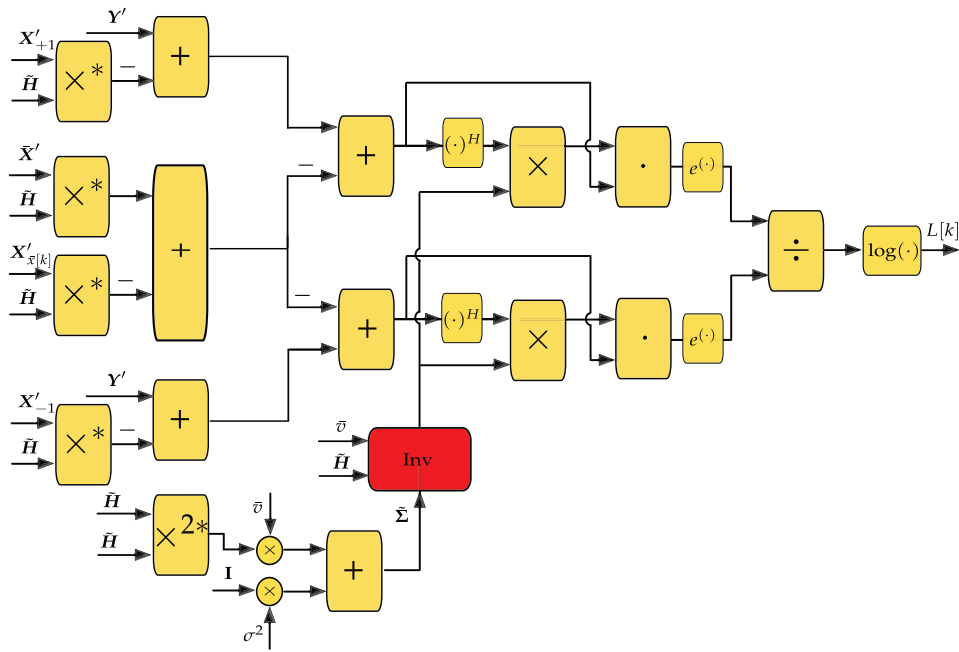


Figure 3.5: SC-FDMA JGA Schematics Diagram.

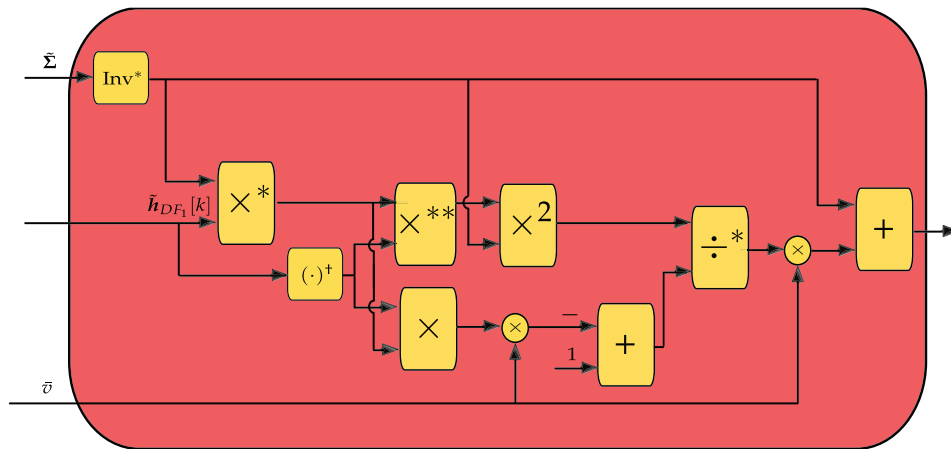


Figure 3.6: SC-FDMA JGA Schematics Diagram 2.

In Table 3.5 it is shown the number of blocks of each type, the number of complex multiplications per block, as well as the total number of complex multiplications required to obtain each LLR, assuming SC-FDMA transmission over a multipath

channel and BPSK modulation.

Table 3.5: Complexity analysis of a JGA equalizer for SC-FDMA transmission (BPSK modulation).

| | Inv | \times^{2*} | \times^* | \times | \cdot |
|-----------------------------|-------------|---------------|------------|-------------|---------|
| # Blocks | 1 | 1 | 4 | 2 | 2 |
| # Multiplications per block | $4M^2 + 2M$ | M | M | M^2 | M |
| Total multiplications | | | | $6M^2 + 9M$ | |

\times^{2*} Diagonal matrix times diagonal matrix.

\times^* Diagonal matrix times column vector.

The results in Table 3.5 can be generalized to an extended JGA scenario with s symbols removed from the interference domain and higher-order modulation, resulting in Table 3.6. First, it is important to note that while applying the Sherman-Morrison formula iteratively, all blocks but $\boxed{\text{Inv}^*}$ are repeated, hence, the number of complex multiplications required by this block is $M + (s + 1)(4M^2 + M)$. Also, the introduction of extra branches to take into account all combinations of symbols $x[k]$ and the ones removed from the interference pool, will increase the computational complexity of the whole algorithm, as shown in Table 3.6, where a modulation order m is assumed.

Table 3.6: Complexity analysis of an extended JGA equalizer for SC-FDMA transmission (higher-order modulation).

| | Inv | \times^2 | \times^* | \times^{**} | \cdot |
|-----------------------|--------------------------------------------------------------|------------|------------------------|---------------|-----------|
| # Blocks | 1 | 1 | $2^m(s + 1) + (s + 2)$ | 2^{m+s} | 2^{m+s} |
| # Mult. per block | * | M | M | M^2 | M |
| Total multiplications | $[2^{m+s} + 4(s + 1)]M^2 + [2^{m+s} + 2^m(s + 1) + 2s + 5]M$ | | | | |

* $M + (s + 1)(4M^2 + M)$

\times^{2*} Diagonal matrix times diagonal matrix.

\times^* Diagonal matrix times column vector.

MIMO scenario

For MIMO multipath scenarios, the computational complexity is calculated in a similar fashion as it has been calculated for multipath SISO scenarios. The only difference is that, instead of using matrices of dimensions $N \times N$ (time domain), or $M \times M$ (frequency domain), matrices of dimensions $NN_R \times NN_T$ or $MN_R \times MN_T$ are used for time-domain and frequency-domain equalization, respectively.

For MIMO frequency-domain equalization, the equalizer has the additional task of inverting $M N_R \times N_R$ matrices, as discussed in Section 3.6.1.

Summary

In Table 3.7, the computational complexity of equalization using the JGA and the extended JGA, both in time and in frequency domain, is listed. A few conclusions can be derived from this table. First, in the time domain, both JGA and extended JGA have the same coefficient for N^3 . Hence, for large values of N , the additional complexity required for the extended method is negligible. It can also be seen in Table 3.7 that performing equalization in the frequency domain results in a computational complexity that grows only quadratically with M , compared to cubically with N for its time-domain counterpart. Thus, unless $M \gg N$, frequency-domain equalization results in great complexity savings. Finally, it can be seen that in the frequency domain, the coefficient of M^2 grows exponentially with s . Therefore, only the removal of small sets of interfering elements is practical for this scenario.

Table 3.7: Total number of complex multiplications required by different equalization schemes.

| Scheme | # Complex multiplications |
|---------------------|----------------------------------------------------------------|
| JGA (time domain) | $3N^3 + 2N^2 + 2^m (N^2 + N)$ |
| EJGA (time domain) | $3N^3 + 2N^2 + sN^2 + 2^{s+m} (N^2 + N)$ |
| JGA (freq. domain) | $[2^m + 4] M^2 + [2^{m+1} + 5] M$ |
| EJGA (freq. domain) | $[2^{m+s} + 4(s + 1)] M^2 + [2^{m+s} + 2^m(s + 1) + 2s + 5] M$ |

Apart from helping to count the number of operations required for each method, the schematics diagrams in Figures 3.3 and 3.4 also show an important property of the extended JGA. Basically, since the extended method introduces new equalization branches in Figure 3.4, most additional operations required by the extended JGA method can be performed in parallel. Hence, even if the number of complex multiplications is significantly higher than the classical JGA, the number of clock cycles required for both systems is nearly the same, as long as the hardware is robust enough to perform all required operations for each branch at the same time.

4

SINR and EXIT Analysis

In this chapter, the improvement in performance obtained by using the extended JGA, instead of the classical JGA is examined via an analysis of the Signal to Noise-plus-Interference Ratio (SINR) at the output of the equalizer. Also, Extrinsic Information Transfer (EXIT) charts are drawn to show how this improvement in the equalizer's performance can translate into an improvement in performance for iterative equalization systems.

4.1 SINR analysis

In most practical communication systems, the correlation introduced by the equalization process is neglected in posterior stages of the detection process. In fact, to guarantee that the correlation introduced will not impair the detection process, an interleaver is introduced before transmission in many standards, like the HS-DPA [1] or the LTE [2]. The reasoning behind the introduction of the interleaver is that it requires a de-interleaver at the receiver side, and the de-interleaving process breaks the correlation between neighbouring symbols at the output of the equalizer. A schematics diagram for a communication system including an equalizer is shown in Figure 4.1(a). This system can be simplified by combining channel, AWGN, and equalizer into a new additive noise-plus-interference term, as shown in Figure 4.1(b). Assuming the noise-plus-interference term to have a Gaussian distribution, this channel can be fully characterized by its SINR.

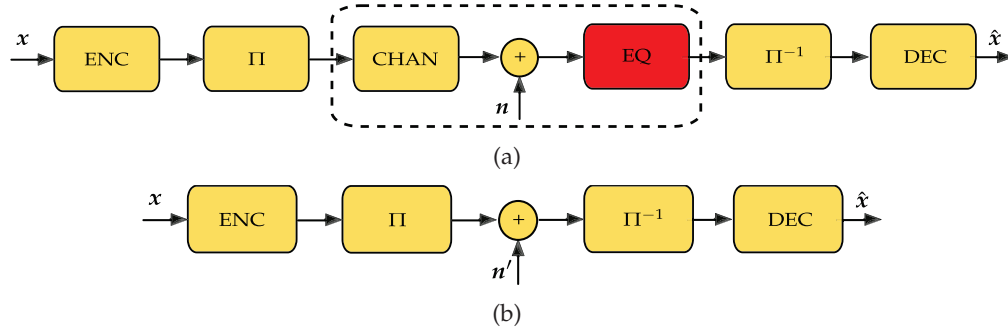


Figure 4.1: Schematics diagram for a multipath communication system.

It can be shown that, for most scenarios, a Gaussian assumption about the equalizer's output is accurate. An example is shown in Figure 4.2. A BPSK modulated signal is transmitted over a channel with tap gains $[0.227, 0.460, 0.688, 0.460, 0.227]$, from now on denoted test channel A¹, at an SNR of 20 dB. At the output of the equalizer, LLRs produced by all positive transmitted symbols are collected and their histogram can be seen in Figure 4.2. It is also shown in this figure the probability density function (pdf) of the LLRs at the output of an AWGN channel at an SNR of 1.82 dB. As it can be seen, there is a close fit between histogram and pdf. It will be shown, in what follows, that this SNR corresponds exactly to the calculated SINR for this particular channel at 20 dB.

4.1.1 SINR for the JGA

As shown in the previous chapter, LLRs at the output of an equalizer applying the JGA for a BPSK modulation are given by

$$L[k] = 2\mathbf{h}[k]^{\dagger}\mathbf{\Sigma}[k]^{-1}(\mathbf{y} - \mathbf{H} \cdot \bar{\mathbf{x}} + \mathbf{h}[k]\bar{x}[k]). \quad (4.1)$$

¹This particular choice of channel was made for two reasons. First, this channel presents a large null in its frequency response, as it can be seen in [4], Chapter 10. Hence, noise enhancement greatly hinders the performance of MMSE (and consequently JGA) equalizers and a more powerful equalizer can incur in significant performance gain. Second, this channel was also used in [25]. By using the same channel, it is possible to make comparisons between their results and results obtained here.

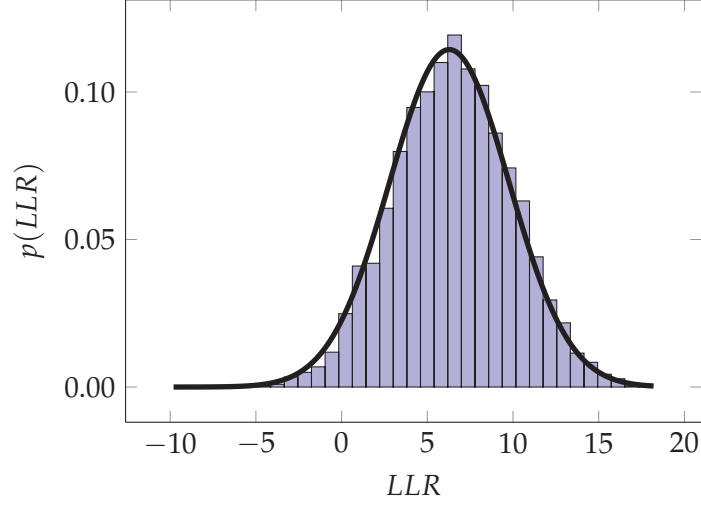


Figure 4.2: Histogram of LLRs at the output of an equalizer for positive transmitted BPSK symbols at 20 dB.

Adding $\mathbf{h}[k]x[k]$ and $-\mathbf{h}[k]x[k]$ to the expression in parenthesis, results in

$$\begin{aligned}
 L[k] &= 2\mathbf{h}[k]^\dagger \boldsymbol{\Sigma}[k]^{-1} (\mathbf{y} - \mathbf{H} \cdot \bar{\mathbf{x}} + \mathbf{h}[k]\bar{x}[k] + \mathbf{h}[k]x[k] - \mathbf{h}[k]x[k]) \\
 &= 2\mathbf{h}[k]^\dagger \boldsymbol{\Sigma}[k]^{-1} \mathbf{h}[k]x[k] + 2\mathbf{h}[k]^\dagger \boldsymbol{\Sigma}[k]^{-1} (\mathbf{y} - \mathbf{H} \cdot \bar{\mathbf{x}} + \mathbf{h}[k]\bar{x}[k] - \mathbf{h}[k]x[k]) \quad (4.2) \\
 &= \mu[k]x[k] + \zeta[k],
 \end{aligned}$$

with $\mu[k] = 2\mathbf{h}[k]^\dagger \boldsymbol{\Sigma}[k]^{-1} \mathbf{h}[k]$ and $\zeta[k] = 2\mathbf{h}[k]^\dagger \boldsymbol{\Sigma}[k]^{-1} (\mathbf{y} - \mathbf{H} \cdot \bar{\mathbf{x}} + \mathbf{h}[k]\bar{x}[k] - \mathbf{h}[k]x[k])$. Since $\boldsymbol{\zeta}[k] = \mathbf{y} - \mathbf{h}[k]x[k]$, $\zeta[k]$ can be rewritten as $2\mathbf{h}[k]^\dagger \boldsymbol{\Sigma}[k]^{-1} (\boldsymbol{\zeta}[k] - \mathbf{H} \cdot \bar{\mathbf{x}} + \mathbf{h}[k]\bar{x}[k])$.

The expression in (4.2) corresponds to a signal to noise-plus-interference form of (4.1). With this expression, one can easily see that the signal power is given by $\mu^2[k]$. Also, since $\bar{\mathbf{x}}$ and $\bar{x}[k]$ depend only on the *a priori* information, they can be removed from the calculation of the variance of the noise-plus-interference term, which is given by [32]

$$\begin{aligned}
 E [\zeta[k]\zeta[k]^\dagger] &= E \left[2\mathbf{h}[k]^\dagger \boldsymbol{\Sigma}[k]^{-1} \boldsymbol{\zeta}[k] \left(2\mathbf{h}[k]^\dagger \boldsymbol{\Sigma}[k]^{-1} \boldsymbol{\zeta}[k] \right)^\dagger \right] \\
 &= 4\mathbf{h}[k]^\dagger \boldsymbol{\Sigma}[k]^{-1} E [\boldsymbol{\zeta}[k]\boldsymbol{\zeta}[k]^\dagger] \boldsymbol{\Sigma}[k]^{-1} \mathbf{h}[k] \quad (4.3) \\
 &= 4\mathbf{h}[k]^\dagger \boldsymbol{\Sigma}[k]^{-1} \boldsymbol{\Sigma}[k] \boldsymbol{\Sigma}[k]^{-1} \mathbf{h}[k] \\
 &= 4\mathbf{h}[k]^\dagger \boldsymbol{\Sigma}[k]^{-1} \mathbf{h}[k] = 2\mu[k].
 \end{aligned}$$

Therefore, the SINR of $L[k]$ at the output of an equalizer applying the JGA, denoted

by $\text{SINR}[k]$, is calculated according to

$$\text{SINR}[k] = \mu^2[k]/2\mu[k] = \mu[k]/2 = \mathbf{h}[k]^\dagger \boldsymbol{\Sigma}[k]^{-1} \mathbf{h}[k]. \quad (4.4)$$

As mentioned at the beginning of this chapter, applying (4.4) to the test channel A, at an SNR of 20 dB with no *a priori* information, an SINR of 1.82 dB is obtained. Hence the tight fit in Figure 4.2.

Figure 4.3 is used to illustrate how accurate the SINR is predicting the performance of a communication system over multipath channels. In this figure, a bit error rate (BER) plot for a BPSK uncoded signal transmitted over an AWGN channel is presented. Also, some BER points for a BPSK uncoded signal transmitted over test channel A are shown, using the SINR at the output of the equalizer, instead of its SNR, as its abscissa. Clearly, there is a very close fit between the BER plot for the uncoded system transmitted over an AWGN channel and the equalized system, indicating that the simplification in Figure 4.1 is accurate.

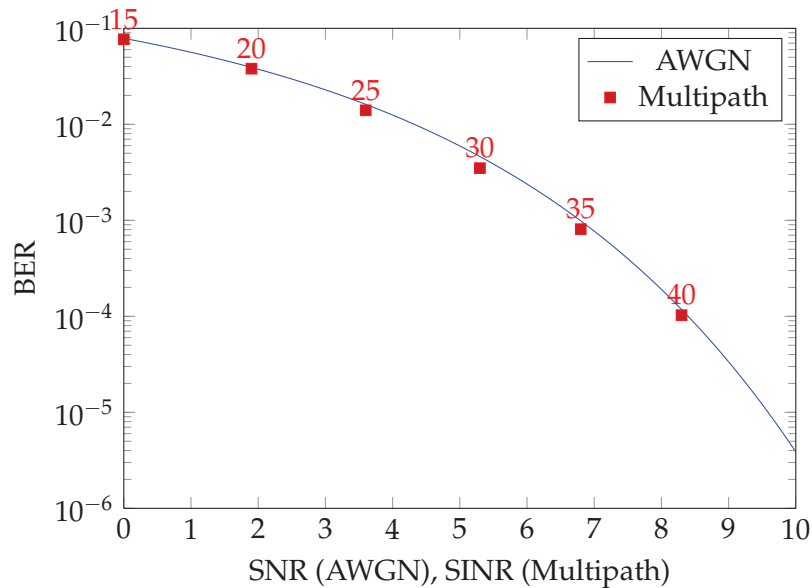


Figure 4.3: BER curves for AWGN and multipath channels (SNRs for multipath channel shown above points).

Another way to verify how well the SINR predicts the equalizer's error performance, assuming once again an uncoded communication system over a multipath channel with AWGN, is to compare simulation results with the theoretical error

performance predicted by [56]

$$BER = Q(1/\sigma) = Q\left(\sqrt{2 \cdot 10^{SINR/10}}\right), \quad (4.5)$$

where $Q(\cdot)$ denotes the Q-function, which is equal to the tail probability of the standard normal distribution.

For the test channel A, it is shown in Figure 4.4 the BER predicted by the SINR using (4.5), as well as the results from a Monte Carlo simulation. Clearly the predicted performance is closely matched by simulation results.

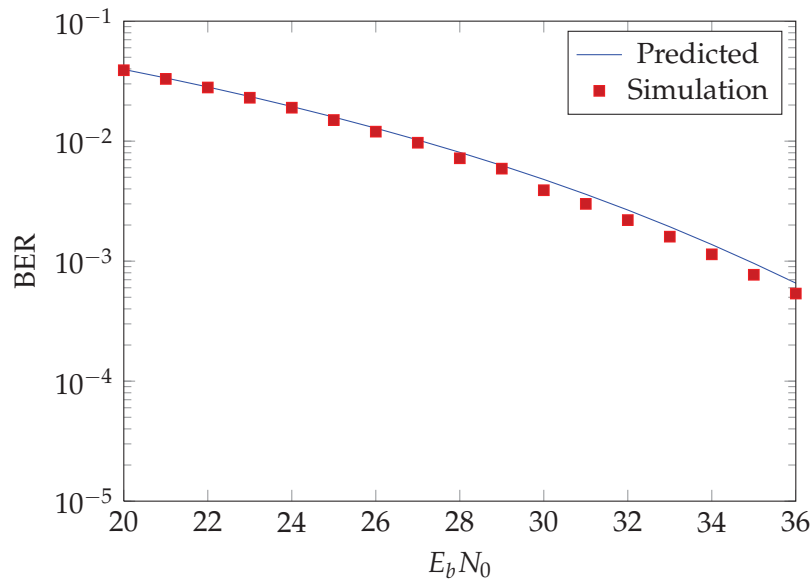


Figure 4.4: Theoretical and simulated BER performances for uncoded BPSK transmission over test channel A.

Higher-order modulations

For higher-order modulations, the extrinsic LLRs are obtained as the logarithm of a ratio between two summations, as seen in (3.10). Hence, these LLRs cannot be written in a simple expression as in (4.1). Nevertheless, an approximation can be made that closely fits the true SINR. This approximation is presented here for a QPSK constellation, as seen in Figure 4.5.

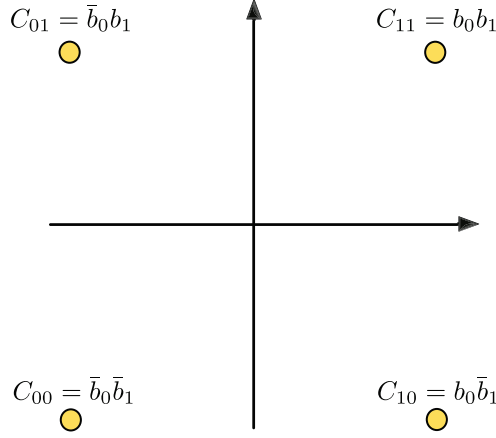


Figure 4.5: QPSK Constellation.

For a QPSK modulation, the value of $L[k]$ in (3.10) is given by

$$\log \left[\frac{e^{-\frac{1}{2}(\mathbf{y}-\mathbf{h}[k]C_{11}-\bar{\boldsymbol{\zeta}}[k])^\dagger \boldsymbol{\Sigma}[k]^{-1}(\mathbf{y}-\mathbf{h}[k]C_{11}-\bar{\boldsymbol{\zeta}}[k])} + e^{-\frac{1}{2}(\mathbf{y}-\mathbf{h}[k]C_{10}-\bar{\boldsymbol{\zeta}}[k])^\dagger \boldsymbol{\Sigma}[k]^{-1}(\mathbf{y}-\mathbf{h}[k]C_{10}-\bar{\boldsymbol{\zeta}}[k])}}}{e^{-\frac{1}{2}(\mathbf{y}-\mathbf{h}[k]C_{01}-\bar{\boldsymbol{\zeta}}[k])^\dagger \boldsymbol{\Sigma}[k]^{-1}(\mathbf{y}-\mathbf{h}[k]C_{01}-\bar{\boldsymbol{\zeta}}[k])} + e^{-\frac{1}{2}(\mathbf{y}-\mathbf{h}[k]C_{00}-\bar{\boldsymbol{\zeta}}[k])^\dagger \boldsymbol{\Sigma}[k]^{-1}(\mathbf{y}-\mathbf{h}[k]C_{00}-\bar{\boldsymbol{\zeta}}[k])}} \right]. \quad (4.6)$$

Assuming, without loss of generality, that C_{11} is transmitted, for most of the time, the inequalities below are true.

$$\begin{aligned} e^{-\frac{1}{2}(\mathbf{y}-\mathbf{h}[k]C_{11}-\bar{\boldsymbol{\zeta}}[k])^\dagger \boldsymbol{\Sigma}[k]^{-1}(\mathbf{y}-\mathbf{h}[k]C_{11}-\bar{\boldsymbol{\zeta}}[k])} &\gg e^{-\frac{1}{2}(\mathbf{y}-\mathbf{h}[k]C_{10}-\bar{\boldsymbol{\zeta}}[k])^\dagger \boldsymbol{\Sigma}[k]^{-1}(\mathbf{y}-\mathbf{h}[k]C_{10}-\bar{\boldsymbol{\zeta}}[k])} \\ e^{-\frac{1}{2}(\mathbf{y}-\mathbf{h}[k]C_{01}-\bar{\boldsymbol{\zeta}}[k])^\dagger \boldsymbol{\Sigma}[k]^{-1}(\mathbf{y}-\mathbf{h}[k]C_{01}-\bar{\boldsymbol{\zeta}}[k])} &\gg e^{-\frac{1}{2}(\mathbf{y}-\mathbf{h}[k]C_{00}-\bar{\boldsymbol{\zeta}}[k])^\dagger \boldsymbol{\Sigma}[k]^{-1}(\mathbf{y}-\mathbf{h}[k]C_{00}-\bar{\boldsymbol{\zeta}}[k])} \end{aligned} \quad (4.7)$$

Hence, (4.6) can be approximated by

$$L[k] \approx \log \left[\frac{e^{-\frac{1}{2}(\mathbf{y}-\mathbf{h}[k]C_{11}-\bar{\boldsymbol{\zeta}}[k])^\dagger \boldsymbol{\Sigma}[k]^{-1}(\mathbf{y}-\mathbf{h}[k]C_{11}-\bar{\boldsymbol{\zeta}}[k])}}{e^{-\frac{1}{2}(\mathbf{y}-\mathbf{h}[k]C_{01}-\bar{\boldsymbol{\zeta}}[k])^\dagger \boldsymbol{\Sigma}[k]^{-1}(\mathbf{y}-\mathbf{h}[k]C_{01}-\bar{\boldsymbol{\zeta}}[k])}} \right]. \quad (4.8)$$

Following the same procedure for the BPSK scenario, (4.8) is rewritten as

$$\begin{aligned} L[k] \approx (\mathbf{h}[k] (C_{11} - C_{01}))^\dagger \boldsymbol{\Sigma}[k]^{-1} (\mathbf{y} - \bar{\boldsymbol{\zeta}}[k]) \\ + \frac{1}{2} \mathbf{h}[k] \boldsymbol{\Sigma}[k]^{-1} \mathbf{h}[k]^\dagger (|C_{11}|^2 - |C_{01}|^2). \end{aligned} \quad (4.9)$$

Since $|C_{11}| = |C_{01}|$, and $\bar{\boldsymbol{\zeta}}[k] = \mathbf{H} \cdot \bar{\mathbf{x}} - \mathbf{h}[k] \bar{x}[k]$, this expression can be further

simplified to

$$L[k] \approx (\mathbf{h}[k] (C_{11} - C_{01}))^\dagger \boldsymbol{\Sigma}[k]^{-1} (\mathbf{y} - \mathbf{H} \cdot \bar{\mathbf{x}} + \mathbf{h}[k] \bar{x}[k]). \quad (4.10)$$

Adding $\mathbf{h}[k]x[k]$ and $-\mathbf{h}[k]x[k]$ to the expression in parenthesis, results in

$$\begin{aligned} L[k] &\approx (\mathbf{h}[k] (C_{11} - C_{01}))^\dagger \boldsymbol{\Sigma}[k]^{-1} \mathbf{h}[k]x[k] \\ &\quad + (\mathbf{h}[k] (C_{11} - C_{01}))^\dagger \boldsymbol{\Sigma}[k]^{-1} (\mathbf{y} - \mathbf{H} \cdot \bar{\mathbf{x}} + \mathbf{h}[k] \bar{x}[k] - \mathbf{h}[k]x[k]) \\ &= \mu[k]x[k] + \zeta[k], \end{aligned} \quad (4.11)$$

where $\mu[k] = (\mathbf{h}[k] (C_{11} - C_{01}))^\dagger \boldsymbol{\Sigma}[k]^{-1} \mathbf{h}[k]$, and $\zeta[k]$ corresponds to the last term in the summation in (4.11).

With (4.11), and calculating $\zeta[k]$ as in (4.3), one obtains

$$\text{SINR}[k] \approx \mu^2[k] / (C_{11} - C_{01}) \mu[k] = (\mathbf{h}[k] (C_{11} - C_{01}))^\dagger \boldsymbol{\Sigma}[k]^{-1} \mathbf{h}[k] (C_{11} - C_{01}), \quad (4.12)$$

which is nearly the same formula for the SINR as in the BPSK scenario (4.4). The only difference is the factor 2 in (4.4) being replaced by $(C_{11} - C_{01})$ in (4.12). This difference is due to the fact the the SINR has to take into account the distance between the closest constellation points. The approximation in (4.12) gets more accurate as the value of the SNR increases.

4.1.2 SINR for the extended JGA

The SINR for an extended JGA detector is also calculated using an approximation as in (4.8). However, since the equalizer has to perform a marginalization over all symbols taken out of the interference pool, care must be taken to include all possible scenarios while calculating the SINR.

For clarity of explanation, the SINR for the extended JGA is presented here by means of an example. A BPSK modulation is used over a channel defined by tap gains $[0.8, 0.6]$. The symbol $x[k-1]$ is removed from the interference pool.

In this scenario, the extended JGA sees the received signal as if a pulse amplitude modulation (PAM) of values -1.4 , corresponding to $x[k] = x[k-1] = 0, -0.2$ ($x[k] = 0, x[k-1] = 1$), 0.2 ($x[k] = 1, x[k-1] = 0$), and 1.4 ($x[k] = x[k-1] = 1$), instead of a BPSK modulation, has been transmitted, as seen in Figure 4.6.

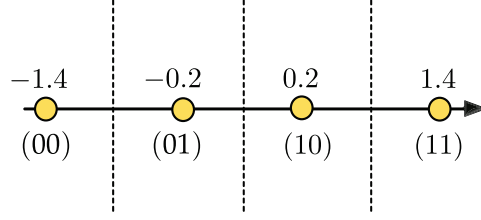


Figure 4.6: Signal constellation for a $[0.8, 0.6]$ channel with BPSK modulation.

If a sequence $x[k] = x[k-1] = 1$ is transmitted, the following inequalities hold for most of the time²,

$$\begin{aligned}
 e^{-\frac{1}{2}(\mathbf{y}-\mathbf{h}[k]-\mathbf{h}[k-1])^\dagger \boldsymbol{\Sigma}[k,k-1]^{-1}(\mathbf{y}-\mathbf{h}[k]-\mathbf{h}[k-1])} &\gg e^{-\frac{1}{2}(\mathbf{y}-\mathbf{h}[k]+\mathbf{h}[k-1])^\dagger \boldsymbol{\Sigma}[k,k-1]^{-1}(\mathbf{y}-\mathbf{h}[k]+\mathbf{h}[k-1])} \\
 e^{-\frac{1}{2}(\mathbf{y}+\mathbf{h}[k]-\mathbf{h}[k-1])^\dagger \boldsymbol{\Sigma}[k,k-1]^{-1}(\mathbf{y}+\mathbf{h}[k]-\mathbf{h}[k-1])} &\gg e^{-\frac{1}{2}(\mathbf{y}+\mathbf{h}[k]+\mathbf{h}[k-1])^\dagger \boldsymbol{\Sigma}[k,k-1]^{-1}(\mathbf{y}+\mathbf{h}[k]+\mathbf{h}[k-1])}
 \end{aligned} \tag{4.13}$$

The first inequality shows that, given the received signal \mathbf{y} , the probability that a sequence [11] has been transmitted is much larger than a [10] sequence. This argument, based on the fact that deviations from the four “constellation points” are due to a Gaussian noise, is specially true when large SNRs are applied. The second inequality shows that, given \mathbf{y} , $p([01]) \gg p([00])$.

For this scenario, (3.16) can be approximated by

$$L[k] \approx \log \left[\frac{e^{-\frac{1}{2}(\mathbf{y}-\mathbf{h}[k]-\mathbf{h}[k-1])^\dagger \boldsymbol{\Sigma}[k,k-1]^{-1}(\mathbf{y}-\mathbf{h}[k]-\mathbf{h}[k-1])}}{e^{-\frac{1}{2}(\mathbf{y}+\mathbf{h}[k]-\mathbf{h}[k-1])^\dagger \boldsymbol{\Sigma}[k,k-1]^{-1}(\mathbf{y}+\mathbf{h}[k]-\mathbf{h}[k-1])}} \right]. \tag{4.14}$$

It can be shown, using the same procedure in the classical JGA scenario, that since the term $-\mathbf{h}[k-1]$ appears both on the numerator and denominator, it is cancelled out and the SINR is given by

$$\text{SINR}[k] = \mathbf{h}[k]^\dagger \boldsymbol{\Sigma}[k,k-1]^{-1} \mathbf{h}[k]. \tag{4.15}$$

Hence, for this scenario, the only difference from the SINR obtained for the classical JGA approach is that the covariance matrix $\boldsymbol{\Sigma}[k,k-1]$, calculated according to 3.14, is used instead of $\boldsymbol{\Sigma}[k]$, calculated according to 3.6.

When a sequence $x[k] = 1$, $x[k-1] = 0$ is transmitted, the inequalities that hold

²For the sake of space, the terms $\bar{\xi}[k]$, common to all exponents, are omitted.

for most of the time are now

$$\begin{aligned} e^{-\frac{1}{2}(\mathbf{y}-\mathbf{h}[k]+\mathbf{h}[k-1])^\dagger \boldsymbol{\Sigma}[k,k-1]^{-1}(\mathbf{y}-\mathbf{h}[k]+\mathbf{h}[k-1])} &\gg e^{-\frac{1}{2}(\mathbf{y}-\mathbf{h}[k]-\mathbf{h}[k-1])^\dagger \boldsymbol{\Sigma}[k,k-1]^{-1}(\mathbf{y}-\mathbf{h}[k]-\mathbf{h}[k-1])} \\ e^{-\frac{1}{2}(\mathbf{y}+\mathbf{h}[k]-\mathbf{h}[k-1])^\dagger \boldsymbol{\Sigma}[k,k-1]^{-1}(\mathbf{y}+\mathbf{h}[k]-\mathbf{h}[k-1])} &\gg e^{-\frac{1}{2}(\mathbf{y}+\mathbf{h}[k]+\mathbf{h}[k-1])^\dagger \boldsymbol{\Sigma}[k,k-1]^{-1}(\mathbf{y}+\mathbf{h}[k]+\mathbf{h}[k-1])} \end{aligned} \quad (4.16)$$

For this particular scenario, (3.16) can be approximated by

$$L[k] \approx \log \left[\frac{e^{-\frac{1}{2}(\mathbf{y}-\mathbf{h}[k]+\mathbf{h}[k-1])^\dagger \boldsymbol{\Sigma}[k,k-1]^{-1}(\mathbf{y}-\mathbf{h}[k]+\mathbf{h}[k-1])}}{e^{-\frac{1}{2}(\mathbf{y}+\mathbf{h}[k]-\mathbf{h}[k-1])^\dagger \boldsymbol{\Sigma}[k,k-1]^{-1}(\mathbf{y}+\mathbf{h}[k]-\mathbf{h}[k-1])}} \right]. \quad (4.17)$$

Now, since the sign of $\mathbf{h}[k-1]$ changes from the numerator to denominator, the SINR can be calculated as

$$\text{SINR}[k] = (\mathbf{h}[k] - \mathbf{h}[k-1])^\dagger \boldsymbol{\Sigma}[k, k-1]^{-1} (\mathbf{h}[k] - \mathbf{h}[k-1]). \quad (4.18)$$

Extensive simulation showed that the inequalities in (4.16) are only true for channels greatly affected by ISI. For instance, in a flat fading channel, which can be represented in matrix form as an identity matrix, the approximation in (4.17) is not valid. For channels mildly affected by ISI, the output of the equalizer has only one SINR, calculated according to (4.15), associated to it.

It is easy to show that, in the case of a sequence $x[k] = 0$, $x[k-1] = 1$, the same result as in (4.18) is obtained, while for $x[k] = 0$, $x[k-1] = 0$, the resultant SINR is the same as in (4.15).

Basically what the discussion above shows is that the extended JGA will output two different SINRs, depending on the received sequence. A higher SINR for the sequences that results in 1.4 or -1.4 and a smaller one for sequences resulting in 0.2 or -0.2 . This result is expected since, in a PAM modulation, some symbols are more protected than others against the effects of noise.

For the test channel A, using an SNR of 15 dB, the SINR values obtained for the two scenarios described above are $\text{SINR}_1 = 13.18$ dB and $\text{SINR}_2 = 10.51$ dB. Since each scenario has an occurrence rate of 50%, a histogram of the LLRs at the output of the detector, for only the positive transmitted symbols, should be fitted by the

following probability density function

$$p(LLR) = \frac{0.5}{\sqrt{2\pi(2/\sigma_1)^2}} e^{\left(-\frac{(x-2/\sigma_1^2)^2}{2(2/\sigma_1)^2}\right)} + \frac{0.5}{\sqrt{2\pi(2/\sigma_2)^2}} e^{\left(-\frac{(x-2/\sigma_2^2)^2}{2(2/\sigma_2)^2}\right)}. \quad (4.19)$$

In Figure 4.7, it can be seen that there is a nearly perfect fit between the histogram of LLRs obtained at the output of an extended JGA and (4.19).

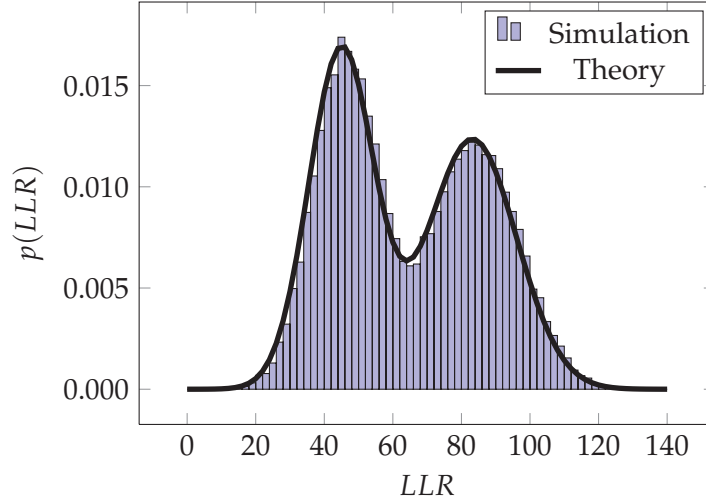


Figure 4.7: Histogram of LLRs at the output of an extended JGA equalizer for positive transmitted BPSK symbols at 15 dB.

In the same way as for the JGA, the SINR can be used to predict the BER of uncoded signals transmitted over multipath AWGN channels when an extended JGA is used. For test channel A, and assuming that the symbol $x[k-1]$ is removed from the interference pool, the BER can be predicted by

$$BER = Q\left(\sqrt{2 \cdot 10^{SINR_1/10}}\right) \cdot 0.5 + Q\left(\sqrt{2 \cdot 10^{SINR_2/10}}\right) \cdot 0.5. \quad (4.20)$$

In Figure 4.8, the predicted error performance is plotted together with Monte Carlo simulation results. As in the classical JGA, the predicted performance is very close to the simulation results.

For higher order modulations and/or a higher number of symbols taken out of the interference pool, the methodology to calculate the SINR is essentially the same. Only more scenarios have to be taken into account. For instance, assuming that both symbols $x[k-1]$ and $x[k+1]$ are taken out of the interference pool, the pre-

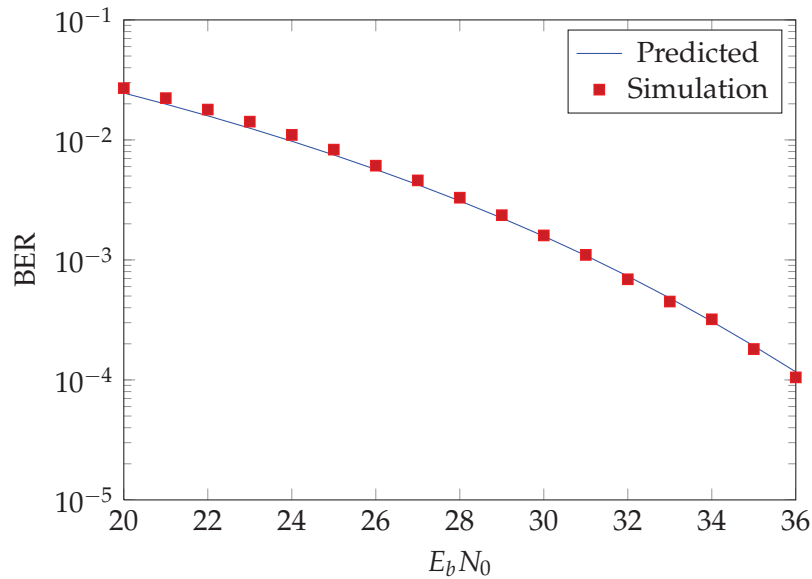


Figure 4.8: BER performance for the extended JGA with $x[k-1]$ removed from the interference pool for channel test A.

dicted and simulated results for the BER for test channel A can be seen in Figure 4.9.

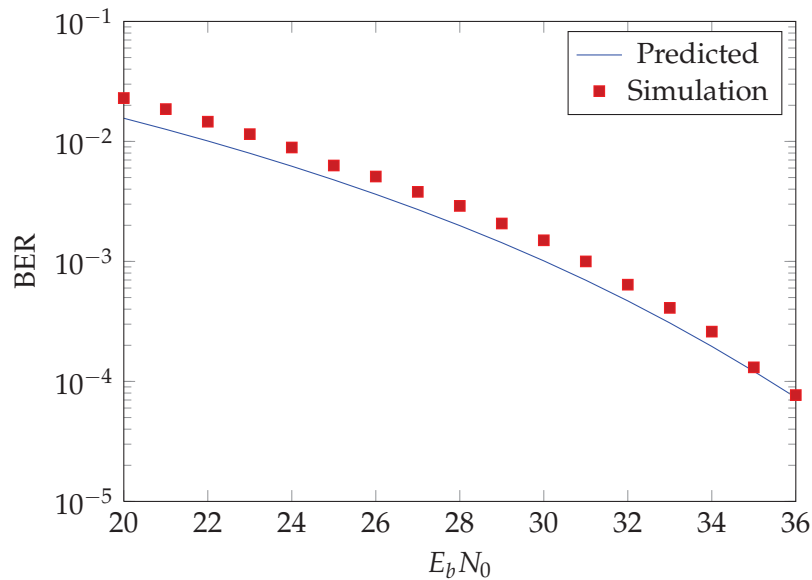


Figure 4.9: BER performance for the extended JGA with $x[k-1]$ and $x[k+1]$ removed from the interference pool for channel test A.

The analysis carried out here so far, only dealt with non-iterative systems. In the

next section, EXIT charts are combined with the SINR analysis in order to assess gains in performance obtained by iterative detection.

4.2 EXIT charts

Extrinsic information transfer charts, hereinafter denoted EXIT charts, are a tool to visualize the convergence behaviour of iterative detecting schemes. They were first proposed by ten Brink [57] to analyze the exchange of extrinsic information for iterative demapping-decoding schemes. Later, they were used to analyze the convergence of iterative decoders for parallel concatenated convolutional codes [58] (better known as turbo codes, [22]). EXIT charts became a standard tool to analyze iterative detectors since they can accurately predict the turbo-cliff position, i.e., the SNR range for which performance improves abruptly, without having to rely on lengthy Monte Carlo simulations.

In this work, EXIT charts are used to analyze the convergence behaviour of iterative detectors consisting of a soft-input soft-output equalizer and a soft-input soft-output decoder. A brief description of this method follows, introducing the notation used throughout remaining sections. For a more comprehensive discussion about EXIT charts, see [59].

4.2.1 Extrinsic transfer characteristics

EXIT charts model the equalizer and decoder as functions that map a sequence of observations and *a priori* information (equalizer) or only observations (decoder) into a new sequence of LLRs.

The convergence behaviour is tracked by these charts with the analysis of the mutual information between the *a posteriori* information and the transmitted symbols, i.e., $I(L_e; X)$ ³, as a function of the the mutual information between the *a priori* information and the transmitted symbols, i.e., $I(L_i; X)$.

³In fact, the proper notation should be $I(L_e[k]; x[k])$. However, since the mutual information is calculated taking into account the pdf of L_e , instead of each instantaneous value, the mutual information is independent of k , and therefore, this index has been dropped. X represents all random variables $x[k]$.

For a BPSK transmission, it can be shown that⁴,

$$\begin{aligned} I(L_i; X) &= \sum_{x=-1,1} \int_{-\infty}^{\infty} p_{L_i}(\xi, X=x) \log_2 \left[\frac{p_{L_i}(\xi, X=x)}{p_{L_i}(\xi)p(X=x)} \right] d\xi \\ &= \frac{1}{2} \sum_{x=-1,1} \int_{-\infty}^{\infty} p_{L_i}(\xi|X=x) \log_2 \left[\frac{2p_{L_i}(\xi|X=x)}{p_{L_i}(\xi|x=1) + p_{L_i}(\xi|x=-1)} \right] d\xi. \end{aligned} \quad (4.21)$$

From (4.21) it is clear that one needs to know $p_{L_i}(\xi|X=x)$ to calculate $I(L_i; X)$. To solve this problem, the following observations, obtained by extensive simulation, are made:

- For large interleavers, the *a priori* values, L_i , remain fairly uncorrelated to the channel's observation, y , over the iterative process;
- The probability density function $p_{L_i}(\xi|X=x)$ approaches a Gaussian distribution as the iterative process continues.

These observations suggest that it is possible to model the *a priori* information as $L_i = \mu_{L_i}X + N_{L_i}$, where X is the transmitted vector, N_{L_i} is a vector of zero-meaned Gaussian variables with variance σ_i^2 , and μ_{L_i} is equal to $\sigma_i^2/2$ [58]. With this assumption, $p_{L_i}(\xi|X=x)$ can be calculated as

$$p_{L_i}(\xi|X=x) \approx \frac{1}{\sqrt{2\pi}\sigma_i} e^{-\frac{(\xi - x\sigma_i^2/2)^2}{2\sigma_i^2}}. \quad (4.22)$$

To obtain $I(L_e; X)$, i.e., the mutual information at the output of the equalizer (or decoder), one has to solve an equation similar to (4.21). The only difference is that $p_{L_i}(\xi|X=x)$ is replaced by $p_{L_e}(\xi|X=x)$. This latter distribution is obtained by observing the histogram of the outputted LLRs.

The crucial observation made in [57] is that the sequence of LLRs at the output of the equalizer (as well as at the decoder) is also close to a distribution given by (4.22), with σ_i^2 being replaced by another variance σ_e^2 . Therefore, it's possible to track the behaviour of the iterative detector by assuming that the mutual information at the output of the equalizer, $I_E(L_e; X)$, is equal to the mutual information at the input of the decoder $I_D(L_i; X)$ and vice versa. At the first iteration, no *a priori* information is available, hence $I_E(L_i; X)$ is assumed to be zero in this case.

⁴A detailed introduction to mutual information and other subjects in information theory can be found in [60].

To draw the mutual information curves for both equalizer and decoder, it is first necessary to obtain a relationship between σ_i^2 and $I(L_i; X)$. Substituting (4.22) in (4.21),

$$I(L_i; X) = 1 - \frac{1}{\sqrt{2\pi\sigma_i^2}} \int_{-\infty}^{\infty} \exp\left(-\frac{(\xi - \sigma_i^2/2)^2}{2\sigma_i^2}\right) \log_2(1 + \exp(-\xi)) d\xi, \quad (4.23)$$

which, can be calculated via numerical integration, generating the curve shown in Figure 4.10.

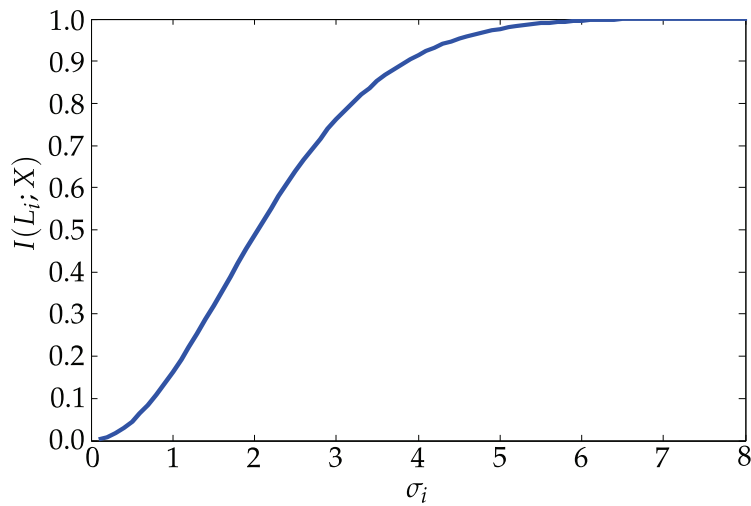


Figure 4.10: Mutual information as a function of σ_i .

Mutual information curves, as mentioned before, are obtained by drawing $I(L_e; X)$ as a function of $I(L_i; X)$. In an iterative detection system, the *a posteriori* mutual information for the equalizer corresponds to the *a priori* mutual information for the decoder and vice versa. Therefore, one can check if an iterative detector will converge to the proper solution, at a given SNR, by observing if there is a convergence path between the EXIT charts for the equalizer and the decoder, switching the axis of the EXIT chart for the decoder.

Example

EXIT curves for JGA equalizers are shown in Figure 4.11, together with the EXIT curve for a convolutional decoder. The multipath channel is the test channel A. The equalizer applies the JGA and the code used is a systematic recursive convolutional

code, defined in polynomial form as $[1, (1 + D^2 + D^3)/(1 + D + D^2 + D^3)]$.

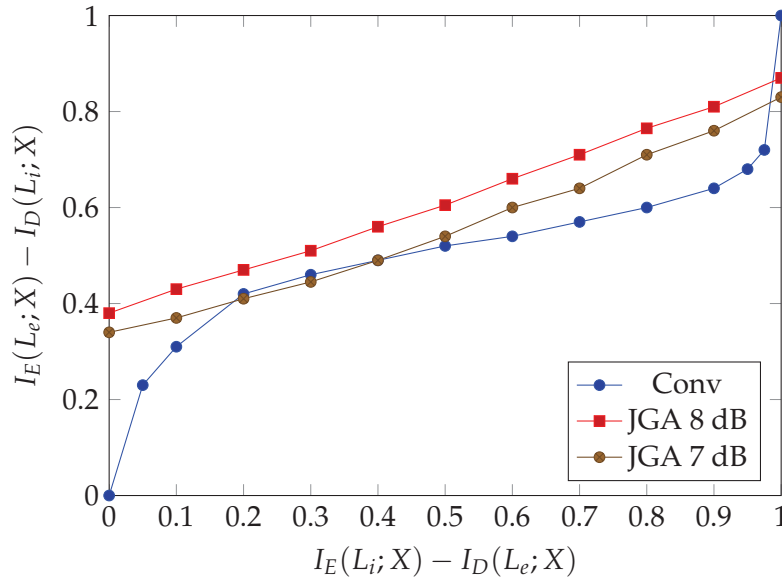


Figure 4.11: EXIT charts for “open-tunnel” and “intersection” scenarios.

As shown in the legend, the only difference between the two curves for the JGA equalizer is the SNR used⁵. For an SNR of 7 dB there is an intersection between equalizer and decoder’s curves. Hence, at the intersection, the mutual information at the output of the equalizer (or decoder) is smaller than its input and further iterations won’t increase the mutual information. For an SNR of 8 dB, however, there is no intersection between equalizer and decoder curves, thus the mutual information has an open-tunnel to increase the reliability of the transmitted information with consecutive iterations.

EXIT chart approximation

EXIT curves are obtained via analysis of histograms of the LLRs at the output of the detector. Clearly, in order to obtain reliable results, thousands of LLRs have to be obtained for each possible value of the mutual information at the detector’s input (*a priori* information). Therefore, obtaining EXIT curves for thousands of channels, in order to determine the average gain in throughput, is computationally infeasible.

⁵Note that since the decoder doesn’t have access to the observations \mathbf{y} , its curve doesn’t change for different values of SNR.

Assuming the output of the equalizer to be Gaussian, the mutual information can be calculated from the SINR using the following equation.

$$I(L_i; X) = 1 - \frac{1}{\sqrt{2\pi\sigma_e^2}} \int_{-\infty}^{\infty} \exp\left(-\frac{(\xi - \sigma_e^2/2)^2}{2\sigma_e^2}\right) \log_2(1 + \exp(-\xi)) d\xi, \quad (4.24)$$

where the variance σ_e^2 is calculated as $\sigma_e^2 = 4/\sigma^2$, and σ^2 is the variance of the noise plus interference term obtained as $\sigma^2 = 1/\sqrt{2 \cdot 10^{\text{SINR}/10}}$.

With this Gaussian assumption on the LLRs at the equalizer's output, EXIT curves can be easily obtained using the SINR, as discussed in last section, together with (4.24). In Figure 4.12 it is shown how this approximation closely matches the EXIT curves obtained via histogram analysis for test channel A at an SNR of 7 dB. For the extended JGA, where two or more SINRs are associated with each channel for a given SNR, the average SINR is used.

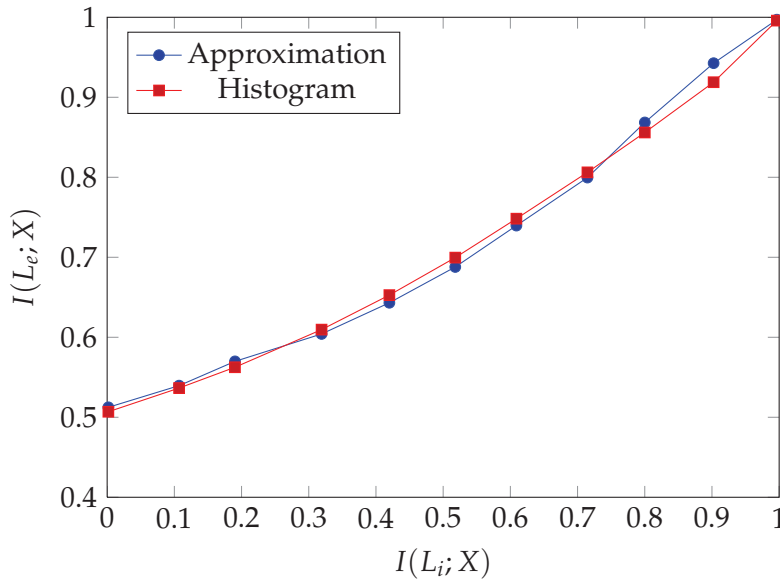


Figure 4.12: EXIT curves for a JGA detector obtained via approximation and via histogram analysis.

4.2.2 Comparing EXIT charts for JGA and extended JGA

EXIT charts can be used to determine the improvement in performance obtained by using the extended JGA, instead of the classical JGA, in iterative detection schemes.

In order to do so, one has to plot the EXIT curves of one equalizer using the JGA, one equalizer using the extended JGA, and the EXIT curves of the decoder in the same graph.

In Figure 4.13, one can see the EXIT curves of a decoder for a convolutional code, defined in polynomial form as $[1, (1 + D^2 + D^3)/(1 + D + D^2 + D^3)]$, as well as EXIT curves for equalizers using the JGA and the extended JGA for the test channel A at 7dB. Clearly, using the extended JGA, there is an “open-tunnel” between equalizer and decoder EXIT curves, allowing the detector to converge to the proper solution. For the JGA, the equalizer and decoder curves intersect and the detector does not converge to the proper solution.

Both equalizer EXIT curves converge to the same point as $I_D(L_e; X) \rightarrow 1$ in Figure 4.13. This is always the case for the extended JGA compared to the classical JGA for the same SNR. This behaviour can be explained by taking a close look at (3.8), (3.14), and (3.15). With perfect knowledge about the transmitted signal, the variance of all transmitted symbols is null, hence for this scenario $\Sigma[k, m] = \Sigma[k]$. Also, $P(x[m])$ will be equal to one for the correct value of $x[m]$ and zero for all other values, hence the LLRs obtained performing (3.15) or (3.8) are the same. In fact, for this scenario, all interference is cancelled out by the mean value of the interference in (3.8) or (3.15), and the system performs as if only AWGN were present.

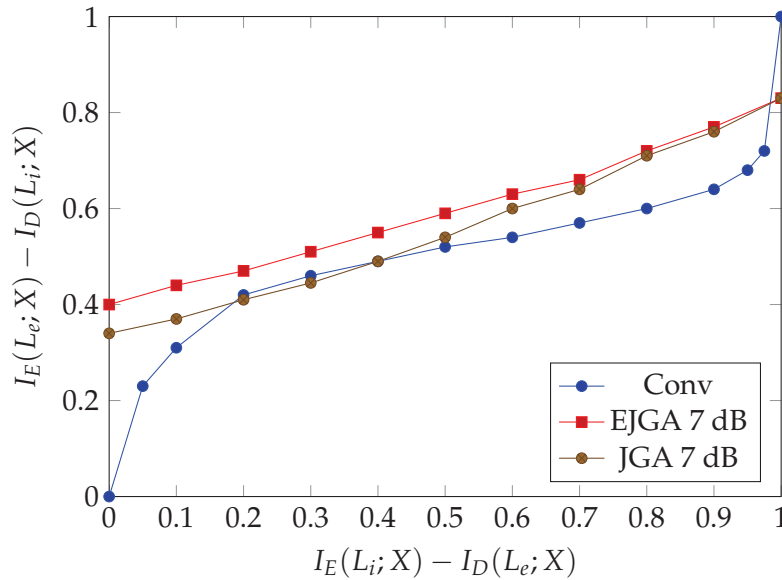


Figure 4.13: EXIT charts for equalizers using the JGA and the extended JGA.

In the following chapter, analysis results obtained in this chapter are verified via Monte Carlo simulations. Also, average throughput gains are obtained using results in this chapter for realistic channels obtained using the SCM.

5

Experimental Results

In this chapter, simulation results for equalization and turbo equalization schemes applying the JGA and the extended JGA are presented. As it will be shown in what follows, results obtained via Monte Carlo simulation corroborate the analysis results obtained in the previous chapter.

5.1 Uncoded system

For an uncoded system using a BPSK modulation over the test channel A, Figure 5.1 shows the improvement in performance obtained by equalizers using the extended JGA with only $x[k - 1]$ removed from the interference pool (EJGA1), and the extended JGA with both $x[k - 1]$ and $x[k + 1]$ removed from the interference pool, compared to the performance of an equalizer using the JGA. As one can see, gains of nearly 4 dB and 5 dB can be obtained at a BER of 10^{-4} , for the EGJA1 and EGJA2, respectively. However, even with two symbols removed from the interference pool, the extended JGA still performs over 20 dB worse than an equalizer using a maximum likelihood algorithm (ML).

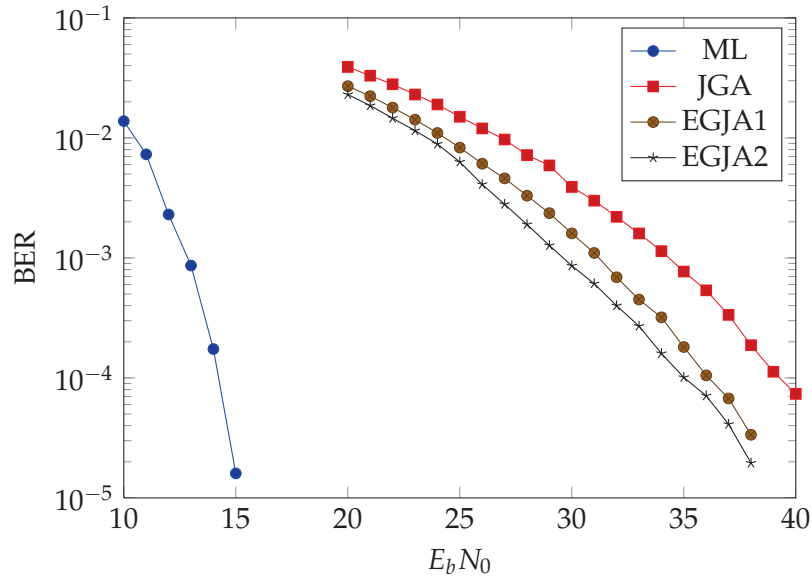


Figure 5.1: Performance curves for different equalizers over test channel A (uncoded system).

5.2 Iterative equalization system - SISO scenario

For an iterative equalization scenario, a communication system whose schematics diagram can be seen in Figure 5.2 was implemented in Simulink[®]. A systematic recursive convolutional code with constraint length $v = 4$, defined in polynomial form as $[1, (1 + D^2 + D^3)/(1 + D + D^2 + D^3)]$ is used together with a block interleaver of size $N = 4096$. Assuming once again BPSK modulation over the test channel A, the performance of an equalizer using the JGA as a function of the number of iterations is shown in Figure 5.3.

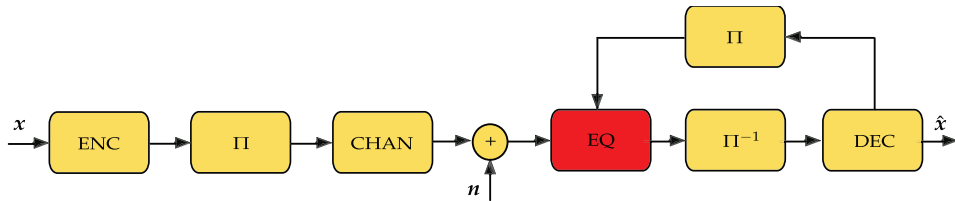


Figure 5.2: Iterative equalization system schematics diagram.

In Figure 5.3, one can see the dramatic improvement in performance obtained by an iterative system, as compared to its non-iterative counterpart. Also, the turbo-

cliff region, i.e., the $E_b N_0$ interval for which the BER improves abruptly, is located at around 8 dB, as predicted by EXIT chart analysis carried out in last chapter (see Figure 4.11).

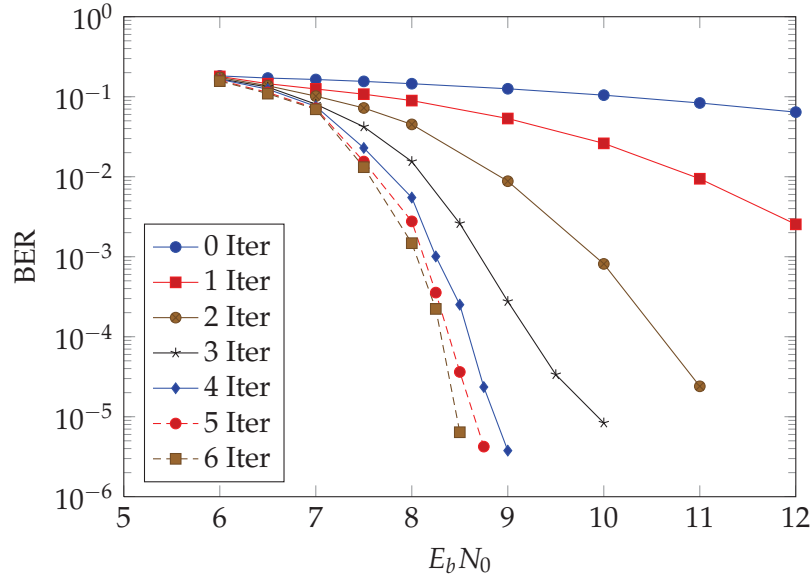


Figure 5.3: Performance curves for an iterative equalization system using the JGA.

A similar result is obtained for an iterative system using the same convolutional code and an equalizer applying an extended JGA, where symbols $x[k-1]$ and $x[k+1]$ are removed from the interference pool, in Figure 5.4. For this scenario, the turbo-cliff region is located around 7 dB, as predicted by EXIT chart analysis carried out in last chapter (see Figure 4.13).

Comparing performances of iterative systems using the JGA, extended JGA and the optimal MAP algorithm [25] for six iterations, one can see in Figure 5.5 that for a BER of 10^{-4} the extended JGA (with $x[k-1]$ and $x[k+1]$ removed from the interference pool) performs 1.5 dB better than the classical JGA. Also, this method performs only 2 dB worse than the optimal MAP algorithm. This figure also presents results for the low-complexity (LC) method presented in Section 3.5.2. This approximation results in a performance loss of less than 0.5 dB for both cases, while providing significant savings in terms of computational complexity.

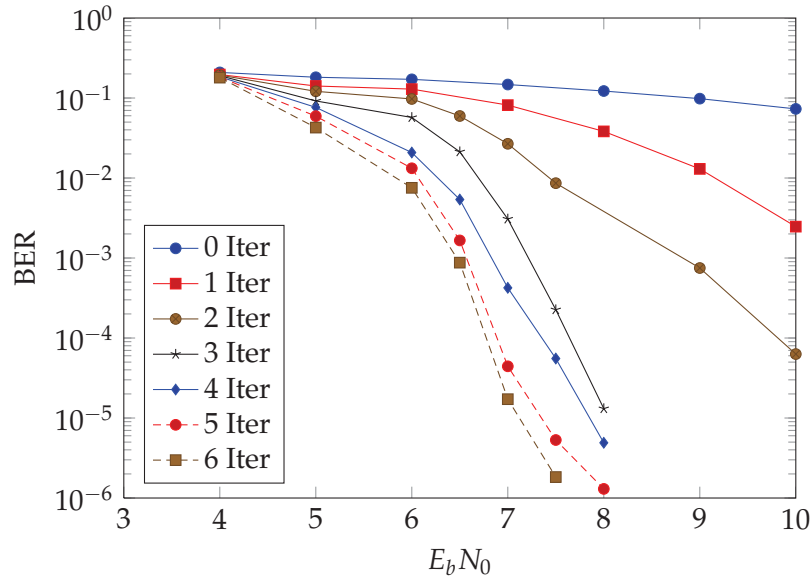


Figure 5.4: Iterative convolutional extended JGA.

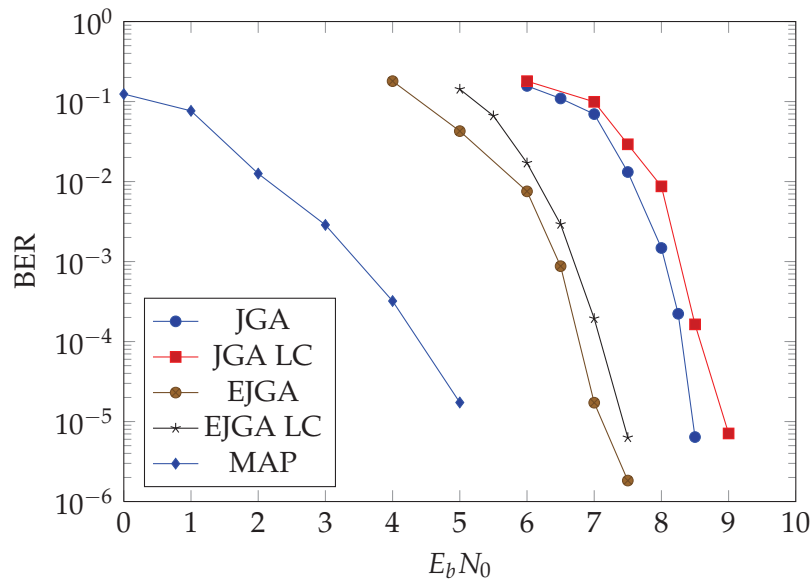


Figure 5.5: Iterative convolutional JGA and extended JGA (regular and LC implementations) for the test channel A.

5.3 SINR analysis - SISO scenario

Five hundred normalized channels were generated in MATLAB[®] using the SCM [48]. The scenarios applied were urban macrocell, suburban macrocell, and urban microcell. A sampling rate of 1 MHz was used for a 2 GHz carrier frequency. Each channel is drawn as a point in Figures 5.6, 5.7, and 5.8, where one axis represents the SINR at the output of the detector for the JGA while the other represents the SINR for extended JGA (EJGA) with one symbol removed from the interference pool. Each SINR was obtained for an SNR of 10 dB, and a QPSK modulation was used.

In channels for which the output of the extended JGA presents two SINRs, an average SINR is used in Figures 5.6, 5.7, and 5.8, since, for several error control codes, the decoder's performance for these scenarios is similar to the performance of a decoder working on an AWGN channel with the SNR equal to this average SINR. Hence, the averaged SINR is the most significant figure of merit in coded systems. The reason behind this behaviour is that, imagining each codeword as a point in a multi-dimensional space, the received signal will deviate from the transmitted signal in some dimensions according to one SINR, and in other dimensions according to the other SINR. For a number of dimensions large enough, the total deviation is statistically similar to the total deviation from a flat channel with an SNR equal to the average SINR.

From Figures 5.6, 5.7, and 5.8, it is clear that the extended JGA always enhances the system's performance (compared to the JGA), as evidenced by the fact that, dividing the plot in two with a diagonal black line, there are no points lying in the lower triangle. It can also be seen that, for some channels, gains of up to 2 dB and even 3 dB were obtained.

The SINR analysis can also be used to predict the potential in terms of throughput gain obtained by using the extended method, as opposed to the regular JGA, for a given communications standard. For instance, in the HSDPA standard (see Appendix B), the number of bits of information per packet (# bits) is determined according to the SINR range, [61]. Hence, the SINR gain obtained by using an extended JGA, instead of a regular JGA, translates directly into a throughput gain, as seen on Table 5.1. In this table, it can be seen that the extended JGA provides gains of 18%, 10% and 19% for urban macrocells, suburban macrocells, and urban microcells respectively for an SNR of 10 dB.

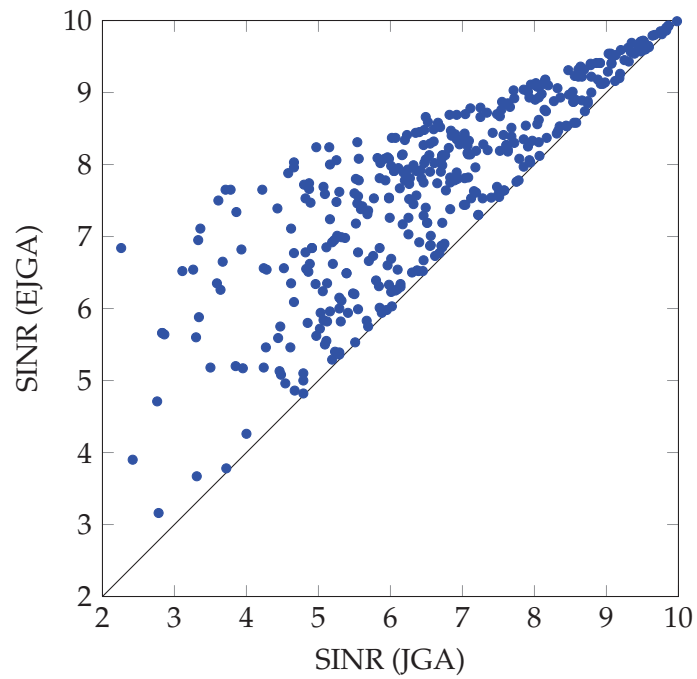


Figure 5.6: SINR (JGA) X SINR (EJGA) for suburban macrocell channels.

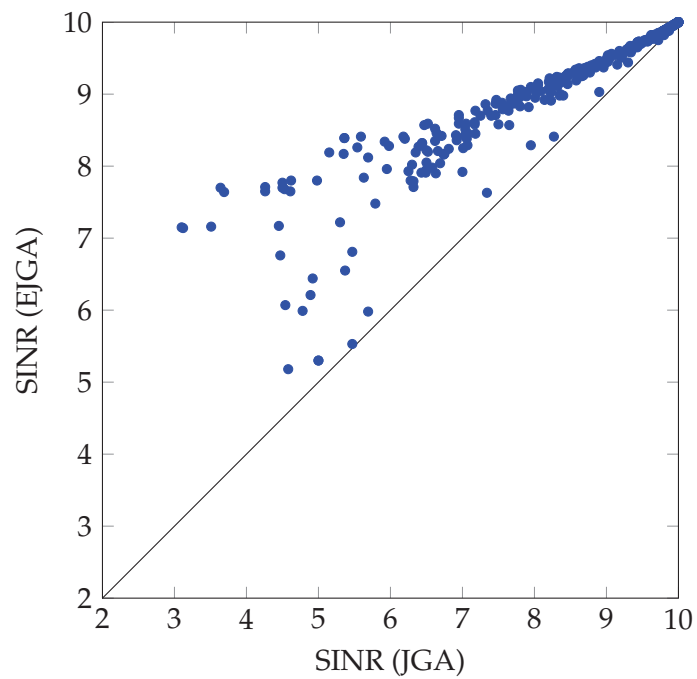


Figure 5.7: SINR (JGA) X SINR (EJGA) for urban macrocell channels.

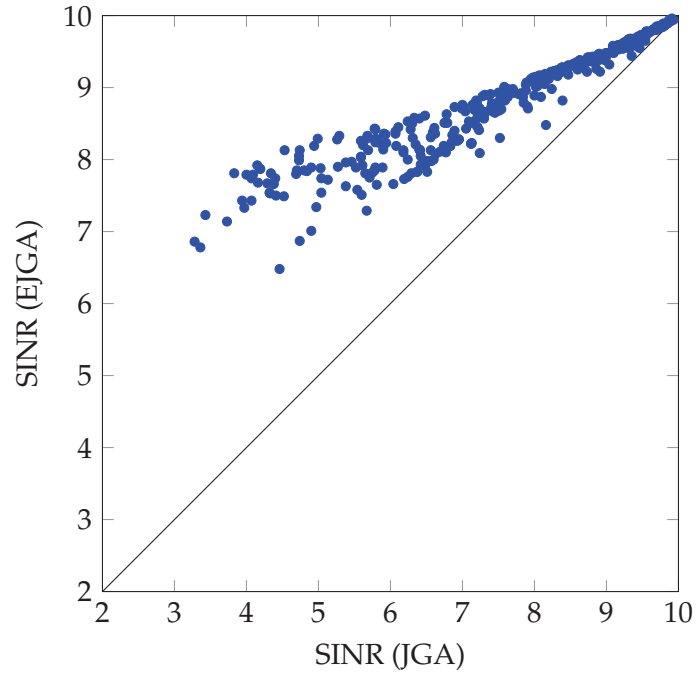


Figure 5.8: SINR (JGA) X SINR (EJGA) for urban microcell channels.

Table 5.1: Percentage of channels in Figures 5.6, 5.7, and 5.8 resulting in each CQI for suburban macrocells (SUMA), urban macrocells (UMA), and urban microcells (UMI), according to the HSDPA standard.

| CQI | SINR (dB) | # bits | SUMA | | UMA | | UMI | |
|---------------------------|--------------|--------|------|------|------|------|------|------|
| | | | JGA | EJGA | JGA | EJGA | JGA | EJGA |
| 0 | -2.8 < | 0 | 0% | 0% | 0% | 0% | 0% | 0% |
| 1 | -2.8 ↔ -2.4 | 137 | 0% | 0% | 0% | 0% | 0% | 0% |
| 2 | -2.4 ↔ -1.7 | 173 | 0% | 0% | 0% | 0% | 0% | 0% |
| 3 | -1.7 ↔ -0.7 | 233 | 0% | 0% | 0% | 0% | 0% | 0% |
| 4 | -0.7 ↔ -0.0 | 317 | 0% | 0% | 0% | 0% | 0% | 0% |
| 5 | -0.0 ↔ +0.8 | 377 | 0% | 0% | 0% | 0% | 0% | 0% |
| 6 | +0.8 ↔ +2.5 | 461 | 1% | 0% | 0% | 0% | 0% | 0% |
| 7 | +2.5 ↔ +3.7 | 650 | 4% | 0% | 1% | 0% | 1% | 0% |
| 8 | +3.7 ↔ +4.7 | 792 | 7% | 1% | 3% | 0% | 6% | 0% |
| 9 | +4.7 ↔ +6.7 | 931 | 40% | 1% | 12% | 0% | 22% | 0% |
| 10 | +6.7 ↔ +7.8 | 1262 | 20% | 21% | 12% | 4% | 18% | 9% |
| 11 | +7.8 ↔ +8.8 | 1483 | 15% | 23% | 16% | 17% | 20% | 33% |
| 12 | +8.8 ↔ +10.0 | 1742 | 12% | 22% | 56% | 75% | 33% | 58% |
| Average # bits per packet | | | 1150 | 1357 | 1504 | 1647 | 1358 | 1613 |

For the LTE standard (see Appendix C), CQIs are determined in order to ensure a frame error rate, FER, of at most 10%. Assuming the output of the detector to have a Gaussian distribution, and using the code rates specified by the standard, Table 5.2 was obtained for a frame size of 1024 bits.

Table 5.2: SNRs that result in a frame error rate of 10% for the turbo code specified by the LTE standard.

| CQI | 1 | 2 | 3 | 4 | 5 | 6 | 7 | 8 | 9 |
|-----------|------|------|------|------|------|-----|-----|-----|------|
| SINR (dB) | -7.5 | -6.5 | -4.5 | -2.0 | -1.0 | 2.5 | 5.5 | 7.0 | 10.0 |

Using once again the results shown in Figures 5.6, 5.7, and 5.8, together with Table 5.3, the throughput gain obtained by using the extended JGA approach as opposed to the regular JGA can be assessed. Gains of 9%, 5%, and 10% were obtained for suburban macrocells, urban macrocells, and urban microcells respectively for an SNR of 10 dB.

Table 5.3: Percentage of channels in Figures 5.6, 5.7, and 5.8 resulting in each CQI for suburban macrocells (SUMA), urban macrocells (UMA) and urban microcells (UMI), according to the LTE standard.

| CQI | SINR (dB) | # bits | SUMA | | UMA | | UMI | |
|----------------------------------|--------------|--------|-------|-------|-------|-------|-------|-------|
| | | | JGA | EJGA | JGA | EJGA | JGA | EJGA |
| 1 | < -7.5 | 0.000 | 0% | 0% | 0% | 0% | 0% | 0% |
| 2 | -7.5 ↔ -6.5 | 0.152 | 0% | 0% | 0% | 0% | 0% | 0% |
| 3 | -6.5 ↔ -4.5 | 0.234 | 0% | 0% | 0% | 0% | 0% | 0% |
| 4 | -4.5 ↔ -2.0 | 0.377 | 0% | 0% | 0% | 0% | 0% | 0% |
| 5 | -2.0 ↔ -1.0 | 0.602 | 0% | 0% | 0% | 0% | 0% | 0% |
| 6 | -1.0 ↔ +2.5 | 0.877 | 1% | 0% | 0% | 0% | 0% | 0% |
| 7 | +2.5 ↔ +5.5 | 1.176 | 26% | 6% | 8% | 1% | 12% | 0% |
| 8 | +5.5 ↔ +7.0 | 1.477 | 32% | 23% | 11% | 3% | 21% | 1% |
| 9 | +7.0 ↔ +10.0 | 1.914 | 41% | 70% | 81% | 96% | 67% | 99% |
| Avg. # bits per resource element | | | 1.571 | 1.721 | 1.810 | 1.892 | 1.733 | 1.910 |

5.4 SINR analysis - MIMO scenario

As in the SISO case, five hundred 2X2 MIMO normalized channels were generated according to the SCM model. A sampling rate of 1 MHz was used for a 2 GHz carrier frequency. Both transmitting and receiving antennas are half wavelength apart (15 cm). Again, the urban macrocell, suburban macrocell and urban microcell

scenarios are evaluated. Each channel is drawn as a point in Figures 5.9, 5.10, and 5.11, where one axis represents the SINR at the output of the detector for the JGA while the other represents the average SINR for extended JGA (EJGA) with one symbol removed from the interference pool. Each SINR was obtained for an SNR of 10 dB, and a QPSK modulation was used.

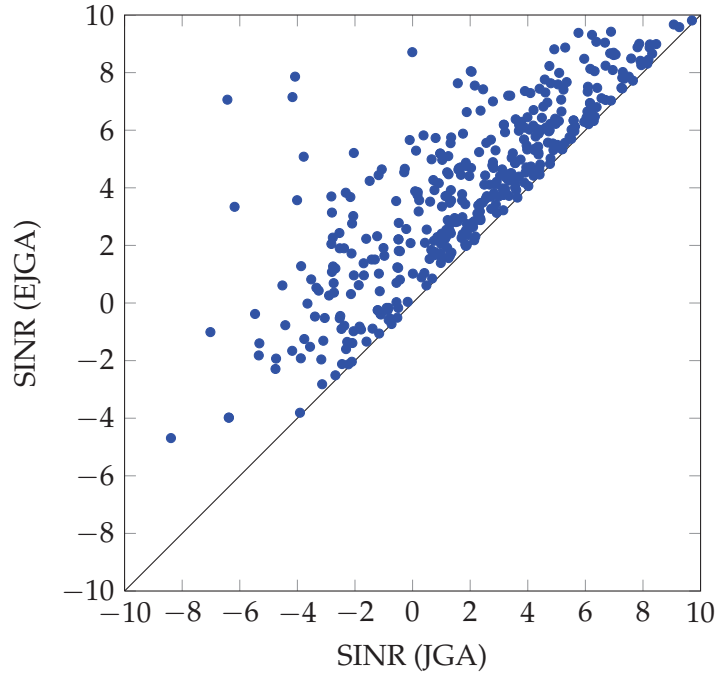


Figure 5.9: SINR (JGA) X SINR (EJGA) for 2X2 MIMO urban macrocell channels.

Applying the same techniques described previously for the SISO scenario, it is possible to calculate the average throughput gain obtained by using the extended JGA (removing the MAI), as opposed to the regular JGA for each MIMO scenario at an SNR of 10dB. For the HSDPA standard, applying the extended detection method results in throughput gains of 39%, 76% and 40%, for urban macro, suburban macro, and urban micro scenarios respectively.

For the LTE standard, the choice of modulation changes from QPSK to 16 QAM for CQIs greater than 6. Simulations showed that a QPSK modulation has a gain of 7 dB over a 16 QAM for the same channel. Hence, this change in the choice of modulation can be accounted by subtracting 7 dB of the SINR and using CQIs of 7, 8 and 9 on Table 5.2, as shown on Table 5.5. For the LTE standard, throughput gains of 25%, 45% and 22% were obtained for the urban macrocell, suburban macrocell

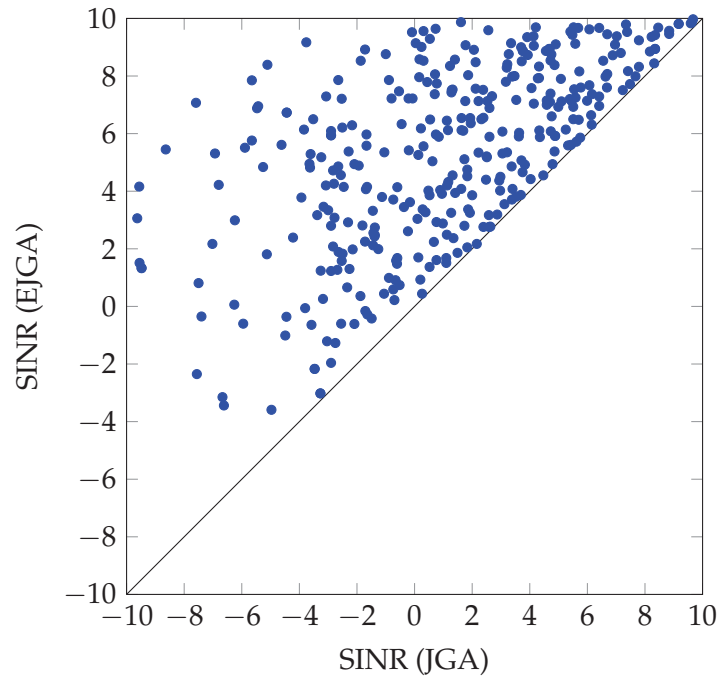


Figure 5.10: SINR (JGA) X SINR (EJGA) for 2X2 MIMO suburban macrocell channels.

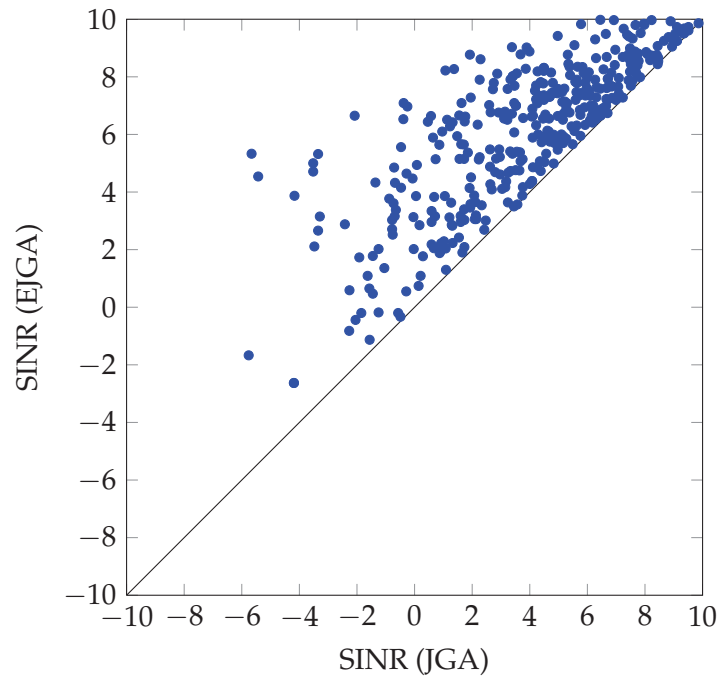


Figure 5.11: SINR (JGA) X SINR (EJGA) for 2X2 MIMO urban microcell channels.

Table 5.4: Percentage of channels in Figures 5.9, 5.10, and 5.11 resulting in each CQI for urban macrocells (UMA), suburban macrocells (SUMA), and urban microcells (UMI), according to the HSDPA standard.

| CQI | SINR (dB) | # bits | UMA | | SUMA | | UMI | |
|---------------------------|--------------|--------|-----|------|------|------|-----|------|
| | | | JGA | EJGA | JGA | EJGA | JGA | EJGA |
| 0 | -2.8 < | 0 | 9% | 1% | 17% | 2% | 3% | 0% |
| 1 | -2.8 ↔ -2.4 | 137 | 3% | 0% | 3% | 0% | 0% | 1% |
| 2 | -2.4 ↔ -1.7 | 173 | 5% | 2% | 4% | 1% | 2% | 0% |
| 3 | -1.7 ↔ -0.7 | 233 | 7% | 5% | 6% | 1% | 4% | 1% |
| 4 | -0.7 ↔ -0.0 | 317 | 5% | 5% | 4% | 3% | 4% | 1% |
| 5 | -0.0 ↔ +0.8 | 377 | 6% | 3% | 8% | 3% | 4% | 1% |
| 6 | +0.8 ↔ +2.5 | 461 | 20% | 15% | 13% | 11% | 14% | 6% |
| 7 | +2.5 ↔ +3.7 | 650 | 13% | 12% | 10% | 9% | 12% | 9% |
| 8 | +3.7 ↔ +4.7 | 792 | 10% | 15% | 8% | 10% | 12% | 7% |
| 9 | +4.7 ↔ +6.7 | 931 | 14% | 23% | 15% | 21% | 23% | 25% |
| 10 | +6.7 ↔ +7.8 | 1262 | 4% | 9% | 5% | 14% | 11% | 21% |
| 11 | +7.8 ↔ +8.8 | 1483 | 3% | 6% | 3% | 11% | 6% | 17% |
| 12 | +8.8 ↔ +10.0 | 1742 | 1% | 4% | 4% | 15% | 7% | 11% |
| Average # bits per packet | | | 567 | 790 | 569 | 1001 | 782 | 1094 |

and urban microcell scenarios, respectively.

Table 5.5: Percentage of channels in Figures 5.10, 5.9, and 5.11 resulting in each CQI for urban macrocells (UMA), suburban macrocells (SUMA), and urban microcells (UMI), according to the LTE standard.

| CQI | SINR (dB) | # bits | UMA | | SUMA | | UMI | |
|-------------------------------------|--------------|--------|-------|-------|-------|-------|-------|-------|
| | | | JGA | EJGA | JGA | EJGA | JGA | EJGA |
| 1 | < -7.5 | 0.000 | 0% | 0% | 2% | 0% | 0% | 0% |
| 2 | -7.5 ↔ -6.5 | 0.152 | 0% | 0% | 2% | 0% | 0% | 0% |
| 3 | -6.5 ↔ -4.5 | 0.234 | 3% | 0% | 3% | 1% | 1% | 0% |
| 4 | -4.5 ↔ -2.0 | 0.377 | 13% | 2% | 15% | 2% | 4% | 1% |
| 5 | -2.0 ↔ -1.0 | 0.602 | 6% | 4% | 6% | 1% | 3% | 1% |
| 6 | -1.0 ↔ +2.5 | 0.877 | 33% | 25% | 27% | 17% | 23% | 8% |
| 7 | +2.5 ↔ +5.5 | 1.176 | 30% | 36% | 24% | 27% | 33% | 26% |
| 8 | +5.5 ↔ +7.0 | 1.477 | 9% | 15% | 9% | 16% | 17% | 20% |
| 9 | +7.0 ↔ +10.0 | 1.914 | 6% | 17% | 11% | 36% | 20% | 44% |
| Average # bits per resource element | | | 0.981 | 1.230 | 0.973 | 1.416 | 1.251 | 1.532 |

5.5 EXIT charts - MIMO scenario

EXIT curves were obtained, using (4.24), for detectors applying the JGA and the extended JGA for five hundred channels generated for each one of the three possible SCM scenarios. These channels are the same as in last section. With these curves and the decoder curves for each CQI, shown in Figures 5.12 and 5.13, it is possible to determine the CQI as the higher one that still allows an “open-tunnel” between equalizer and decoder’s EXIT curves.

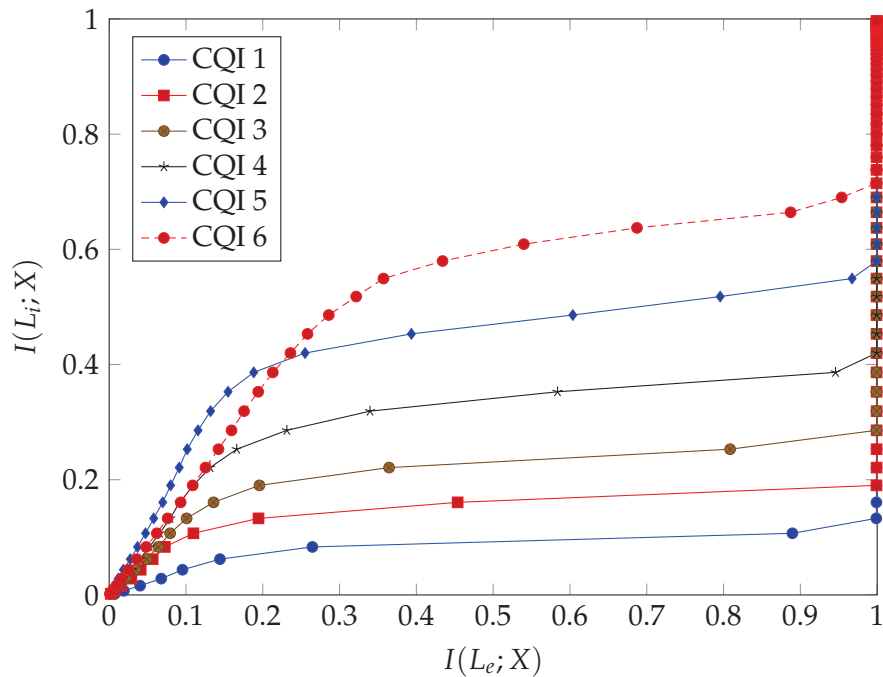


Figure 5.12: EXIT curves for LTE turbo decoders with CQIs 1-6.

In Figure 5.14, the percentage of channels per CQI (assuming the LTE standard), for iterative detectors applying the JGA and the extended JGA, for all three scenarios considered are compared. As expected, the use of the extended JGA concentrates more channels on higher CQIs, as opposed to the JGA, increasing the average overall throughput. Taking the results shown in this figure and the number of bits per resource element shown in Table C.2, the gain in throughput obtained by the extended JGA is of 22%, 37%, and 20% for the urban macrocell, suburban macrocell, and urban microcell scenarios, respectively.

In Figure 5.15, a comparison is made between the percentage of channels at each

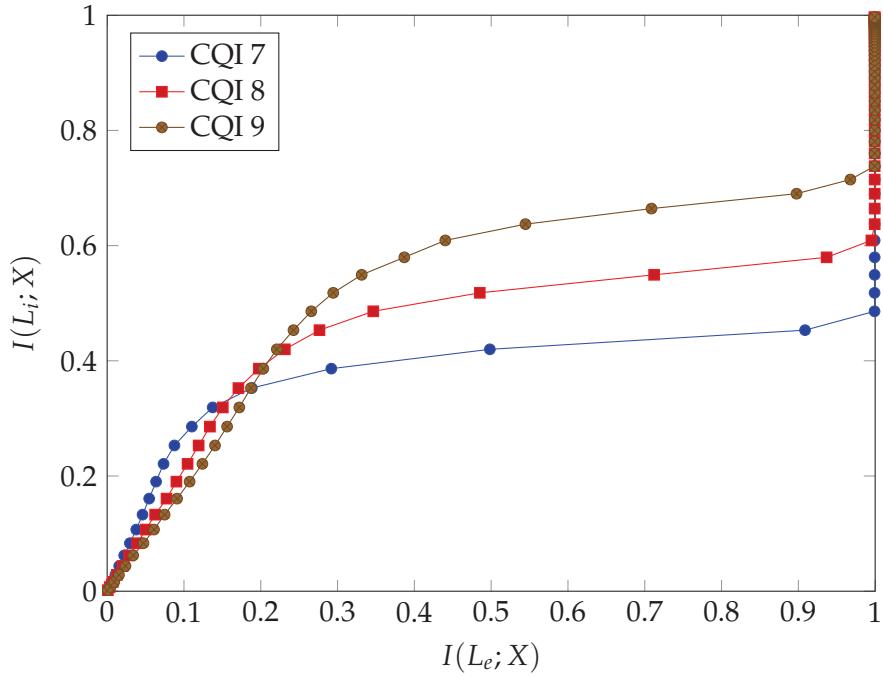


Figure 5.13: EXIT curves for LTE turbo decoders with CQIs 7, 8, and 9.

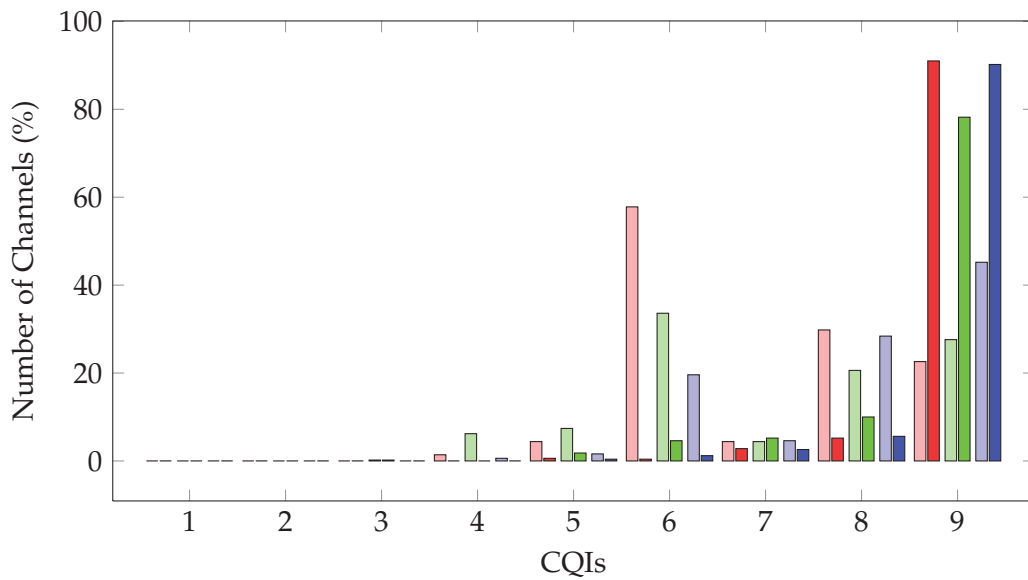


Figure 5.14: Percentage of channels per CQI for the iterative JGA (light colours) and iterative extended JGA (dark colours) for the urban macrocell (left, red), suburban macrocell (center, green), and urban microcell (right, blue) scenarios.

CQI for the non-iterative JGA and the iterative JGA for all three scenarios considered. Clearly, the use of an iterative system can lead to a significant throughput gain, as it concentrates more channels in high CQIs. Nominally, the gain in throughput obtained by making use of iterations is of 53%, 30%, and 23% for the urban macrocell, suburban macrocell, and urban microcell scenarios, respectively.

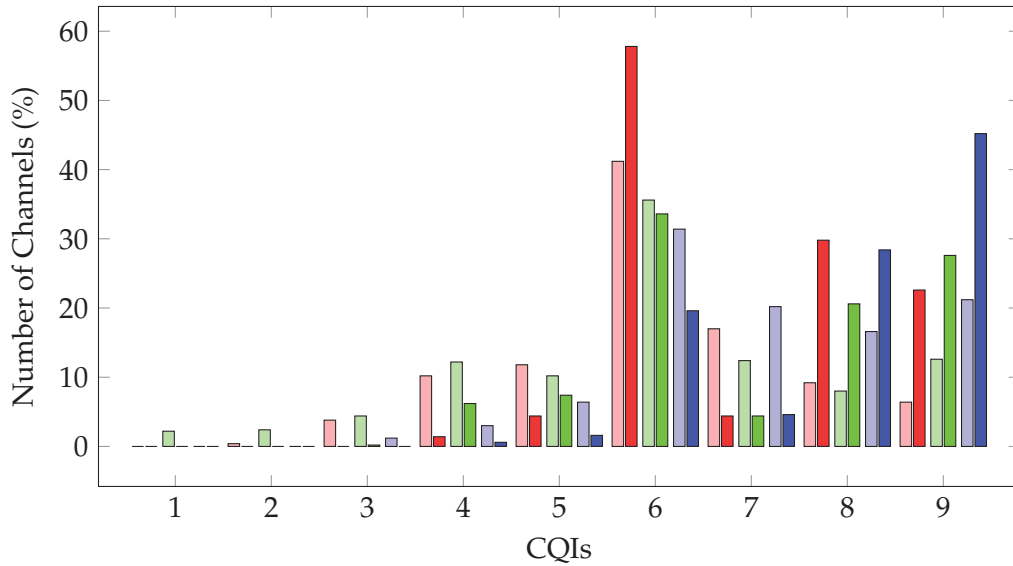


Figure 5.15: Percentage of channels per CQI for the non-iterative JGA (light colours) and iterative JGA (dark colours) for the urban macrocell (left, red), suburban macrocell (center, green), and urban microcell (right, blue) scenarios.

Finally, in Figure 5.16, the non-iterative JGA is compared to the iterative extended JGA. As expected, this comparison is the one providing the most significant gains in performance. Gains in average throughput of 86%, 79%, and 48% for the urban macrocell, suburban macrocell, and urban microcell scenarios, respectively, were obtained.

5.6 Comparing analysis and simulation results for a specific channel

In order to verify the accuracy of gains in performance predicted in previous sections using analysis methods, EXIT curves, as well as BER performance curves for a specific channel are presented here. These curves are for a 2×2 MIMO commu-

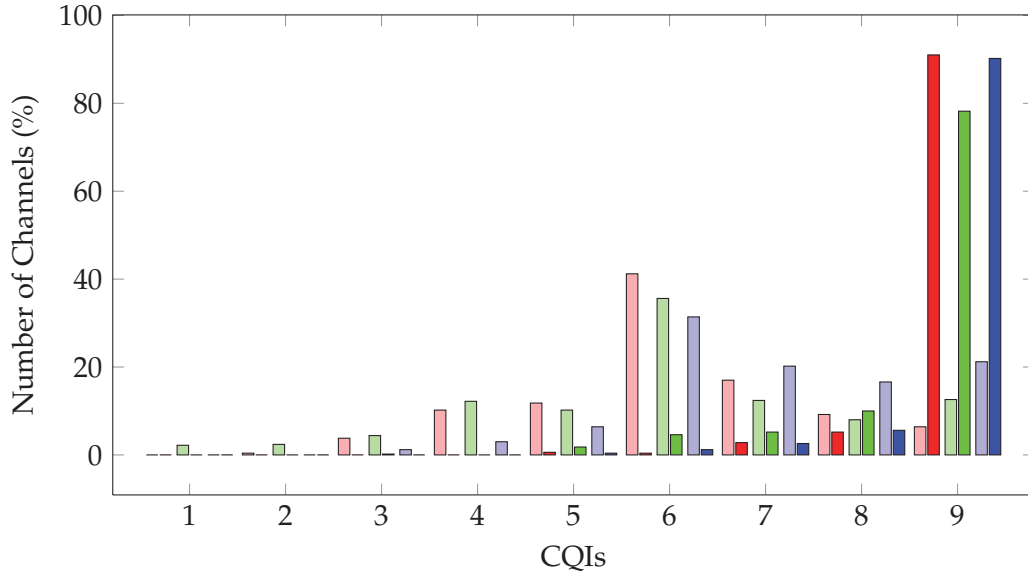


Figure 5.16: Percentage of channels per CQI for the non-iterative JGA (light colours) and iterative extended JGA (dark colours) for the urban macrocell (left, red), suburban macrocell (center, green), and urban microcell (right, blue) scenarios.

nication system depicted in Figure 5.17, and BER curves are obtained via Monte Carlo simulation.

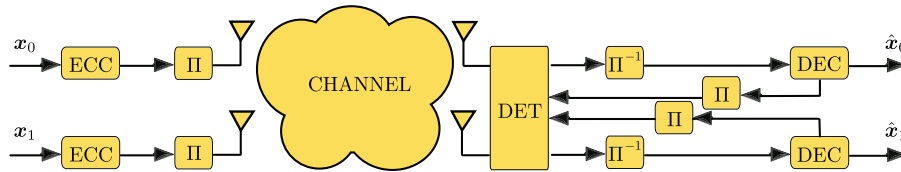


Figure 5.17: Schematics Diagram for a 2×2 MIMO multipath communication system.

The communication system shown in Figure 5.17 works as follows. Two vectors of data, x_0 and x_1 , are encoded by a turbo encoder as defined by the LTE standard [2] for a CQI of 6. After encoding, each stream is interleaved, modulated and transmitted over a normalized 2×2 MIMO multipath channel, generated according to the SCM model [62], whose coefficients are shown in Table 5.6. At the receiver, the detector samples the signal, at a rate of 10 MHz, and applies the JGA or extended JGA to obtain vectors with the LLRs for the transmitted coded bits for each stream. After de-interleaving, these vectors are fed to the decoders. Each decoder performs six

internal iterations and sends back extrinsic information about the encoded signals to the detector until a certain number of global iterations are completed. For this particular scenario, simulations showed that 2 iterations were already enough. Hard decisions on the decoded bits are only made at the final iteration to produce vectors of detected data \hat{x}_0 and \hat{x}_1 .

Table 5.6: Channel Coefficients

| Tx 1, Rx 1 | Tx 1, Rx 2 | Tx 2, Rx 1 | Tx 2, Rx 2 |
|-----------------|-----------------|-----------------|-----------------|
| $+0.23 - 0.29i$ | $-0.91 - 0.29i$ | $+0.40 + 0.06i$ | $-0.56 - 0.21i$ |
| $+0.09 - 0.12i$ | $-0.20 + 0.08i$ | $+0.12 + 0.03i$ | $-0.13 - 0.16i$ |
| $+0.04 + 0.05i$ | $+0.09 - 0.03i$ | $-0.05 - 0.01i$ | $+0.06 + 0.07i$ |
| $+0.03 - 0.03i$ | $-0.06 + 0.02i$ | $+0.03 + 0.00i$ | $-0.04 + 0.05i$ |
| $-0.02 + 0.02i$ | $+0.04 - 0.01i$ | $-0.02 + 0.00i$ | $+0.03 + 0.04i$ |
| $+0.01 - 0.02i$ | $-0.03 + 0.01i$ | $+0.02 + 0.00i$ | $-0.02 - 0.03i$ |

For this channel, EXIT curves are presented in Figure 5.18 for the extended JGA at 2 dB and the regular JGA at 8 dB. In this same figure, the EXIT curve for a turbo decoder for a CQI of 6. As it can be seen, for this particular channel, the EJGA has an open-tunnel at only 2 dB, while 8 dB are necessary for the regular JGA to assume convergence, leading to a 6 dB gain in performance.

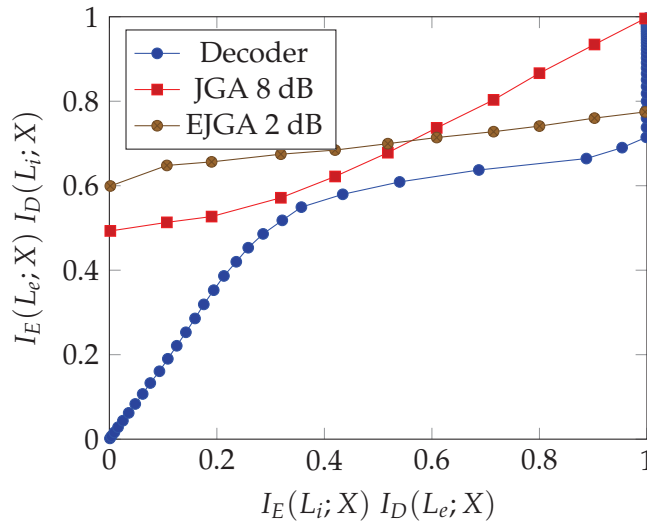


Figure 5.18: EXIT chart for the JGA, the extended JGA, and the decoder (inter-changed axis).

In Figure 5.19, BER curves for this system using the extended JGA and the classical JGA, are compared for the channel described in Table 5.6. Assuming perfect

channel knowledge at the receiver, the system applying the extended JGA outperforms the one applying the JGA by nearly 6 dB, as predicted for this channel. Also, as predicted, the system begins to converge to the proper solution at 2 dB for the extended JGA and at 8 dB for the regular JGA. Since the EXIT curve for a turbo decoder at a CQI of 6 is nearly parallel to the x-axis for most of the time, as shown in Figure 5.12, the gain in performance does not increase significantly with the number of iterations.

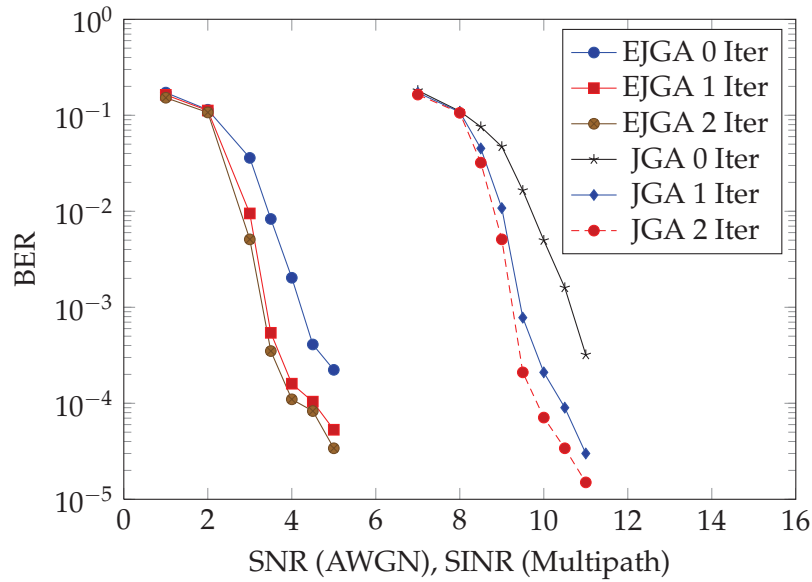


Figure 5.19: BER curves for iterative systems applying the JGA and the extended JGA for a channel specified by the coefficients in Table 5.6.

Clearly, this extreme improvement in performance is only obtained by a subset of channels for which most of the interference has been removed by the extended method. For channels where the overall interference is spread over many terms, the improvement in performance is less pronounced, as SINR charts presented in Chapter 4 suggest.

6

Conclusions and Future Work

In this work, a novel scheme for equalization of signals over multipath SISO or MIMO channels, denoted extended JGA, has been proposed. This method enhances the performance of equalizers based on the JGA by removing part of the MAI and/or ISI, prior to making use of the jointly Gaussian assumption to remove residual interference. Also, frequency-domain versions of both classical and extended JGA are presented, paving the way for the use of these methods in SC-FDMA transmissions.

Complexity analysis of classical JGA and extended JGA shows that the complexity of the latter is only substantially greater than the former for large number of symbols removed from the interference pool. Moreover, a close look at the schematics diagrams in Section 3.7 shows that the additional computations required by the extended method can be performed in a parallel fashion. Hence, depending on the hardware available, the extended method may not even require additional clock cycles.

The gain in performance obtained using the extended JGA, instead of the classical JGA, is assessed by means of SINR analysis for non-iterative schemes. It is shown that, for SISO scenarios, the extended method can lead to noticeable gains in throughput. For communication systems using the LTE standard, average gains of 5%, 9%, and 10% in throughput were observed for suburban macrocell, urban macrocell and urban microcell scenarios generated according to the SCM. For 2×2 multipath MIMO systems, assuming antennas both at the transmitter and receiver

to be separated by only half wavelength, even larger gains were obtained. Nominally, average gains in throughput of 45%, 25%, and 22% were obtained for suburban macrocell, urban macrocell and urban microcell scenarios.

For iterative equalization schemes, EXIT charts are used to verify the improvement in performance obtained by the extended JGA over the classical JGA. Used in conjunction with the SINR method, it was possible to use EXIT charts to verify gains in performance and/or throughput for hundreds of channels generated according to the SCM. According to the analysis performed in this work, average gains of more than 35%, 22%, and 20% were obtained for 2×2 multipath MIMO channels generated according to the SCM for suburban macrocell, urban macrocell and urban microcell scenarios, respectively.

A Simulink[®] model of a communication system over MIMO multipath channels with iterative equalization at the receiver was created. Performing Monte Carlo simulations with this model, it was possible to verify the gain in performance predicted by SINR and EXIT chart analysis for specific channels.

6.1 Original contributions

A number of original contributions to the field of signal processing for wireless communications is proposed in this work. The most significant ones are listed in what follows.

Extended JGA An extension of the jointly Gaussian approach for equalization of signals received over multipath channels was proposed. This extension generalizes JGA equalizers allowing a trade-off between complexity and performance. This idea was first presented in [63];

Extended JGA for multipath MIMO channels The idea of extending the JGA was first generalized for MIMO multipath channels in [64] and a more comprehensive treatment of this topic, including SINR and EXIT chart analysis, is presented in [65];

JGA in frequency domain In [66], the JGA, and consequently the extended JGA, are adapted to work in the frequency domain. Working in the frequency domain has the advantage that the channel matrix is diagonalized, simplifying the equalization process. This adaptation makes this equalization scheme

specially well-suited to be applied in SC-FDMA transmissions, as proposed in the LTE standard for the uplink scenario [2].

6.2 Future work

The extended JGA method for equalization presented here was only analyzed and simulated in this work for a fixed channel found in literature (test channel A) and 2×2 MIMO channels generated according to the SCM model. Nevertheless, this model can be applied to any wireless MIMO multipath channel with an arbitrary number of antennas, transmissions over optical and copper cables, and even underwater acoustic communications. The methods presented here only require the communication channel to be described in discrete-time baseband form according to (2.1) or (2.2).

In Chapter 3, schematic diagrams of the JGA and the extended JGA are shown. These diagrams were used to produce Simulink[®] models for both methods which, in turn, were used in Monte Carlo simulations. For Xilinx[®] Field-Programmable Gate Array (FPGA) boards, these models can be rewritten using components available in the System Generator Blockset and readily compiled into hardware language. Implementing the proposed methods in FPGA has two advantages. First, it can take advantage of the parallel nature of the proposed methods, making the equalization process much faster and permitting lower BER regions to be analyzed. Second, it permits an accurate idea of the memory and hardware requirements for implementing such methods, which are of fundamental importance to analyze the feasibility of such methods for practical communications systems.

Bibliography

- [1] H. Holma and A. Toskala, *HSDPA/HSUPA for UMTS, High Speed Radio Access for Mobile Communications*. John Wiley and Sons, 2006.
- [2] 3rd Generation Partnership Project (3GPP), "Physical layer aspects for evolved UTRA (TR 25.814 version 1.5.0 (Release 7))," *Tech. Rep., 3rd Generation Partnership Project (3GPP)*, 2006.
- [3] J. G. Andrews, A. Ghosh, and R. Muhamed, *Fundamentals of WiMAX: Understanding Broadband Wireless Networks*. Prentice Hall, 2003.
- [4] J. Proakis, *Digital Communications, 3rd Edition*. McGraw-Hill, 1995.
- [5] C. E. Shannon, "A mathematical theory of communication," *The Bell system technical journal*, vol. 27, pp. 379–423, 1948.
- [6] A. Goldsmith, *Wireless Communications*. Cambridge, 2005.
- [7] R. Price, "Nonlinearly feedback-equalized PAM vs. capacity," *Proc. of IEEE International Conference on Communications*, pp. 22.12–22.17, 1972.
- [8] A. J. Viterbi, "Error bounds for convolutional codes and an asymptotically optimum decoding algorithm," *IEEE Transactions on Information Theory*, vol. 13, pp. 260–269, 1967.
- [9] L. Bahl, J. Cocke, F. Jelinek, and J. Raviv, "Optimal decoding of linear codes for minimizing symbol error rate," *IEEE Transactions on Information Theory*, pp. 284–287, 1974.
- [10] S. Lin and D. J. Costello, *Error Control Coding, 2nd Edition*. Prentice Hall, 2004.
- [11] A. Duel-Hallen and C. D. Heegard, "Delayed decision feedback sequence estimation," *IEEE Transactions on Communications*, vol. 37, pp. 428–436, 1989.
- [12] M. V. Eyuboglu and S. U. H. Qureshi, "Reduced-state sequence estimation with set partitioning and decision feedback," *IEEE Transactions on Communications*, vol. 36, pp. 13–20, 1988.

- [13] V. Franz and J. B. Anderson, "Concatenated decoding with a reduced-search BCJR algorithm," *IEEE Journal on Selected Areas in Communications*, vol. 16, pp. 186–195, 1998.
- [14] D. Ferttonani, A. Barbieri, and G. Colavolpe, "Reduced-complexity BCJR algorithm for turbo equalization," *IEEE Transactions on Communications*, vol. 55, pp. 2279–2287, 2007.
- [15] G. J. Foschini and M. J. Gans, "On limits of wireless communications in a fading environment when using multiple antennas," *Wireless Personal Communications*, vol. 6, pp. 311–335, 1998.
- [16] E. Biglieri, R. Calderbank, A. Constantinides, A. Goldsmith, A. Paulraj, and H. V. Poor, *MIMO Wireless Communications*. Cambridge University Press, 2007.
- [17] A. Paulraj, R. Nabar, and D. Gore, *Introduction to Space-Time Wireless Communications*. Cambridge Press, 2003.
- [18] E. Biglieri, G. Taricco, and A. Tulino, "Performance of space-time codes for a large number of antennas," *IEEE Transactions on Information Theory*, 2002.
- [19] G. Strang, *Linear Algebra and Its Applications, 4th Edition*. Brooks Cole, 2006.
- [20] P. W. Wolniansky, G. J. Foschini, G. D. Golden, and R. A. Valenzuela, "V-BLAST: an architecture for realizing very high data rates over the rich-scattering wireless channel," *Proceedings of the International Symposium on Signals, Systems, and Electronics*, pp. 295–300, 1998.
- [21] H. Holma and A. Toskala, *LTE for UMTS - OFDMA and SC-FDMA Based Radio Access*. John Wiley and Sons, 2009.
- [22] C. Berrou, A. Glavieux, and P. Thitimajshima, "Near shannon limit error-correcting coding and decoding: Turbo-codes," *Proc. of IEEE International Conference on Communications 1993*, vol. 2, pp. 1064–1070, 1993.
- [23] C. Douillard, A. Picard, P. Didier, M. Jézéquel, C. Berrou, and A. Glavieux, "Iterative correction of intersymbol interference : Turbo-equalization," *European Transactions on Telecommunications*, vol. 6, pp. 507–511, 1995.
- [24] J. Hagenauer and P. Hoeher, "A Viterbi algorithm with soft-decision outputs and its applications," *Proc. GLOBECOM*, pp. 47.11–47.17, 1989.

- [25] G. Bauch, H. Khorram, and J. Hagenauer, "Iterative equalization and decoding in mobile communications systems," *Proc. 2nd European Personal Mobile Communications Conference*, pp. 307–312, 1997.
- [26] A. Berthet, R. Visoz, and P. Tortelier, "Turbo-equalization for coded 8-PSK signals over ISI channels with application to EDGE advanced mobile system," *Proc. IEEE International Symposium on Personal, Indoor and Mobile Radio Communications*, pp. 307–312, 2000.
- [27] R. Visoz, A. O. Berthet, and S. Chtourou, "A novel frequency domain turbo-equalizer for ST-BICM over MIMO ISI channel," *Proceedings of the 6th IEEE International Conference on 3G and Beyond*, pp. 185–189, 2005.
- [28] X. Wang and H. V. Poor, "Iterative (turbo) soft interference cancellation and decoding for coded CDMA," *IEEE Transactions on Communications*, vol. 47, pp. 1670–1678, 1999.
- [29] M. Tuchler, R. Koetter, and A. C. Singer, "Minimum mean squared error equalization using *a priori* information," *IEEE Transactions on Signal Processing*, vol. 50, pp. 673–683, 2002.
- [30] J. C. Fricke, M. Sandell, J. Mietzner, and P. A. Hoeher, "Impact of the Gaussian approximation on the performance of the probabilistic data association MIMO decoder," *EURASIP Journal on Wireless Communications and Networking*, pp. 796–800, 2005.
- [31] T. H. Peng and L. K. Rasmussen, "Asymptotically optimal nonlinear MMSE multiuser detection based on multivariate Gaussian approximation," *IEEE Transactions on Communications*, vol. 54, pp. 1427–1438, 2006.
- [32] X. Yuan, K. Wu, and L. Ping, "The jointly Gaussian approach to iterative detection in MIMO systems," *IEEE International Conference on Communications*, pp. 2935–2940, 2006.
- [33] L. Liu, W. K. Leung, and L. Ping, "Simple iterative chip-by-chip multiuser detection for CDMA systems," *IEEE Vehicular Technology Conference*, pp. 2157–2161, 2003.
- [34] X. Yuan, K. Wu, and L. Ping, "Low-complexity iterative detection in multi-user MIMO ISI channels," *IEEE Signal Processing Letters*, pp. 25–28, 2008.

- [35] T. Wo and P. A. Hoeher, "Low-complexity Gaussian detection for MIMO systems," *Hindawi Journal of Electrical and Computer Engineering*, 2010.
- [36] D. Tse and P. Viswanath, *Fundamentals of Wireless Communications*. Cambridge Press, 2005.
- [37] G. L. Turin, F. D. Clapp, T. L. Johnston, S. B. Fine, and D. Lavry, "A statistical model of urban multipath propagation," *IEEE Transactions on Vehicular Technology*, vol. 21, pp. 1–9, 1972.
- [38] H. Suzuki, "A statistical model for urban radio propagation," *Doctoral Thesis, University of California Berkeley*, 1975.
- [39] —, "A statistical model for urban radio propagation," *IEEE Transactions on Communications*, vol. 25, pp. 673–680, 1977.
- [40] A. A. Saleh and R. A. Valenzuela, "A statistical model for indoor multipath propagation," *IEEE Journal on Selected Areas in Communications*, vol. 5, 1987.
- [41] I. E. Telatar, "Capacity of multi-antenna Gaussian channels," *European Transactions on Telecommunications*, pp. 585–595, 1999.
- [42] D. S. Shiu, G. Foschini, M. J. Gans, and J. M. Khan, "Fading correlation and its effect on the capacity of multielement antenna systems," *IEEE Transactions on Communications*, vol. 48, 2000.
- [43] C. Xiao, J. Wu, S.-Y. Leong, Y. R. Zheng, and K. B. Letaief, "A discrete-time model for spatio-temporally correlated MIMO WSSUS multipath channels," *Proceedings of Wireless Communications and Networking Conference*, vol. 1, 2003.
- [44] N. Costa and S. Haykin, "A novel wideband MIMO channel model and experimental validation," *IEEE Transactions on Antennas and Propagation*, pp. 550–562, 2008.
- [45] C. Zhang and R. R. Bitmead, "State-space modelling for MIMO wireless channels," *Proceedings of the IEEE International Conference on Communications*, 2005.
- [46] K. Pedersen, J. Andersen, J. Kermoal, and P. Mogensen, "A stochastic multiple-input-multiple-output radio channel model for evaluation of space-time coding algorithms," *Proceedings of IEEE 52nd Vehicular Technology Conference (VTC 2000)*, pp. 893–897, 2000.

- [47] J. P. Kermoal, L. Schumacher, K. I. Pedersen, P. E. Mogensen, and F. Frederiksen, "A stochastic MIMO radio channel model with experimental validation," *IEEE Journal on Selected Areas in Communications*, vol. 20, pp. 1211–1226, 2002.
- [48] 3rd Generation Partnership Project (3GPP), "Spatial channel model for multiple input multiple output (MIMO) simulations (TR 25.996 v6.1.0 (Release 6)),", 2003.
- [49] E. Damosso and L. M. Correia, "Cost 231 final report," *European Commission*, 1999.
- [50] M. C. Jeruchim, P. Balaban, and K. S. Shanmugan, *Simulation of Communication Systems*. Kluwer Academic, 2000.
- [51] S. Loyka and G. Levin, "On physically-based normalization of MIMO channel matrices," *IEEE Transactions on Wireless Communications*, vol. 8, no. 3, pp. 1107–1112, 2009.
- [52] A. G. Burr, "Capacity bounds and estimates for the finite scatteres MIMO wireless channel," *IEEE Journal on Selected Areas in Communications*, pp. 812–818, 2003.
- [53] A. Papoulis and S. U. Pillai, *Probability, Random Variables and Stochastic Processes*. McGraw-Hill, 2002.
- [54] M. Tuchler, R. Koetter, and A. C. Singer, "Turbo equalization: Principles and new results," *IEEE Transactions on Communications*, vol. 50, pp. 754–767, 2002.
- [55] W. H. Press, B. P. Flannery, S. A. Teukolsky, and W. T. Vetterling, *Numerical Recipes: The Art of Scientific Computing*. Cambridge University Press, 1986.
- [56] J. R. Barry, E. A. Lee, and D. G. Messerschmitt, *Digital Communications*. Springer, 2003.
- [57] S. ten Brink, "Convergence behavior of iteratively decoded parallel concatenated codes," *Electronics Letters*, vol. 35, pp. 1117–1119, 1999.
- [58] —, "Convergence of iterative decoding," *IEEE Transactions on Communications*, vol. 49, pp. 1727–1737, 2001.
- [59] C. Schlegel and L. Perez, *Trellis and Turbo Coding*. Wiley-IEEE Press, 2003.
- [60] T. M. Cover and J. A. Thomas, *Elements of Information Theory, 2nd Edition*. Wiley-Interscience, 2006.

- [61] Motorola and Nokia, "R1-02-0675, Revised CQI proposal," *3GPP RAN WG1, Tech. Rep.*, 2002.
- [62] 3GPP, "Spatial channel model for multiple-input multiple-output (MIMO) simulations," vol. TR 25.996 V6.1.0, 2003.
- [63] M. Jar and C. Schlegel, "Extended jointly Gaussian approach for iterative equalization," *IEEE International Conference on Communications*, 2010.
- [64] —, "Extended jointly gaussian approach for MIMO multipath channels," *Proceedings of the International Symposium on Turbo Codes and Iterative Information Processing (ISTC)*, 2010.
- [65] —, "Detection of signals over multipath channels using an extended jointly Gaussian approach," *Submitted to IEEE Transactions on Wireless Communications*, 2011.
- [66] M. Jar, E. Bouton, and C. Schlegel, "Frequency domain iterative equalization for single-carrier FDMA," *Proceedings of the International Workshop on Signal Processing Advances in Wireless Communications (SPAWC)*, 2011.
- [67] "EDGE, HSPA, LTE: The mobile broadband advantage," *Rysavy Research*, 2007.
- [68] 3rd Generation Partnership Project (3GPP), "Universal mobile telecommunications systems (UMTS); multiplexing and channel coding (FDD) (Release 5) TS 25.212." *Tech. Rep., 3rd Generation Partnership Project (3GPP)*, 2006.
- [69] S. Crozier and P. Guinand, "High-performance low-memory interleaver banks for turbo codes," *Proceedings of IEEE 54rd Vehicular Technology Conference*, 2001.
- [70] P. Frenger, S. Parkvall, and E. Dahlman, "Performance comparison of HARQ with Chase combining and incremental redundancy for HSDPA," *IEEE Vehicular Technology Conference, Fall*, 2001.
- [71] K. Freudenthaler, F. Kaltenberger, S. Geirhofer, S. Paul, J. Wehinger, C. Mecklenbräuker, A. Springer, and J. Berkmann, "Throughput simulations for a UMTS high speed downlink packet access LMMSE equalizer," *Proc. IST Mobile Summit*, 2005.
- [72] C. Dumard, F. Kaltenberger, , and K. Freudenthaler, "Low-cost approximate LMMSE equalizer based on Krylov subspace methods for HSDPA," *IEEE Transactions on Wireless Communications*, vol. 6, 2007.

-
- [73] 3rd Generation Partnership Project (3GPP), "Evolved universal terrestrial radio access (E-UTRA): Multiplexing and channel coding (TS 36.212 v9.1.0 (Release 9))," *Tech. Rep., 3rd Generation Partnership Project (3GPP)*, 2010.
- [74] —, "Evolved universal terrestrial radio access (E-UTRA): Physical layer procedures (TS 36.213 v9.1.0 (Release 9))," 2010.

A

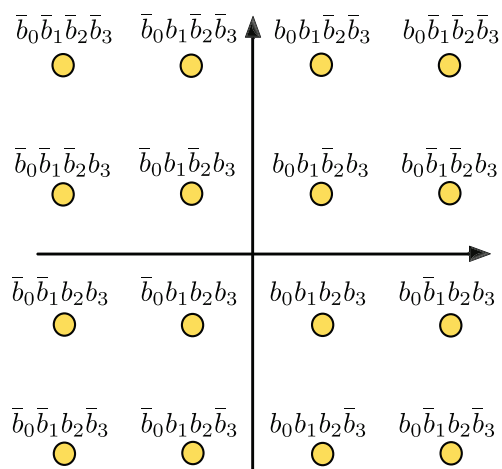
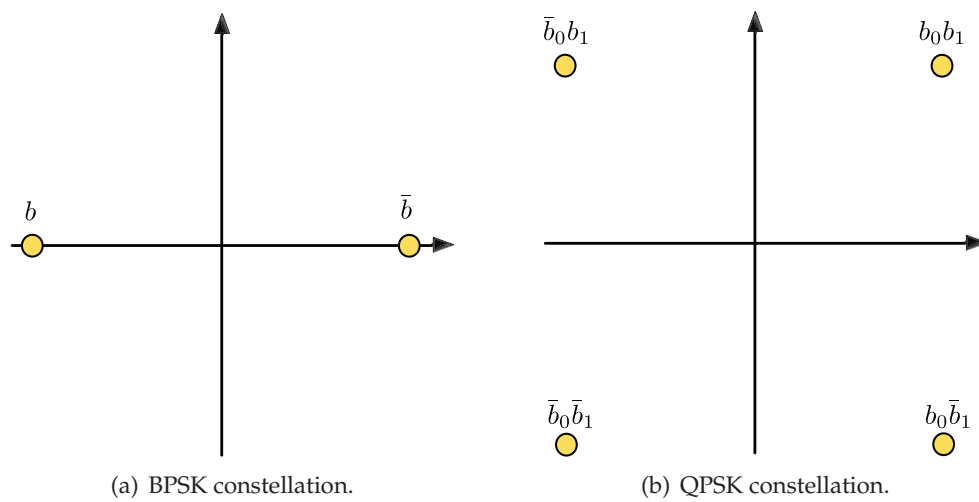
Obtaining Soft-Values from LLRs

In iterative detectors, both the JGA, as well as the extended JGA, need to make use of *a priori* information to obtain the mean value of each transmitted symbol, $\bar{x}[k] = \mathbb{E}\{x[k]\}$, as well as its variance, $v[k] = \mathbb{E}\{(x[k] - \bar{x}[k])(x[k]^\dagger - \bar{x}[k]^\dagger)\}$. However, the *a priori* information fed back from the decoder is the log-likelihood ratio (LLR) for each transmitted bit, as opposed to information for each transmitted symbol.

In a discrete baseband representation of a digital communication system, the complex symbols to be transmitted are simple bijective mappings of vectors of binary numbers, i.e., the task of the modulator is to map binary vectors into points in the complex plane. In Figure A.1 the constellations for binary phase-shift keying (BPSK), quadrature phase-shift keying (QPSK) and 16 quadrature amplitude modulation (16 QAM) schemes are shown. To simplify notation, in Figure A, $b_i[k] = 1$, i.e., the i th bit that takes part in the mapping of symbol $x[k]$ being equal to one, is represented by b_i . In the same way, $b_i[k] = 0$ is represented by \bar{b}_i .

To obtain the mean and variance of the transmitted symbols, for each signal constellation, it is first necessary to obtain an expression for the probabilities of a given bit $b[k]$ being equal to zero or one, i.e., $P(b[k] = 1)$ and $P(b[k] = 0)$, from the LLRs. Using the definition of log-likelihood ratios,

$$L[k] \triangleq \log \left[\frac{P(b[k] = 1)}{P(b[k] = 0)} \right], \quad (\text{A.1})$$



(c) 16 QAM constellation.

Figure A.1: Constellation mappings.

and the identity

$$P(b[k] = 1) = 1 - P(b[k] = 0), \quad (\text{A.2})$$

these probabilities can be obtained as

$$P(b[k] = 1) = \frac{e^{L[k]}}{1 + e^{L[k]}} \quad (\text{A.3}) \quad P(b[k] = 0) = \frac{1}{1 + e^{L[k]}}. \quad (\text{A.4})$$

For modulation orders $m > 1$, each transmitted symbol is a function of m bits, i.e., $x[k] = f(b_0[k], b_1[k], \dots, b_m[k])$. Therefore, each symbol $x[k]$ has m LLRs, denoted by $L_0[k], L_1[k], \dots, L_m[k]$, associated to it.

The mean values and the variances of the transmitted symbols will depend on these probabilities, as well as on the the signal constellation used. In this appendix, it is shown how to calculate the mean value and the variance of signals transmitted using BPSK, QPSK, and 16 QAM constellations using Gray coding, given a set of LLRs.

A.1 BPSK constellation

Assuming the mapping shown in Figure A.1(a), it is easy to show that the mean value of a transmitted symbol $x[k]$ is given by

$$\begin{aligned} \bar{x}[k] &= \mathbb{E}\{x[k]\} = -P(b[k] = 1) + P(b[k] = 0) \\ &= -\frac{e^{L[k]}}{1 + e^{L[k]}} + \frac{1}{1 + e^{L[k]}} \\ &= -\frac{e^{L[k]/2} - e^{-L[k]/2}}{e^{L[k]/2} + e^{-L[k]/2}} = -\tanh(L[k]/2), \end{aligned} \quad (\text{A.5})$$

and the variance by

$$\begin{aligned} v[k] &= \mathbb{E}\{(x[k] - \bar{x}[k])(x[k]^\dagger - \bar{x}[k]^\dagger)\} \\ &= \mathbb{E}\{|x[k]|^2\} - \bar{x}[k]\mathbb{E}\{x[k]^\dagger\} - \bar{x}[k]^\dagger\mathbb{E}\{x[k]\} + \bar{x}[k]^2 \\ &= 1 - |\bar{x}[k]|^2, \end{aligned} \quad (\text{A.6})$$

where the last equality holds for all constellations for which $\mathbb{E}\{|x[k]|^2\} = 1$. In other words, independent of the constellation used, (A.6) can be used as long as

the signal's power is always unitary. For instance, this expression can be used for any phase shift-keying modulations, independent of the size of the constellation.

A.2 QPSK constellation

Assuming the mapping shown in Figure A.1(b), where $b_0b_1 = 1/\sqrt{2} + i/\sqrt{2}$, it can be shown that

$$\begin{aligned}\bar{x}[k] &= \left(\frac{-1-i}{\sqrt{2}}\right) P(b_0[k]=0)P(b_1[k]=0) + \left(\frac{-1+i}{\sqrt{2}}\right) P(b_0[k]=0)P(b_1[k]=1) \\ &\quad + \left(\frac{1-i}{\sqrt{2}}\right) P(b_0[k]=1)P(b_1[k]=0) + \left(\frac{1+i}{\sqrt{2}}\right) P(b_0[k]=1)P(b_1[k]=1).\end{aligned}\tag{A.7}$$

Dividing this expression in its real and imaginary parts,

$$\begin{aligned}Re\{\bar{x}[k]\} &= -\frac{1}{\sqrt{2}}P(b_0[k]=0)P(b_1[k]=0) - \frac{1}{\sqrt{2}}P(b_0[k]=0)P(b_1[k]=1) \\ &\quad + \frac{1}{\sqrt{2}}P(b_0[k]=1)P(b_1[k]=0) + \frac{1}{\sqrt{2}}P(b_0[k]=1)P(b_1[k]=1) \\ &= \frac{-1}{\sqrt{2}}P(b_0[k]=0) + \frac{1}{\sqrt{2}}P(b_0[k]=1) \\ &= \frac{1}{\sqrt{2}} \left(\frac{e^{L_0[k]}}{1+e^{L_0[k]}} - \frac{1}{1+e^{L_0[k]}} \right) \\ &= \frac{1}{\sqrt{2}} \tanh(L_0[k]/2),\end{aligned}\tag{A.8}$$

$$\begin{aligned}Im\{\bar{x}[k]\} &= -\frac{1}{\sqrt{2}}P(b_0[k]=0)P(b_1[k]=0) + \frac{1}{\sqrt{2}}P(b_0[k]=0)P(b_1[k]=1) \\ &\quad - \frac{1}{\sqrt{2}}P(b_0[k]=1)P(b_1[k]=0) + \frac{1}{\sqrt{2}}P(b_0[k]=1)P(b_1[k]=1) \\ &= \frac{-1}{\sqrt{2}}P(b_1[k]=0) + \frac{1}{\sqrt{2}}P(b_1[k]=1) \\ &= \frac{1}{\sqrt{2}} \left(\frac{e^{L_1[k]}}{1+e^{L_1[k]}} - \frac{1}{1+e^{L_1[k]}} \right) \\ &= \frac{1}{\sqrt{2}} \tanh(L_1[k]/2).\end{aligned}\tag{A.9}$$

Hence, the the mean value of a transmitted symbol $x[k]$ is given by

$$\bar{x}[k] = \mathbb{E}\{x[k]\} = \frac{1}{\sqrt{2}} (\tanh(L_0[k]/2) + \tanh(L_1[k]/2)i), \quad (\text{A.10})$$

and its variance is calculated according to (A.6).

A.3 16 QAM constellation

Assuming the mapping shown in Figure A.1(c), where $b_0b_1\bar{b}_2b_3 = 1/\sqrt{10} + i/\sqrt{10}$, the same procedure shown for BPSK and QPSK modulations can be applied, resulting in

$$\text{Re}\{\bar{x}[k]\} = \frac{3}{\sqrt{10}} \frac{e^{L_0[k]} - 1}{1 + e^{L_0[k]}} \frac{1}{1 + e^{L_1[k]}} + \frac{1}{\sqrt{10}} \frac{e^{L_0[k]} - 1}{1 + e^{L_0[k]}} \frac{e^{L_1[k]}}{1 + e^{L_1[k]}} \quad (\text{A.11})$$

$$\text{Im}\{\bar{x}[k]\} = \frac{3}{\sqrt{10}} \frac{1 - e^{L_2[k]}}{1 + e^{L_2[k]}} \frac{1}{1 + e^{L_3[k]}} + \frac{1}{\sqrt{10}} \frac{1 - e^{L_2[k]}}{1 + e^{L_2[k]}} \frac{e^{L_3[k]}}{1 + e^{L_3[k]}}. \quad (\text{A.12})$$

Hence, the mean value of a transmitted symbol $x[k]$ is given by

$$\begin{aligned} \bar{x}[k] &= \frac{3}{\sqrt{10}} \frac{\tanh(L_0[k]/2)}{1 + e^{L_1[k]}} + \frac{1}{\sqrt{10}} \frac{\tanh(L_0[k]/2)e^{L_1[k]}}{1 + e^{L_1[k]}} \\ &\quad - \left(\frac{3}{\sqrt{10}} \frac{\tanh(L_2[k]/2)}{1 + e^{L_3[k]}} + \frac{1}{\sqrt{10}} \frac{\tanh(L_2[k]/2)e^{L_3[k]}}{1 + e^{L_3[k]}} \right) i. \end{aligned} \quad (\text{A.13})$$

Since not all points in the constellation have the same energy, the variance of the transmitted symbols cannot be calculated as in the BPSK or QPSK cases.

According to (A.6), the variance of transmitted symbols using any constellation can be calculated as

$$v[k] = \mathbb{E}\{|x[k]|^2\} - |\bar{x}[k]|^2, \quad (\text{A.14})$$

where $E\{|x[k]|^2\}$ is calculated as

$$\mathbb{E}\{|x[k]|^2\} = \sum_{i=0}^{15} |x[k]|^2 P(x[k]), \quad (\text{A.15})$$

where $P(x[k])$ is equal to the product of the probabilities for each bit that determines the constellation point. For instance, for $P(x[k]) = 1/\sqrt{10} + 1/\sqrt{10}$,

$P(P(x[k])) = P(b_0[k] = 1)P(b_1[k] = 1)P(b_2[k] = 0)P(b_3[k] = 1)$ (see Figure A.1(c)).

The variance of transmitted bits in a 16 QAM modulation is, therefore, calculated according to (A.14), using (A.15) and (A.13).

For higher order phase shift-keying modulations, e.g., 8 PSK, 16 PSK, etc., the same method used for BPSK and QPSK can be used. For higher order quadrature amplitude modulations, e.g., 64 QAM, 256 QAM, etc., the method used for 16 QAM can be applied.

B

HSDPA Standard

The High-Speed Downlink Packet Access (HSDPA) is a communications protocol for mobile telephony standardized by the 3rd Generation Partnership Project (3GPP) [1]. It is part of the High-Speed Packet Access (HSPA) set of standards, and deals specifically with the downlink, base station (BS) to mobile station (MS) scenario. In this appendix, it is shown how packets are transmitted in an HSDPA system. A schematics diagram of the HSDPA transmission process is presented in Figure B.1.

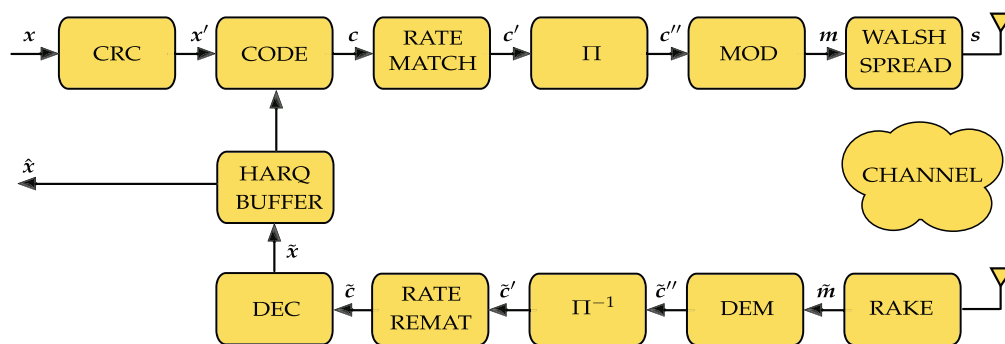


Figure B.1: HSDPA physical layer schematics diagram.

The transmission process starts by calculating Cyclic Redundancy Check (CRC) bits to be appended to the signal to be transmitted, x , resulting in x' . Following, a turbo encoder of rate $R = 1/3$ maps x' into c . The encoded signal passes through a rate matching block which will puncture or repeat some bits, depending on the channel quality and the number of resources available, resulting in c' . An inter-

leaver is applied to the output of the rate matcher, resulting in c'' . Finally, the signal is mapped to a QPSK or 16 QAM constellation, resulting in m , and multiplied by a spreading sequence, resulting in the signal to be transmitted over the channel s .

At the receiver, a rake receiver is employed to map the spreaded signal back to the complex plane, resulting in \tilde{m} . Following, a demodulator maps these complex symbols to sequences of LLRs, \tilde{c}'' , corresponding to the bits that specifies each constellation point (see Appendix A). The signal is de-interleaved, resulting in \tilde{c}' and a rate rematcher reverts the puncturing or repeating patterns introduced by the rate matcher at the transmitter side, resulting in \tilde{c} . Finally the signal is decoded and the result, \tilde{x} , is sent to the Hybrid Automatic Repeat reQuest (HARQ) block. This block will check the CRC bits appended to the transmitted signal. If there is a match, the transmission is assumed to be successful. If not, the LLRs produced by the decoder are saved into a buffer and the receiver will ask for a retransmission. In case of retransmission, the new LLRs are combined with the LLRs in the buffer.

B.1 HSDPA transmission format

HSDPA, as its name suggests, is a packet-based access scheme. According to its standard [67], distinct packets are transmitted using a bandwidth of 5 MHz at a Transport Transmission Interval (TTI) of 2 ms. In each TTI, 3 slots of 2,560 chips are transmitted. Therefore, the chip rate is always kept constant at 3.84 Mcps. These chips are obtained by spreading the signal to be transmitted using orthogonal channelization codes based on Walsh sequences with spreading factor (SF) of 16. Depending on the quality of the channel, as defined by the Channel Quality Indicator (CQI), up to 15 different codes, denoted by High Speed Physical Downlink Shared Channels (HS-PDSCHs), can be used at a time¹. The packet transmission is as shown in Figure B.2.

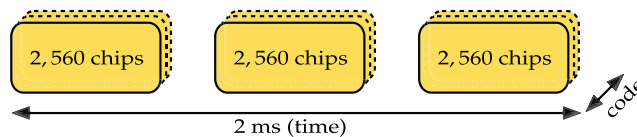


Figure B.2: HSDPA transmitted packet structure.

¹Each code might correspond to a particular user. Also, some users can use more than one code at a time.

The HSDPA transmission process starts by evaluating the CQI to determine the information bit payload, i.e., the Transport Block Size (TBS), the constellation to be used (i.e. QPSK or 16 QAM) and the number of HS-PDSCHs to be used (i.e., 1, 2, 3, etc), according to Table 7A in [68], reproduced here as Table B.1. For instance, given a CQI of 15, the TBS is 3,319 bits, the constellation to be used is QPSK and 5 HS-PDSCHs are used. The CQI is obtained from the receiver through the uplink High Speed Dedicated Physical Control Channel (HS-DPCCH).

Table B.1: Packet format for different values of CQI.

| CQI | SINR | TBS | #HS-PDSCH | CQI | SINR | TBS | #HS-PDSCH |
|-------------------|-------|-------|-----------|--------------------|-------|--------|-----------|
| 1 | -2.80 | 137 | 1 | 16 | 11.32 | 3,565 | 5 |
| 2 | -2.36 | 173 | 1 | 17 | 12.18 | 4,189 | 5 |
| 3 | -1.66 | 233 | 1 | 18 | 13.51 | 4,664 | 5 |
| 4 | -0.71 | 317 | 1 | 19 | 14.52 | 5,287 | 5 |
| 5 | -0.07 | 377 | 1 | 20 | 15.50 | 5,887 | 5 |
| 6 | 0.78 | 461 | 1 | 21 | 16.58 | 6,554 | 5 |
| 7 | 2.54 | 650 | 2 | 22 | 17.58 | 7,168 | 5 |
| 8 | 3.72 | 792 | 2 | 23 | 18.50 | 9,719 | 7 |
| 9 | 4.75 | 931 | 2 | 24 | 19.50 | 11,418 | 8 |
| 10 | 6.77 | 1,262 | 3 | 25 | 20.50 | 14,411 | 10 |
| 11 | 7.83 | 1,483 | 3 | | | | |
| 12 | 8.80 | 1,742 | 3 | | | | |
| 13 | 10.10 | 2,279 | 4 | | | | |
| 14 | 10.53 | 2,583 | 4 | | | | |
| 15 | 11.13 | 3,319 | 5 | | | | |
| Modulation – QPSK | | | | Modulation – 16QAM | | | |

Before encoding, 24 CRC bits are appended to the end of the transport block to allow error detection at the receiver. For a CQI of 15, these 24 bits will be added to the 3,319 information bits, resulting in 3,343 bits.

The next step in the transmission process is to encode the information with a rate $R = 1/3$ turbo encoder. Therefore, at its output there will be three times more bits than at its input. For a CQI of 15, it means that there will be $3,343 \times 3 = 10,029$ bits at its output.

A rate matching algorithm is applied to the output of the turbo encoder to accommodate the information to the virtual IR buffer (of size 9,600 bits) and to the

number bits available for transmission, which is calculated as follows:

$$\# \text{Available bits} = \frac{\text{Chip Rate} \times \text{TTI Interval} \times \# \text{HS-PDSCHs} \times \# \text{Bits per Symbol}}{SF} \quad (\text{B.1})$$

The chip rate is fixed at 3.84 Mcps, the TTI interval is 2 ms and $SF = 16$. Therefore, for a CQI of 15, using QPSK modulation with 5 HS-PDSCH codes, the number of available coded bits to be transmitted is

$$\frac{3.84 \text{ Mcps} \times 2 \text{ ms} \times 5 \times 2}{16} = 4,800 \text{ bits.}$$

Figure B.3 shows this process. Note that the 7,680 chips per packet, transmitted at intervals of 2 ms, generates a rate of 3.84 Mcps.

B.2 HSDPA communication system elements

In this section, the blocks composing the schematics diagram of HSDPA transmission in Figure B.1 are presented in detail.

B.2.1 Turbo codes

Turbo coding, a method first introduced by Berrou [22], has received a lot of attention from academia and industry for its great error control performance. In fact, turbo codes were the first to achieve a performance close to the Shannon limit. Iterative equalization was inspired by this class of codes [23].

A turbo encoder consists of two systematic recursive convolutional codes (usually the same code). Both constituent encoders are fed with the same information, but the information is interleaved prior to being encoded by the second encoder. The interleaver performs two tasks at once. It helps to break correlation between neighboring bits and also creates a random-like code. Figure B.4 shows a schematic diagram for the 3GPP turbo encoder. Although this code has a 1/3 rate, it can achieve higher or even lower rates by puncturing or repeating some parity bits.

Optimal decoding of a turbo code is computationally infeasible due to its huge complexity. Thus, Berrou et. al. [22] devised a near-optimal iterative method that

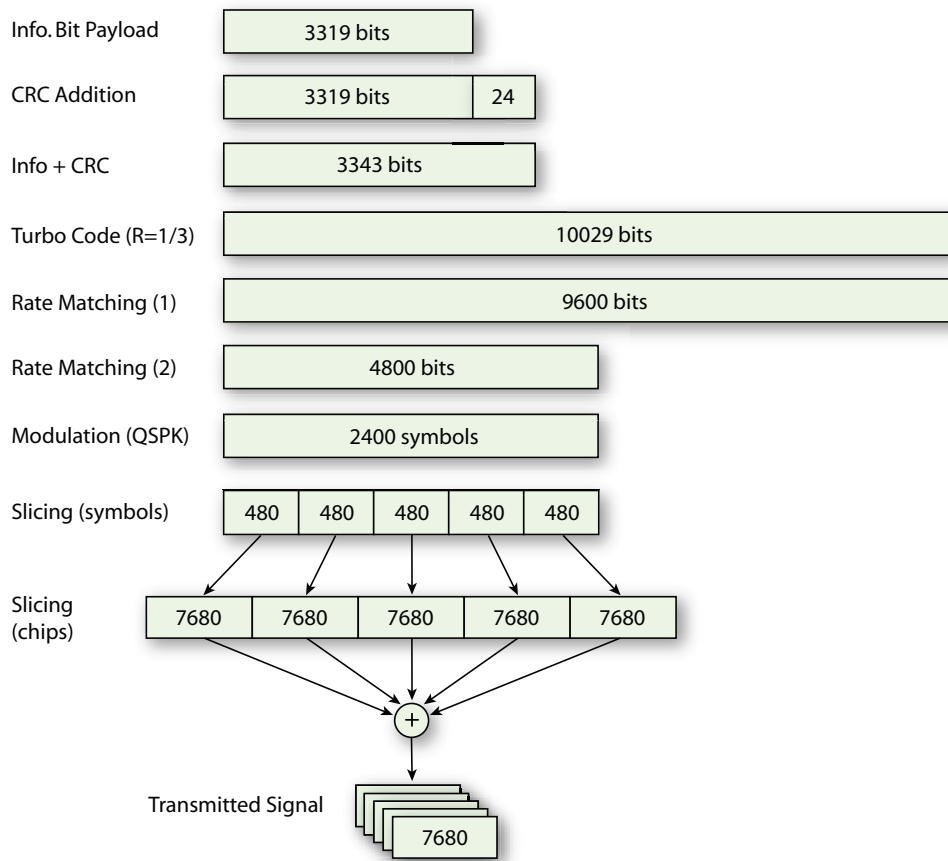


Figure B.3: Packet transmission for a CQI of 15.

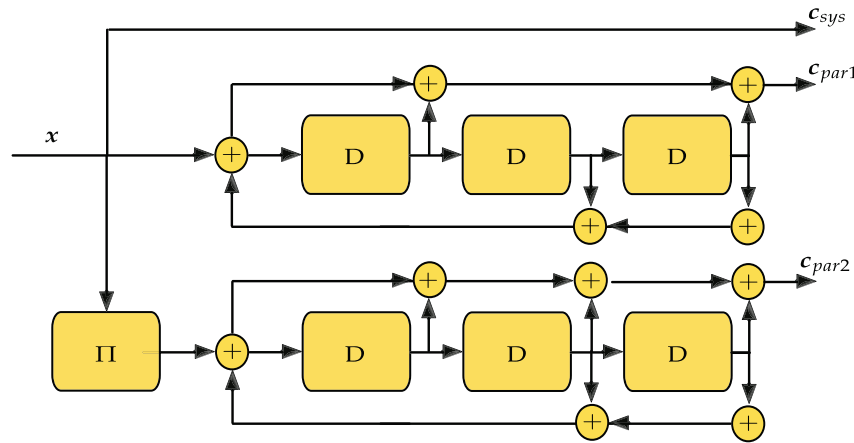


Figure B.4: HSDPA turbo encoder.

consists in decoding each constituent code separately and feeding back the extrinsic information produced by one decoder to another. A crucial point is that both decoders need to produce soft values rather than taking hard decisions. After some iterations, hard decisions are taken on the soft values produced by the decoders. Figure B.5 shows a schematic diagram of a turbo decoder.

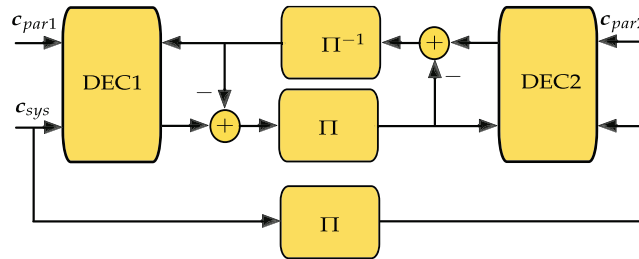


Figure B.5: Turbo decoder schematics diagram.

For the HSDPA standard, the constituent codes have constraint length 4 and are defined by the polynomials $1 + D^2 + D^3$ (feedback), $1 + D + D^3$ (parity 1), and $1 + D + D^2 + D^3$ (parity 2), as seen in Figure B.4. The interleavers used are dithered relative prime (DRP) interleavers [69].

B.2.2 Rate matching

The coded information at the output of the turbo encoder has to be matched to the number of bits available for buffering and transmission. Therefore, a rate matching

function takes place just after encoding. Rate matching is divided into two stages. The first stage ensures the transmission rate will not go over the virtual IR buffer capacity by puncturing some parity bits, if the number of coded bits is greater than the virtual IR buffer size. The second stage ensures the transmission rate will perfectly match the number of binary bits per TTI. This is done by puncturing or repeating systematic and parity bits, depending whether there is more or less bits to be transmitted than available.

The virtual IR buffer, for a 3GPP category 6 system, has a capacity of 9,600 bits. The number of binary channel bits per TTI is 4,800, for QPSK modulation, and 7,680 for a 16 QAM modulation. The TBS, as well as the number of HS-PDSCH codes and the modulation scheme are determined by the CQI value, as seen in Table B.1. The exact puncturing algorithm for both stages, and the repeating algorithm for the second stage can be seen in section 4.2.7 in [68].

B.2.3 Channel interleaver

Channel interleaving provides two benefits. First it breaks correlation between neighboring bits, second, it spreads bursts of error if they occur. Thus, the HSDPA standard has incorporated channel interleaving at the output of the second rate matching stage.

In an HSDPA transmission, every physical channel is interleaved separately by a block interleaver with inter-column permutations. The inter-column permutation patterns can be seen in Section 4.2.5 in [68].

B.2.4 Channel modulation

Two digital modulation schemes are available for HSDPA transmission, QPSK for signal-to-interference noise ratios (SINR) below 11.33 dB and 16 QAM for SINRs greater or equal to this value. Both QPSK and 16 QAM constellations, presented in Figure A are standard and can be found in any textbook on Digital Communications, e.g., [4, 59].

In 16 QAM some bits are more prone to errors than others. To overcome this problem, each retransmission presents a different rearrangement of the bits defining the

points in the 16 QAM constellation. These rearrangements are defined in Section 4.5.7 in [68].

1st Transmission $b_0b_1b_2b_3$

2nd Transmission $b_2b_3b_0b_1$

3rd Transmission $b_0b_1\overline{b_2b_3}$

4th Transmission $b_2b_3\overline{b_0b_1}$

B.2.5 Walsh spreading

After modulation, the signal is spread using Walsh functions with a SF of 16. Signal spreading with orthogonal functions such as Walsh functions allows different users to share the same channel. These users are ideally separable via orthogonal projections. Walsh spreading also improves the performance of the system against interference by virtue of spreading the spectrum, analogously to direct-sequence spread spectrum.

In the case of multipath channels, spread-spectrum signaling allows the use of a rake receiver to overcome part of the interference introduced by multipath propagation. The HSDPA standard limits the number of codes to be shared by users on a particular channel at a time to 15.

B.2.6 Hybrid Automatic Repeat-Request (HARQ)

As mentioned before, a CRC of length 24 bits is added to the information prior to encoding. If the received and the recalculated CRC differ, a retransmission is required. Up to 4 retransmissions can be required. The probability of undetected errors in a transmitted block is negligible, since any changes will alter the CRC (and there are 2^{24} different CRC sequences).

Since rate matching punctures or repeats some bits at the output of the encoder, retransmissions can make use of the bits previously transmitted, or use a different set of bits by performing puncturing or repeating different bits. If the same set of bits are retransmitted, the receiver will combine them with the previously received bits to enhance the decoding process. This method is called Chase combining. If

a different set of bits is transmitted, the decoder will use this incremental information, together with information obtained in previous transmissions, to enhance decoding. This method is called incremental redundancy.

The HSDPA standard supports both HARQ methods. Incremental redundancy has been shown to perform significantly better for high channel-coding rates and high modulation orders at the expense of an increase in complexity. For low channel-coding rates, incremental redundancy does not perform much better than Chase combining, making the latter a better candidate in such situations [70].

B.2.7 Rake receiver

Most wireless channels exhibit multipath propagation, and, for higher signal bandwidths, this causes the received signal to contain distinguishable echoes (copies) of the transmitted signal. These echoes may completely obliterate recognizability of the original signal unless measures are taken to account for the echoes.

A rake receiver partially eliminates the effect of echoes by correlating the transmitted signal with delayed copies of the Walsh sequence, s , used at the transmitter. The result of each “finger” is then weighed and combined, as seen in Figure B.6.

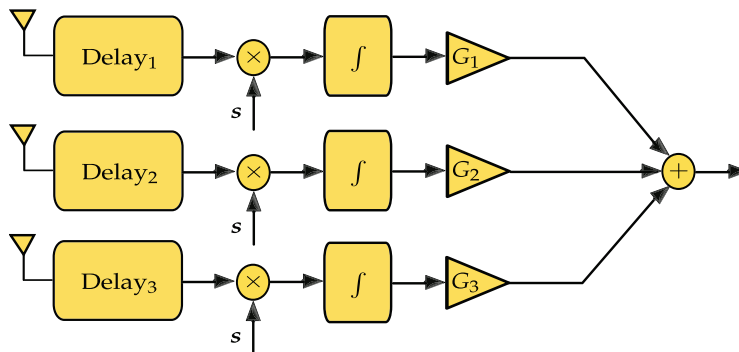


Figure B.6: Rake receiver with three “fingers”.

In HSDPA the spreading is relatively mild, and therefore self-interference is not negligible. Several authors have found that adaptive approximations to the actual matched filter deliver better performance than a rake receiver [71, 72].



LTE Standard

The Long Term Evolution (LTE) standard was proposed by the 3rd Generation Partnership Project (3GPP) [2] to replace HSPA+ [1] in the near future. This standard was conceived to enable much higher speeds to be achieved, along with a considerably lower packet latency which is a growing requirement for many modern services, like video on demand.

For the downlink scenario, LTE applies a multiplexing scheme known as Orthogonal Frequency-Division Multiplexing (OFDM). This method allows providers to share the channel frequency resources among different users and it is resistant to the effects of multipath propagation. Despite its qualities, OFDM transmissions are very sensitive to carrier frequency synchronization and, more importantly, have a high Peak-to-Average Power Ratio (PAPR). Thus, they are not well-suited for the uplink scenario of mobile networks, where the transmitter is normally a battery powered device [21].

In the uplink scenario, i.e., transmissions from mobile station to base station, the LTE standard has proposed the use of a technique called Single-Carrier Frequency-Division Multiple Access (SC-FDMA). SC-FDMA reduces considerably the PAPR, allowing the use of more power-efficient amplifiers in mobile handsets, an important factor for power constrained equipments. However, SC-FDMA transmissions are prone to suffer from the effects of multipath propagation. Therefore, this method requires the signal to be equalized at the receiver's front end.

Over the next sections, a brief description of the LTE standard with focus on the

uplink scenario, is presented. For a more detailed presentation of this scenario, the reader is referred to [21, 2].

C.1 LTE transmission format

In LTE, information is transmitted via resource blocks. Each resource block possess two dimensions, frequency and time. As seen in Table C.1 [21], where N_{sc}^{RB} denotes the number of subcarriers per resource block and N_{RB}^{UL} the number of uplink resource blocks, there are 12 subcarriers per resource block. In the time domain, there are 7 or 6 SC-FDMA symbols, depending whether normal or extended cyclic prefixes are used. Hence, a resource block is as shown in Figure C.1 (assuming a normal cyclic prefix).

Table C.1: Transmission Bandwidth configuration for LTE

| Bandwidth | 1.4MHz | 3MHz | 5 MHz | 10 MHz | 15 MHz | 20MHz |
|---------------|--------|------|-------|--------|--------|-------|
| N_{sc}^{RB} | 12 | 12 | 12 | 12 | 12 | 12 |
| N_{RB}^{UL} | 6 | 15 | 25 | 50 | 75 | 100 |

Each one of the 12 frequency slots occupies a 15 kHz bandwidth. Hence, each resource block has a bandwidth of 180 kHz. In the time domain, each resource block takes 0.5 ms to be transmitted. Thus, if normal cyclic prefix is used, each SC-FDMA symbol takes $0.5/7ms = 71.42\mu s$ to be transmitted¹.

Each SC-FDMA symbol is composed of 12 frequency slots and a single carrier is used for transmission. Therefore, the information in these 12 frequency slots needs to be converted from parallel to serial prior to transmission. The effect is that the symbols to be transmitted on the uplink have a transmission rate 12 times faster than on the downlink scenario. One can easily calculate this transmission rate as $71.42\mu s/12 = 5.95\mu s$.

Continuing the time domain analysis of the LTE uplink scenario, information is organized into frame structures of 20 slots. Each frame, then, takes 10ms to be transmitted. A group of two consecutive slots is called a sub-frame. This frame structure is shown in Figure C.2. Note that, as in Figure C.1, each slot contains 7 symbols.

¹The normal cyclic prefix takes $144T_s = 5.2\mu s$. Thus, only $66.74\mu s$ are effectively used for signal transmission. For extended cyclic prefix, each symbol takes $0.5ms/6 = 83.33\mu s$, from which $512T_s =$

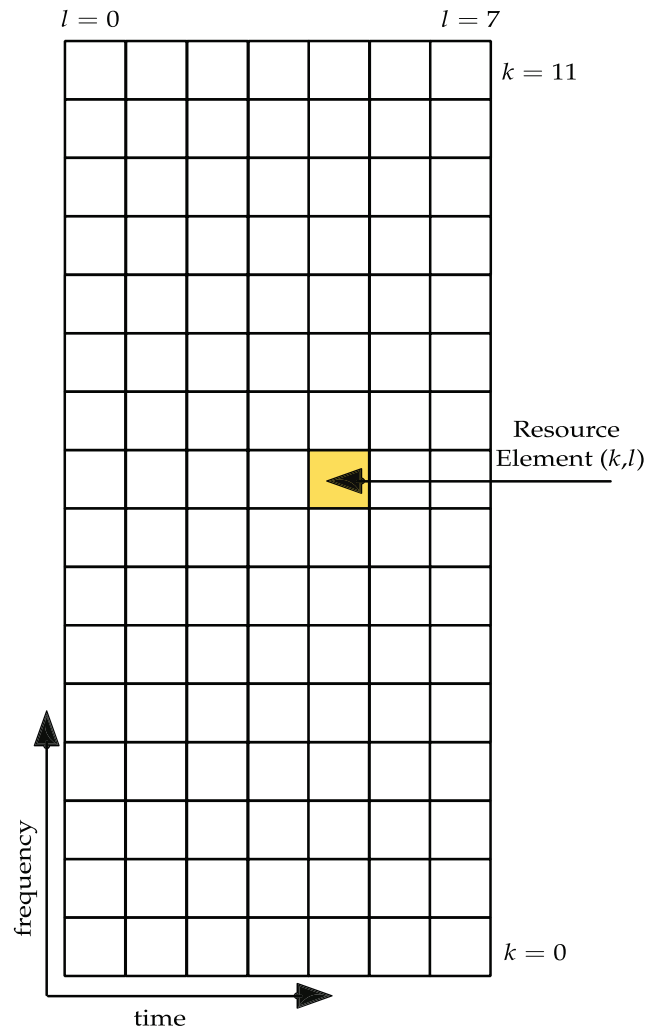


Figure C.1: LTE basic resource block.

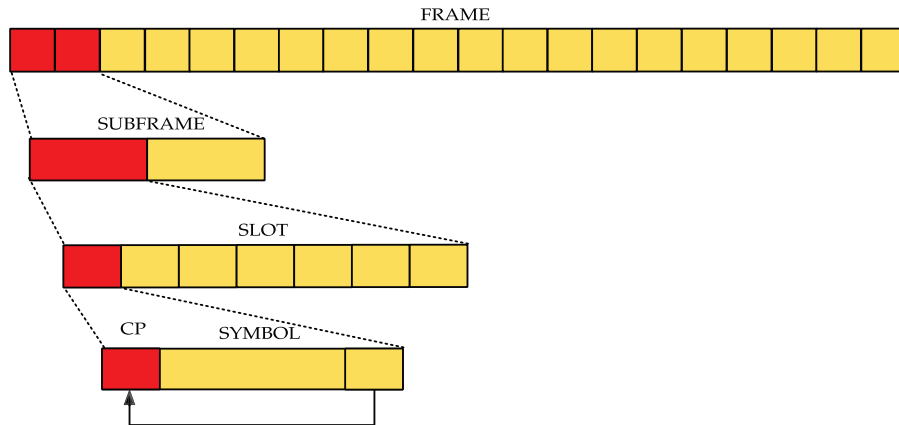


Figure C.2: Frame structure

Hybrid automatic repeat request

As in the HSDPA standard, LTE also uses an HARQ scheme for error detection and retransmission. Resource blocks are transmitted, one at a time, in a continuous fashion. The receiver will then process each block and check for consistency. If an error is detected in a given resource block, the receiver will send a negative acknowledgment (NACK) signal for the transmitter to retransmit this particular block. If no error is detected, an acknowledgment (ACK) signal is transmitted and no retransmission takes place. In the case of a retransmission, the receiver will combine the information from the present retransmission with the information received in previous transmissions.

In LTE, the number of HARQ processes is fixed at 8 [21], both for uplink and downlink. Hence, the transmitter will only completely stop to transmit new resource blocks if there are 8 retransmission processes taking place.

CQI reporting

In order to guarantee the reliability of the transmitted signal, transmission parameters, like the choice of modulation and code rate are determined by a CQI index. For a given transmission scenario, the CQI index to be used is chosen as the highest CQI that guarantees that the transport block error rate (BLER) does not exceeds 10%.

$16.67\mu\text{s}$ corresponds to the cyclic prefix

The correspondence between the CQI indexes, the choice of modulation, and code rate are shown in Table C.2 [21]. The number of bits per resource element is calculated as the modulation order times the coding rate.

Table C.2: CQI Table.

| CQI | Modulation | Coding Rate | Bits per Resource Element |
|-----|--------------|--------------|---------------------------|
| 0 | out of range | out of range | out of range |
| 1 | QPSK | 0.0762 | 0.1523 |
| 2 | QPSK | 0.1172 | 0.2344 |
| 3 | QPSK | 0.1885 | 0.3770 |
| 4 | QPSK | 0.3008 | 0.6016 |
| 5 | QPSK | 0.4385 | 0.8770 |
| 6 | QPSK | 0.5879 | 1.1758 |
| 7 | 16QAM | 0.3691 | 1.4766 |
| 8 | 16QAM | 0.4785 | 1.9141 |
| 9 | 16QAM | 0.6016 | 2.4063 |
| 10 | 64QAM | 0.4551 | 2.7305 |
| 11 | 64QAM | 0.5537 | 3.3223 |
| 12 | 64QAM | 0.6504 | 3.9023 |
| 13 | 64QAM | 0.7539 | 4.5234 |
| 14 | 64QAM | 0.8525 | 5.1152 |
| 15 | 64QAM | 0.9258 | 5.5548 |

C.2 SC-FDMA communication system elements

In this section, all signal processing steps involved in the transmission of information from a MS to a BS for the LTE uplink scenario are presented. A schematic diagram showing all processing stages for uplink transmission, which uses an SC-FDMA scheme as aforementioned, is shown in Figure C.3.

First, CRC bits are calculated and attached to the original signal, x . Then, the binary signal is encoded by a turbo code of rate $R = 1/3$, and the resultant codeword is punctured by a rate matching algorithm to achieve the code rate dictated by the CQI. After being punctured, the resultant codeword is modulated, resulting in c , and transformed into the frequency domain by a discrete Fourier transform of size N , resulting in C . A resource element mapper ensures that the signal will occupy the frequencies reserved for the user. Finally, the signal is sent back to the time domain by an inverse discrete Fourier transform of size M , resulting in c' and a cyclic prefix is added prior to transmission.

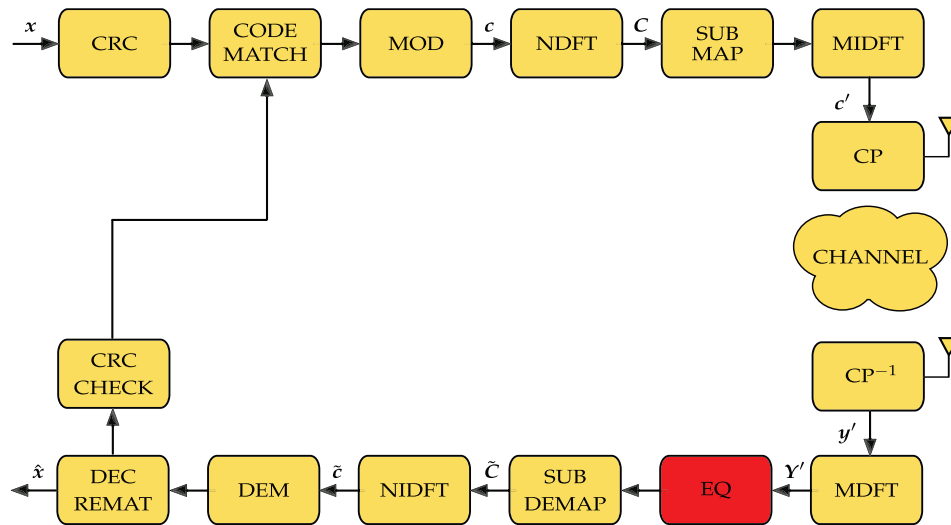


Figure C.3: LTE uplink schematic diagram.

At the receiver side, the cyclic prefix is removed, resulting in y' and the signal is transformed to the frequency domain by a discrete Fourier transform of size M , resulting in Y' . A frequency domain equalizer compensates for the interference introduced by multipath (and possible multiple antennas). After, the signal is mapped back to its original frequencies, resulting in \tilde{C} , and transformed back to the time domain by an inverse discrete Fourier transform of size N , which results in \tilde{c} . After demodulation, the signal rate is matched back to $R = 1/3$ by appending zeros to the previously punctured positions. Finally the signal is decoded. If the CRC of the decoded signal matches the original CRC, the receiver will transmit an ACK signal to the transmitter, else a NACK signal requests the information to be retransmitted.

C.2.1 Cyclic redundancy check

As mentioned before, the LTE standard employs an HARQ retransmission scheme. After receiving a packet of data, the receiver has to check if the data is corrupted to decide whether or not to ask for retransmission. To make it possible for the receiver to check for inconsistencies in the received data, a CRC sequence is calculated and appended to the data to be transmitted. The CRC can be easily computed by passing the data to be transmitted through a feedback shift register whose connections are determined by a cyclic generator polynomial $G(D)$. For instance, the feedback shift register determined by the polynomial $G = 1 + D + D^3$ is shown in Figure C.4.

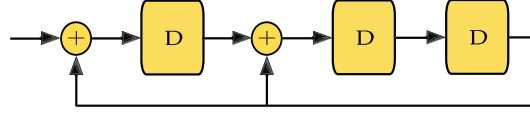


Figure C.4: Feedback Shift Register.

The LTE standard presents 4 generator polynomials with sizes 24 (2), 16, and 8, defined in Section 5.1.1 of [73] as

$$\begin{aligned}
 G_{24A}(D) &= D^{24} + D^{23} + D^{18} + D^{17} + D^{14} + D^{11} + D^{10} \\
 &\quad + D^7 + D^6 + D^5 + D^4 + D^3 + D + 1 \\
 G_{24B}(D) &= D^{24} + D^{23} + D^6 + D^5 + D + 1 \\
 G_{16}(D) &= D^{16} + D^{12} + D^5 + 1 \\
 G_8(D) &= D^8 + D^7 + D^4 + D^3 + D + 1.
 \end{aligned} \tag{C.1}$$

C.2.2 Turbo code

The signal to be transmitted, together with the CRC, is encoded by a convolutional turbo code of rate $R = 1/3$. Both constituent encoders are identical systematic feedback convolutional codes whose connections are defined in Section 5.3.1.2 of [73] by the polynomials $1 + D^2 + D^3$ (feedback), $1 + D + D^3$ (feedforward). The constituent encoders are separated by an interleaver in the same fashion as in Figure B.4.

The second constituent code receives an interleaved copy of the same data received by the first constituent code. This internal interleaver is a quadratic permutation polynomial interleaver where the relationship between the output index i and the input index $\pi(i)$ is given by

$$\pi(i) = f_1 i + f_2 i^2 \pmod{K}, \tag{C.2}$$

where the parameters f_1 and f_2 are determined by the size of the block size K according to Table 5.1.3-3 in [73].

Both constituent codes are terminated by a sequence of three tail bits that do not take part in the internal interleaver. Each one of the three streams generated by

the encoder are interleaved separately by a block interleaver created by writing the numbers $1, 2, \dots, K + 3$ row by row on a matrix with 32 columns and reading them column by column according to the following inter-column permutation pattern (Table 5.1.4-1 in [73])

$$\{0, 16, 8, 24, 4, 20, 12, 28, 2, 18, 10, 26, 6, 22, 14, 30, 1, 17, 9, 25, 5, 21, 13, 29, 3, 19, 11, 27, 7, 23, 15, 31\}. \quad (\text{C.3})$$

After block interleaving, a single output buffer is formed by placing the interleaved systematic bits in the beginning, followed by a bit-by-bit interlacing of the two rearranged parity streams. This interlacing is done in order to allow equal level of protection for each one of the constituent codes.

C.2.3 Rate matching

Rate matching, in LTE systems, is done using a circular buffer. Suppose that the single stream created by the turbo code has D_{Total} bits and the resources available for this user only allows $D_{Res} \leq D_{Total}$ bits to be used. In this scenario, only the first D_{Res} bits of the single stream will be transmitted, while all other bits will be punctured. If $D_{Res} \geq D_{Total}$, all D_{Total} bits are taken and the rate matcher will start repeating the bits in the single stream from the start, hence the name circular, until D_{Res} bits are available for transmission.

C.2.4 Modulation

After rate matching, the sequence of bits are modulated into one of the three possible constellations defined for LTE: QPSK, 16 QAM, and 64 QAM.

C.2.5 Transform precoding

The M_{symbol} symbols at the modulator's output are divided into $M_{symbol} / M_{sc}^{PUSCH}$ sets, each one corresponding to one SC-FDMA symbol. The parameter M_{sc}^{PUSCH} , which defines the size of the discrete Fourier transform at the uplink transmitter, is calculated according to

$$M_{sc}^{PUSCH} = M_{RB}^{PUSCH} \cdot N_{sc}^{RB}, \quad (\text{C.4})$$

where N_{sc}^{RB} is always equal to 12 (see Table C.1) and $M_{RB}^{PUSCH} = 2^{\alpha_2} \cdot 3^{\alpha_3} \cdot 5^{\alpha_5} \leq N_{RB}^{UL}$. N_{RB}^{UL} is determined by the available bandwidth, according to Table C.1.

A discrete Fourier transform, DFT, is then applied according to

$$z \left[l \cdot M_{sc}^{PUSCH} + k \right] = \frac{1}{\sqrt{M_{sc}^{PUSCH}}} \sum_{n=0}^{M_{sc}^{PUSCH}} c \left[l \cdot M_{sc}^{PUSCH} + n \right] \cdot e^{-\frac{2\pi i n k}{M_{sc}^{PUSCH}}}, \quad (\text{C.5})$$

with $k = 0, \dots, M_{sc}^{PUSCH}$ and $l = 0, \dots, M_{\text{ymb}} / M_{sc}^{PUSCH}$. The complex symbols at the output of the modulator are denoted by the terms $c \left[l \cdot M_{sc}^{PUSCH} + n \right]$.

C.2.6 Resource element mapper

After the transform precoding, the signal is multiplied by a scaling factor in order to conform with the transmit power P_{PUSCH} specified in [74]. Also, the signal is sequentially mapped to the resource block elements (i.e., frequency and time slots) assigned for transmission that are not occupied by reference signals.

C.2.7 SC-FDMA baseband signal generation

After being mapped into resource blocks, the signal to be transmitted undergoes an inverse discrete Fourier transform, IDFT, operation that maps the subcarrier amplitudes back into the (complex) time domain according to

$$s_l(t) = \sum_{k=\lfloor N_{RB}^{UL} N_{sc}^{RB} / 2 \rfloor}^{\lfloor N_{RB}^{UL} N_{sc}^{RB} / 2 \rfloor - 1} a_{k+\lfloor N_{RB}^{UL} N_{sc}^{RB} / 2 \rfloor, l} \cdot e^{-2\pi i (k+1/2) \Delta_f (t - N_{CP,l} T_s)}, \quad (\text{C.6})$$

where $a_{k,l}$ denotes the content of resource element (k, l) . N_{RB}^{UL} and N_{sc}^{RB} are determined according to Table C.1. All timing processes in the LTE standard are measured in multiples of $T_s = \frac{1}{15000 \times 2048} \cdot N_{CP,l}$, which denotes the cyclic prefix interval for the l th time slot, is equal to $160T_s$ for $l = 0$ and $144T_s$ for $l \neq 0$ ².

²It is also possible to use extended cyclic prefixes with interval $512T_s$ for all l .

C.2.8 Cyclic-prefix attachment

In (C.6), all SC-FDMA signals were generated respecting a time delay of $N_{CP}T_s$. This was done because, prior to transmission, a cyclic prefix is attached at the beginning of each transmitted SC-FDMA signal. On the downlink, this cyclic prefix practically guarantees that one symbol won't spread over the next one due to multipath propagation. In the uplink, however, the cyclic prefix interval alone is not enough to prevent symbols from spreading over other symbols, causing intersymbol interference.

A cyclic prefix is obtained by copying the end of the original signal to be transmitted and placing it at its beginning, as shown in Figure C.2. As stated on last section, the cyclic prefix occupies a time slot of $160T_s$ for the first time slot in a resource block and $144T_s$ for all subsequent time slots.

C.2.9 SC-FDMA signal reception

At the receiver side, apart from inverting the signal processing steps undergone during transmission, the signal has to be equalized to compensate for the effects of multipath propagation (and possibly multi-antenna interference from MIMO scenarios). Normally, equalization is carried in the frequency domain, just after inverting the SC-FDMA signal generation by means of a discrete Fourier transform, as shown on Figure C.3.